

RCA Review

A technical journal published quarterly
by RCA Research and Engineering
in cooperation with the subsidiaries
and divisions of RCA.

Contents

- 517 Memorial to David Sarnoff by Elmer W. Engstrom
- 519 Amplification—Modern Trends, Techniques and Problems II
Leon S. Nergaard
- 567 Resolving Power Functions and Integrals of High-Definition Television and
Photographic Cameras—A New Concept in Image Evaluation
Otto H. Schade, Sr.
- 610 Techniques for High-Data-Rate Two-Dimensional Optical Pattern Recog-
nition
R. Croce and G. Burton
- 636 Low-Noise Punch-Through P-N- ν -P, P-N-P, and P-N-Metal Microwave
Diodes
S. G. Liu and J. J. Risko
- 645 Switching Times of a Moderate-Power GaAs Field-Effect Transistor
L. S. Napoli, W. F. Reichert, R. E. DeBrecht, and A. B. Dreeben
- 650 Transit-Time-Spread-Limited Time Resolution of Image Tubes in Streak
Operation
Illes P. Csorba
- 660 Technical Papers
- 662 Patents
- 664 Authors
- 668 Index to Volume 32, 1971



David Sarnoff
1891—1971

For more than 35 years I had the honor of serving under David Sarnoff, first in his role as President and later when he became Chairman of the Board and Chief Executive Officer of RCA. During those years, it was my privilege to bear witness to an era of unparalleled progress sparked by the vision of a truly remarkable personality. More than any other man in his time, David Sarnoff was the driving spirit who must be credited with transforming electronic technology from its research beginnings into a vital force that now permeates all phases of our lives.

With unbounded faith in scientists and engineers—at times more faith in them than they were willing to express themselves—David Sarnoff committed himself without qualification to the principles of industrial research. He has, therefore, left us with a legacy of inspiration to guide the further progress of electronics for generations to come.

For those of us who served with him, for those who follow in his footsteps, the story of David Sarnoff's dedicated life encompasses all of the opportunities America holds forth for the achievement of greatness. He was not content merely to dream impossible dreams. He fulfilled them. And by doing so, he has made it possible for all who continue to labor in this field to fulfill their own lives—if they have the will.

Thus, there is only one way to properly conclude a tribute to the life of David Sarnoff. Neither nostalgia nor memories will suffice—only challenges.

Elmer W. Engstrom

RCA Corporation

Robert W. Sarnoff Chairman of the Board and Chief Executive Officer
A. L. Conrad President and Chief Operating Officer

Editorial Advisory Board

Chairman, J. A. Rajchman RCA Laboratories

E. D. Becken RCA Global Communications
G. H. Brown RCA Patents and Licensing
G. D. Cody RCA Laboratories
H. L. Cooke RCA Research and Engineering
A. N. Goldsmith Honorary Vice President, RCA
N. L. Gordon RCA Laboratories
G. B. Herzog RCA Laboratories
J. Hillier RCA Research and Engineering
E. O. Johnson RCA Solid-State Division
H. W. Leverenz RCA Patents and Licensing
D. S. McCoy RCA Laboratories
H. F. Olson RCA Laboratories
K. H. Powers RCA Laboratories
P. Rappaport RCA Laboratories
L. A. Shottliff RCA International Licensing
T. O. Stanley RCA Laboratories
J. J. Tietjen RCA Laboratories
W. M. Webster RCA Laboratories

Secretary, Charles C. Foster RCA Research and Engineering

Editor Ralph F. Clafone

Associate Editors

W. A. Chisholm RCA Limited
M. G. Gander RCA Service Company
T. G. Greene Missile and Surface Radar Division
W. O. Hadlock RCA Research and Engineering
W. A. Howard National Broadcasting System
C. Hoyt Consumer Electronic Systems Division
E. McElwee RCA Solid-State Division
C. A. Meyer RCA Electronic Components
M. G. Pletz Defense Engineering
C. W. Sall RCA Laboratories
I. M. Seideman Astro-Electronics Division
W. Varnum Commercial Electronic Systems Division

Amplification—Modern Trends, Techniques, and Problems, II

L. S. Nergaard

Consultant, RCA Laboratories, Princeton, N. J.

Abstract—This paper reviews progress in power generation and low-noise devices at the frontier of the spectrum during the past ten years. First it develops the physical notions required to understand the new devices in elementary terms. Then it examines the operation of the new devices themselves: avalanche diodes of a variety of kinds, transferred-electron devices, microwave transistors, and acousto-electric devices. Then it examines their present performance and makes some cautious guesses about their future.

1. Introduction

Some ten years ago the writer scanned the electron-devices field to see what was new, what the new devices did, how they did it and how well they did it.¹ In retrospect three things were notable about the era:

1. Most of the work was concentrated in the microwave field. This was natural; as the accessible communication spectrum becomes cluttered, new parts of the spectrum must be opened up and at the time the microwave spectrum was next on the list. As will become apparent in due course, now it is the millimeter-wave area that is receiving increasing attention.
2. All of the new devices, with one exception, the Adler tube, were solid-state devices. The basic work on vacuum tubes was well in

hand, new ideas were drying up, and the possible improvements looked like refinements in engineering. On the other hand, solid-state devices were new, relatively unexplored, and glamorous. It was obvious where the new challenges lay.

3. All of the new devices were "receiving devices," i.e., small-signal devices with emphasis on low-noise performance. Included were low-noise traveling-wave tubes, parametric amplifiers, tunnel-diode amplifiers, masers, and the Adler tube. The break-throughs that led to solid-state power sources with acceptable power outputs in this frequency range had yet to occur.

Now, ten years later, things have changed; break-throughs in power generation have occurred, and work on power generation occupies major attention and work on low-noise devices receives lesser attention, at least in the journals. When power generation catches up with the performance of the more-mature low-noise devices, the emphasis may shift again.

In view of the break-throughs that have occurred in recent years, it may be timely to look again at the new devices, see how they work in elementary terms, and examine how far they have come in performance. The list of new devices includes:

1. Avalanche diodes
2. Transferred-electron devices
3. Microwave transistors
4. Acoustoelectric amplifiers

Because all of these devices have much in common, it seems worthwhile to set forth the basics they share in a separate section to avoid repetition in the description of the new devices. Having done so, the individual devices will be described and then the performance of all will be discussed in a common section so that their performance may be compared.

2. Some Basic Ideas Underlying the New Devices

The new devices are constructed of semiconductors—a limited class of materials within the larger domain of solids. As the name implies, the electronic properties of semiconductors lie between those of insulators and metals. At zero degrees Kelvin they are insulators and at higher temperatures they acquire conductivity. Because the useful semiconductors are crystalline and of high purity, an electron moving freely through the crystal lattice sees a periodic electric field, i.e., it sees a field much like that seen by a wave packet moving through a

periodic filter network. The analogy is very close because an electron can be regarded as a wave packet (witness electron diffraction) with an energy⁸

$$\mathcal{E} = \hbar\omega = \frac{p^2}{2m^*} \quad [1]$$

and momentum

$$p = \hbar\beta,$$

where

$$\hbar = h/(2\pi)$$

h = Planck's constant,

m^* = the effective mass of the electron,

β = the phase constant of the electron.

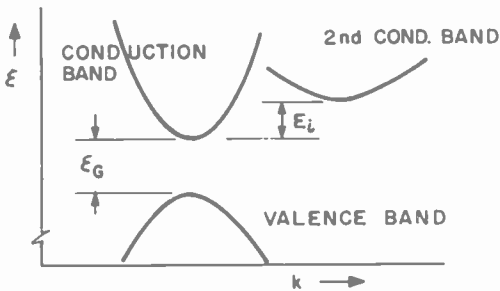


Fig. 1—The band structure of semiconductor with two conduction bands.

Thus, when a solid-state physicist draws an ω - β diagram for his "filter," he labels it an \mathcal{E} - K diagram (K is the phase constant in his nomenclature) as shown in Fig. 1. There are pass bands and stop bands, which the physicist calls the valence band, the conduction band and, in some semiconductors, higher conduction bands. The stop band between the valence band and first conduction band is called the band-gap, and the gap between the minima of the first and second conduction bands is called an excitation energy. In a semiconductor, the valence band is filled with electrons at zero degrees Kelvin and the material is

insulating because there are no unoccupied energy states in the valence band into which electrons can move as they try to acquire energy, and the conduction bands are empty. As the temperature is raised, some electrons in the valence band are thermally excited to the conduction band. These electrons can move because there are unoccupied energy-states above those they occupy. Furthermore, electrons in the valence band can now move into the "holes," unoccupied states, left by the excited electrons. The movement of the holes in the valence band as electrons move is tantamount to the movement of positive charges, called positive holes or, in the jargon, "holes." Thermal excitation is not the only way to get electrons into a conduction band or holes in a valence band, a matter to be discussed shortly.

It will be recalled that the energy of an electron is given by

$$\mathcal{E} = \frac{p^2}{2m^*} \quad [3]$$

Now the bands are approximately parabolic about their minima and maxima so the effective masses in various bands are constant, approximately, and their values are given by

$$\frac{1}{m^*} = \frac{\partial^2 \mathcal{E}}{\partial p^2} \quad [4]$$

It follows that the "steeper" the parabola, the smaller the effective mass. Hence, if two conduction bands have different steepnesses, excitation of an electron from one band to another leads to an abrupt change in effective mass, an effect that is exploited in transferred-electron devices, so called because electrons are transferred from one band to another during operation.

Whereas the \mathcal{E} - K diagram is useful in representing a semiconductor of uniform properties, it is less useful where the properties of the semiconductor are varied along its length to achieve particular useful effects. Then the customary representation is that shown in Fig. 2. Here, just the maximum of the valence band and the minimum of the conduction band are shown as a function of distance. Also shown are discrete energy levels immediately above the valence band, labeled N_A , and immediately below the conduction band, labeled N_D . These levels are produced by adding atoms with one less valence electron than the host crystal for acceptors and atoms with one more electron than the

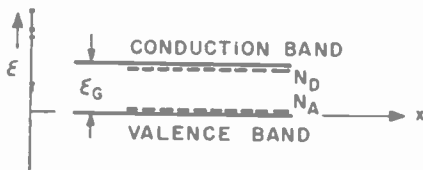


Fig. 2—Energy diagram showing band edges versus distance.

host crystal for donors. The acceptors take electrons from the valence band and leave holes behind, and the donors contribute their "excess" electrons to the conduction band, both at ordinary temperatures. If both acceptors and donors are present, electrons from the donors drop into the holes produced by the acceptors. The semiconductor is n-type (electron conducting) if the number of donors exceeds the number of acceptors and is p-type if the number of acceptors exceeds the number of donors; if the numbers of donors and acceptors are equal, the material is said to be compensated. Even then there will be a few holes in the valence band and a few electrons in the conduction band due to thermal excitation.

As noted above, the utility of semiconductors arises in large part from the effects that result from tapering the properties along the length. The most useful "taper" is the p-n junction, and because its properties are utilized in a number of the new devices, and is the basic ingredient of transistors, it may be useful to review its properties. Such a junction is shown in Fig. 3. It consists of an n-type region and a p-type region meeting at the plane $X = 0$. The donors and acceptors are shown as uniform and extending to the junction. Such a junction is called an abrupt junction to distinguish it from a tapered junction, which has properties different in detail if not in principle. It will be

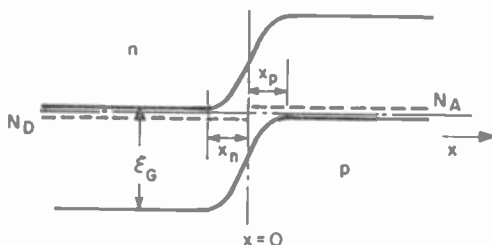


Fig. 3—A p-n junction.

noted that the conduction bands of the two sides of the junction are displaced by the bandgap, approximately. This comes about because the electrons in the conduction band (and the holes in the valence band) are distributed in energy according to the Boltzmann law

$$n = n_o \exp \left\{ -\frac{\mathcal{E}}{kT} \right\} = n_o \exp \left\{ -\frac{qV}{kT} \right\} \quad [5]$$

where n = density of electrons at energy \mathcal{E} ,

n_o = reference density,

k = Boltzmann's constant,

T = temperature,

q = electron charge,

V = voltage.

The density of electrons is high in the n region and low in the p region so electrons in the n region try to spill into the p region, but in so doing they set up a dipole field that reduces the spillover until the flows of electrons in forward and backward directions are equal. The dipole region (see Fig. 3) consists of a region X_n in the n region, which is depleted of electrons, and a region X_p in the p region, which is depleted of holes. If the donor density in the n region is N_D , the field in this region is given by

$$\frac{\partial E}{\partial x} = \frac{N_D q}{\epsilon}, \quad [6]$$

where ϵ is the permittivity of the semiconductor. A first integration gives

$$E = \frac{N_D q}{\epsilon} (X_n - X), \quad [7]$$

so the field rises linearly from X_n towards the middle of the junction, a property used in avalanche devices. A second integration gives

$$V_n = \frac{N_D q}{2\epsilon} (X_n - X)^2, \quad [8]$$

so the total voltage drop on the n side is

$$V_n = \frac{N_D q}{2\epsilon} X_n^2. \quad [9]$$

Then the width of the depletion layer in terms of the voltage is

$$X_n = \sqrt{\frac{2\epsilon V_n}{N_D q}}, \quad [10]$$

and the charge "stored" is

$$Q_n = N_D q X_n = \sqrt{2\epsilon N_D q V_n}. \quad [11]$$

Similar relations can be written for the p side, and when the relations for X_n , Q_n , X_p , and Q_p are combined, the results are

$$X_n = \sqrt{\frac{2\epsilon N_A V_o}{N_D (N_D + N_A) q}}, \quad [12]$$

$$X_p = \sqrt{\frac{2\epsilon N_D V_o}{N_A (N_D + N_A) q}}, \quad [13]$$

and
$$Q = \sqrt{\frac{2\epsilon N_A N_D q V_o}{N_D + N_A}}, \quad [14]$$

where V_o = total voltage drop
= the contact potential.

If the junction is "back-biased" to increase the potential barrier preventing the flow of charge, as in Fig. 4, the relations become

$$X_n = \sqrt{\frac{2\epsilon N_A (V + V_o)}{N_D (N_D + N_A) q}}, \quad [15]$$

$$X_p = \sqrt{\frac{2\epsilon N_D (V + V_o)}{N_A (N_D + N_A) q}}, \quad [16]$$

$$\text{and } Q = \sqrt{\frac{2\epsilon N_A N_D q (V + V_o)}{N_D + N_A}} \quad [17]$$

where V_o is the applied voltage. Hence the widths of the depletion layers can be controlled by adjustment of the applied voltage V , a property used in avalanche diodes. Furthermore

$$\frac{\partial Q}{\partial V} = \sqrt{\frac{\epsilon N_A N_D q}{2(N_D + N_A)(V + V_o)}} = C, \quad [18]$$

where C is the junction capacitance. The variation of C with applied voltage is the property exploited in varactors.

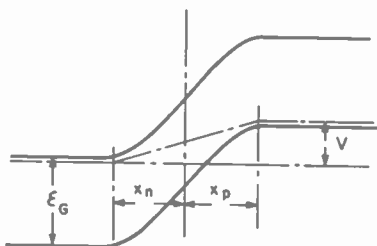


Fig. 4—A back-biased p-n junction.

When the junction is forward biased the barrier is reduced and electrons spill into the p region and holes spill (holes "spill" upwards in the energy diagram) into the n region. When an electron spills (is "injected" in the jargon) into the p region, a hole enters from the contact to the n region to maintain charge neutrality, so the electron is paired with a hole to maintain local charge neutrality. A hole in the n region is similarly paired with an electron. The pairs drift by diffusion or, if there is a field in the region, by field-induced drift. The drift velocity of a pair is that of the minority carrier (except at high injection levels) and is given by

$$v = \mu E, \quad [19]$$

where

μ = the particle mobility.

The mobility, in turn, is given by

$$\mu = \frac{q}{m^*} \frac{l_F}{v_T}, \quad [20]$$

where l_F = the particle mean-free-path, about 100-1000 lattice spacings

v_T = thermal velocity.

It should be noted particularly that the mobility is inversely proportional to the effective mass. Hence the curvature of the bands discussed in connection with Eqs. [3] and [4] is reflected directly in the mobility and it is the change in mobility from band to band that is exploited in transferred-electron devices; just how will be discussed later in the examination of individual devices.

Pairs recombine in the course of time at a rate that depends exponentially on time in the bulk semiconductor, so devices that depend on the transit of pairs between electrodes or opposed junctions, as in the transistor, must be made thin to minimize the loss of pairs by recombination. The current-amplification factor of a transistor, α , is directly proportional to the number of pairs that survive transit.

If only neutral pairs move, how is current carried? The answer is: mostly by the majority carriers. Pairs increase the local conductivity so the voltage required to achieve a fixed current drops. The injection of pairs is like shorting out a part of a resistor.

The minority-carrier devices comprise an important class of devices. However, they are not the only important class. In fact, most of the new microwave devices to be described are majority-carrier devices.

3. Avalanche Devices

In 1958, Read proposed a solid-state counterpart of Llewellyn's vacuum diode.^{3,4} Such a diode oscillator was first achieved by Johnston, DeLoach, and Cohen, although not quite in the form Read visualized.⁵ The diode consists of a p-n junction with an n⁺ (plus for heavily-doped) contact on the n side. The doping of the p material is heavy enough relative to the n doping so that the depletion layer in the p material is thin (see Eq. [13]) and almost all of the voltage drop occurs in the n material. Now the trick is to choose the doping of the n material, its width W , and the operating voltage so that

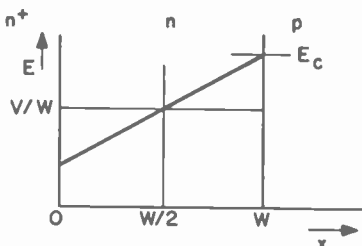


Fig. 5—The distribution of electric field versus distance in an avalanche diode.

1. The thickness of the n depletion layer approximately equals the width,

$$X_n \sim \sqrt{\frac{2\epsilon(V + V_o)}{N_D q}} \approx W \quad [21]$$

i.e., the diode is "punched through," in the jargon.

2. The field at the p-n junction is the critical field E_c for the formation of electron-hole pairs by avalanche

$$E(w) = \frac{N_D q W}{2\epsilon} + \frac{V}{W} = E_c \quad [22]$$

(the critical field in silicon is about 3.3×10^5 volts/cm). Then the situation is as sketched in Fig. 5.

When E has an ac component as in Fig. 6, pairs are generated on the positive swing. Now, the rate of generation is given by

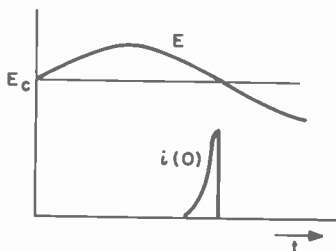


Fig. 6—The electric field E and injected current $i(o)$ in an avalanche diode.

$$\frac{\partial n}{\partial t} = \alpha n v f(E), \quad [23]$$

where

n = electron density

α = constant

v = electron velocity

$f(E)$ = ionization function

The ionization function looks as shown in Fig. 7. Because the rate of generation is proportional to the number already generated as well

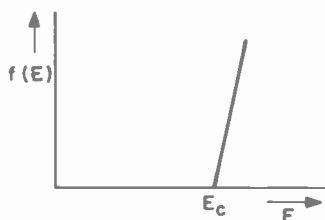


Fig. 7—The ionization function for holes and electrons in a semiconductor.

as $f(E)$, the number of pairs builds up as shown by the lower curve in Fig. 6. Hence, the electron current “injected” into the depleted region (hole are collected immediately)

$$i(o) = n q v_s, \quad [24]$$

(where v_s is the saturation velocity) is approximately 90° out of phase with the voltage. Each electron crossing the diode produces a square pulse of current in the circuit that starts when the electron starts and stops when the electron is collected. This is easily seen from a simple-minded argument and Fig. 8. Suppose an electron moves a distance dx in a time dt between parallel electrodes separated a distance L and supplied with a voltage V . Then the work done on the electron is

$$w = q E dx = q \frac{V}{L} dx. \quad [25]$$

This energy must be supplied by the battery. Hence,

$$q \frac{V}{L} dx = iVdt, \quad [26]$$

or

$$i = \frac{qdx}{Ldt} = \frac{qv}{L}, \quad [27]$$

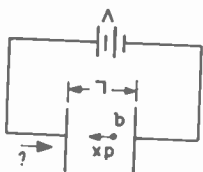


Fig. 8—A space-charge-limited diode showing the current in the external circuit as the result of charge movement within the diode.

and the current persists as long as q or v does. The fundamental Fourier component of such a pulse is

$$\frac{\sin \frac{\omega T}{2}}{\frac{\omega T}{2}} \quad [28]$$

where T is the transit time and the phase shift is

$$\varphi = \frac{\omega T}{2}. \quad [29]$$

So, if the avalanche produces a current with a fundamental component

$$i_1 \sim \alpha V \sin (\omega t - \pi/2) \quad [30]$$

at the junction, the current in the external circuit is

$$\begin{aligned}
 i &= \alpha V \frac{\sin \frac{\omega T}{2}}{\frac{\omega T}{2}} \sin \left(\omega t - \frac{\pi}{2} - \frac{\omega T}{2} \right) \\
 &= - \frac{\alpha V}{\omega T} [(1 - \cos \omega T) \sin \omega t - \sin \omega T \cos \omega t]. \quad [31]
 \end{aligned}$$

Hence the conductance of the diode is

$$G = - \frac{\alpha V}{\omega T} (1 - \cos \omega T), \quad [32]$$

which is negative, and has its maximum negative value when

$$\omega T = \pi, \quad [33]$$

i.e., when the transit time is half an rf period. There are other ranges of ωT where a large negative conductance occurs, namely when

$$\omega T \approx (2n + 1) \pi, \quad n \text{ an integer}, \quad [34]$$

but the ωT in the denominator make these regions less favorable.

Since the diode can provide a negative conductance, it can be used to produce an amplifier by cancelling out most of the loss of the passive circuit in which it is placed. Such amplification was achieved by DeLoach and Johnston.⁶ Such were the avalanche oscillators and amplifiers until 1967.

In April of 1967, Prager, Chang, and Weisbrod described a new avalanche-diode oscillator that operated in the UHF band, with spectacular output and efficiency; outputs of over 400 watts peak and efficiencies of 25 percent compared to usual values of a watt or less and efficiencies of a few percent.⁷ They called the diode the "anomalous diode" because the name seemed singularly appropriate at the time. It is no longer anomalous, thanks to the work of Johnston, Scharfetter, and Bartelink⁸ and Clorfeine, Ikola, and Napoli.⁹

The basic concepts underlying the device are readily understood even though the detailed quantitative theory gets a little messy. The diode is again an n⁺-n-p diode operated in a punched-through regime.

Suppose the field is as shown by Curve 1 in Fig. 4 at time $t = 0$ at which time a constant current density J is impressed. Then, since there are no carriers in the diode, the field must rise from its initial value as

$$E = Jt, \quad [35]$$

since all of the current is displacement current. In time the field at $X = W$ reaches the critical value E_c , Curve 2, and from there on the

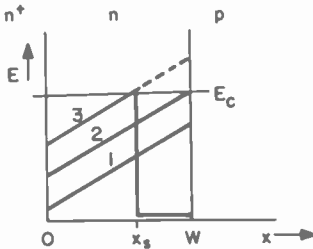


Fig. 9—The field distribution at successive times in the anomalous avalanche diode (trapatt.)

point of intersection of the E curve with the E_c line, X_s , progresses to the left with a velocity

$$v = \frac{J}{N_D q}. \quad [36]$$

By making J large enough, this velocity can be made to exceed the saturation velocity of the holes and electrons generated at the crossing. Hence, the intersection leaves a plasma in its wake and the field drops abruptly to a low value as shown by Curve 3. When the intersection reaches the n^+ layer, ionization stops and the diode is left with a very low voltage across it. As holes and electrons drain out of the plasma, holes to the right and electrons to the left, the plasma disappears, the voltage rises again and the field approaches the initial value. The slow draining accounts for the relatively long "transit time." The behavior is reminiscent of the "sawtooth" generator of some years ago using a gas-discharge tube. E. M. Leyton (a friend of the people involved) went a little further and remarked that the "boys" have apparently invented a solid-state spark-gap. None-the-less,

because of the low voltage drop through the plasma, the diode can be very efficient in a circuit that shapes the current waveform properly. For example, suppose the current and voltage both could be made "square." Then the efficiency would be

$$\eta = \frac{8}{\pi^2} \sim 81\% \quad [37]$$

assuming the plasma voltage drop to be zero. It is known experimentally that support of the fundamental and certain harmonics by the circuit is necessary for high-efficiency operation. Some of the circuits that achieve high efficiencies seem superficially simple yet cold-probe measurements show that they present high reactances to a variety of higher harmonics.¹⁰ It may be that a practical compromise between efficiency and circuit complexity has been reached; a more elaborate circuit might be impossible to tune in service.

Very recently a new diode oscillator, called the baritt for "barrier injection transit time,"* has appeared.¹¹ It is not an avalanche diode, but is made of silicon and is closely related to the avalanche diodes discussed above. Hence, it is described here, rather than in a separate section. In operation it comes closer to the Llewellyn diode than does the Read diode.

The diode is of n-type silicon with metallic contacts, so each end has a Schottky barrier layer as shown in Fig. 10a.¹² Platinum contacts, sintered to form a platinum-silicide interface, are used. The heights of the end barriers are shown in the figure as φ_1 and φ_2 , which may be equal. When the diode is back-biased to punch-through by a voltage V , as in Fig. 10b, the height of the barrier at the right-hand side is reduced by Schottky effect to φ_2 .¹³ The Schottky relation for the reduction in φ is

$$\Delta\varphi = \sqrt{qE}, \quad [38]$$

where E is the field, so the current rises as

$$i = i_0 \exp \left\{ \frac{q\sqrt{qE}}{kT} \right\}, \quad [39]$$

* One of these days, the ingenuity in coining acronyms will exceed that of the invention.

a very steep rise. Now the arguments adduced for the avalanche diode apply. The injected current, in contrast to the avalanche diode, is in phase with the voltage, so that Eq. [30] becomes

$$i = \alpha V \sin \omega t. \tag{40}$$

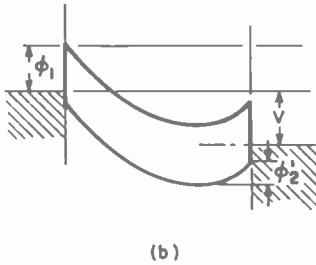
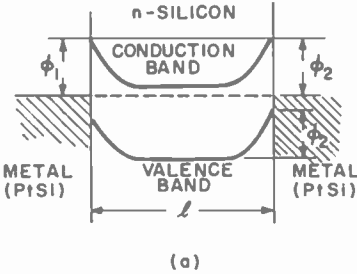


Fig. 10—(a) The band structure of a baritt without bias and (b) the band structure when back-biased.

Eq. [31] becomes

$$i = \alpha V \frac{\sin \frac{\omega T}{2}}{\frac{\omega T}{2}} \sin \omega \left(t - \frac{T}{2} \right), \tag{41}$$

and Equation [32] becomes

$$G = \alpha V \frac{\sin \omega T}{\omega T}. \tag{42}$$

Hence the maximum negative conductance occurs at

$$\omega T = \frac{3\pi}{2}, \quad [43]$$

instead of at

$$\omega T = \pi \quad [44]$$

as in the avalanche diode.

The advantages of the baritt are that it is simple and cheap and, more important, since it does not involve avalanche, which tends to be noisy, its noise should be about 20 dB less than that of an avalanche diode.

In closing this section, it should be noted that both silicon and gallium arsenide have been used for the construction of avalanche diodes, and all are majority-carrier devices. Furthermore, since they operate under punched-through conditions, they are space-charge-limited devices.

4. Transferred-Electron Devices

The transferred-electron devices, like the avalanche diodes, were discovered on paper before they were realized in the laboratory. In fact it took a little time before it was demonstrated that what happened in the laboratory was indeed what had been predicted on paper.

In 1961 Ridley and Watkins predicted that a semiconductor with two conduction bands would yield a negative resistance. They also predicted that in the negative resistance regime a perturbation would make electrons cluster to form "domains" instead of dissipating as in normal diffusion. In 1962, Hilsum predicted that the negative resistance would start at a field of 3200 volts/cm in gallium arsenide (GaAs) and that it could be used to produce what he called transferred-electron oscillators and amplifiers (TEO's and TEA's).¹⁵

A year later Ridley elaborated the theory and computed the movement of his domains.¹⁶ That same year Gunn, in the course of measurements on gallium arsenide, found coherent microwave oscillations and a year later measured the movement of domains by a probe technique.¹⁷ Kroemer pointed up the connection between the Gunn effect and the work of Ridley, Watson and Hilsum, then Hutson, Jayaraman, Chyno-

weth, Cornell, and Feldman wrapped it up by measuring the change with pressure in excitation energy between conduction bands.^{*18,19}

So much for the background, for the moment at least, and on to the devices. The basic current-voltage characteristic of the device is shown in Fig. 11. (The abscissa is E , the voltage per unit length, instead of the voltage itself). The characteristic may be constructed

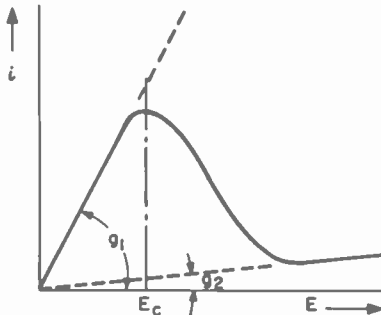


Fig. 11—The current-electric-field characteristic of a double-conduction-band semiconductor.

of two straight lines, the first with a slope g_1 corresponding to having all of the electrons in the first band, the second with a slope g_2 (about $1/20$ of g_1) corresponding to having all of the electrons in the second band, and a transition between the two starting at the excitation field E_c . The transition occurs as more and more of the electrons are transferred to the upper band. The transition starts just where Hilsum said it would. The characteristic is difficult to measure because of the instabilities that set in when the field exceeds E_c and the differential conductance becomes negative.

As noted earlier, the first oscillator operating on this characteristic was achieved by Gunn. An amplifier operating on this characteristic was achieved by Thim, Barber, Hakki, Knight, and Uenohara in 1965.²⁰ Since then, transferred-electron oscillators and amplifiers have proliferated as have the papers, or at least the Letters to the Editor, describing them. So, at this point, the writer has chosen to be arbitrary and to select a few papers that seem to him to be particularly noteworthy out of the many published.

* The bandgap E_g in gallium arsenide is about 1.4 electron volts, and the excitation energy from first to second conduction band E_c (Fig. 1) is about 0.36 electron volt.

The first is a substantial paper on the theory of negative conductance amplification in "two-valley" semiconductors.²¹ The next two papers relate to the formation of domains in "two-valley" semiconductors and a new way of avoiding them.^{22,23} As noted earlier, Ridley and Watkins predicted the formation of domains in the presence of a perturbation. Since an rf signal is a perturbation, it can lead to the formation of domains. Suppose a domain forms at the cathode of a diode on the positive swing of the rf voltage. The electrons in the domain are in the second conduction band where the conductivity is low, so most of the applied voltage appears across the domain, as in Fig. 12. As a result, the field drops below critical elsewhere and

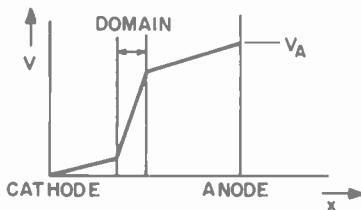


Fig. 12—The voltage distribution in a double-conduction-band semiconductor in the presence of domain.

nothing new happens until the domain drifts to the anode and disappears there. Then things can start over. The result is that the frequency of operation is determined by the transit time of the domain. It would be advantageous to remove this restriction. This is done by taking advantage of the time of the formation of a domain. The electronic relaxation time is

$$T = \frac{\epsilon}{\sigma} = \frac{\epsilon}{nq\mu_n}, \quad [45]$$

where (as a reminder)

- ϵ = permittivity,
- σ = conductivity,
- q = electron charge,
- n = electron density,
- μ_n = electron mobility.

Now, an electron moves with saturation velocity v_s at the high fields

used in these devices. Hence, in a relaxation time an electron moves a distance

$$l = v_s T = \frac{\epsilon v_s}{nq\mu_n} . \quad [46]$$

So, if the device has a length l and

$$nl > \frac{\epsilon v_s}{q\mu_n} \text{ cm}^{-2} , \quad [47]$$

a domain can form and if

$$nl < \frac{\epsilon v_s}{q\mu_n} \text{ cm}^{-2} , \quad [48]$$

a domain cannot form. The "magic number" for gallium arsenide is

$$\frac{\epsilon v_s}{q\mu_n} \sim 10^{12} . \quad [49]$$

If nl is kept less than 10^{12} , the entire bulk of the semiconductor displays a negative conductance, and devices with more than an octave of tuning range or bandwidth are possible. Perlman has recently described a transferred-electron amplifier with a bandwidth of 4 GHz at a 9 GHz center frequency.²⁴

In 1966 Copeland found another way of operating which he called the Limited-Space-Charge-Accumulation Mode (LSA mode).²⁵ The scheme consists in biasing the diode far beyond the critical field, in the valley of Fig. 11 or beyond, and then operating with a voltage swing that carries the voltage below the peak of the curve on its negative excursion. The frequency must be high enough so that a domain cannot form during its two excursions per cycle through the negative-conductance region. Hence, the diode delivers a high current during the negative rf voltage swing and a very small current during the positive swing. If the diode were a vacuum triode or tetrode, this manner of operating would be called Class B or Class C operation, depending on the bias point. The thing that makes this mode of operation possible is the voltage swing below the critical voltage.

Below the critical voltage the electron relaxation time is very short, roughly 1/20 of that at high voltage, so any incipient domain is quenched every cycle. Hence the condition for LSA operation is

$$T_1 \ll \frac{1}{f} \ll T_2, \quad [50]$$

where

T_1 = relaxation time in band 1,

T_2 = relaxation time in band 2,

or

$$1.4 \times 10^3 \ll \frac{n}{f} \leq 2 \times 10^5 \text{ cm}^{-3} \text{ sec} \quad [51]$$

for gallium arsenide. As with all Class B or C operation, the efficiency is high compared to "Class A operation" where the diode is biased in the negative-conductance region.

This mode of operation was seen by Fukui and Copeland in 1966,²² and in 1967 Kennedy and Eastman²³ obtained the remarkable result of 33 watts peak power output at X-band with an efficiency of 3.4%. Because of the extremely high power density in LSA operation at the high power of which the mode is capable, the duty cycle must be kept low.

Since this section started with Hilsum, it seems appropriate to end it with him also; recently he and Rees proposed the three-level transferred-electron oscillator.²⁵ It works.²⁶

5. Microwave Transistors

Transistors have been around a long time and the literature on them is massive. Therefore, only some aspects pertinent to microwave operation will be noted, as much to point up some of the problems that confront the transistor designer as anything else.

a. The Overlay Transistor

In principle, the bipolar transistor is very simple. It consists of two junctions back-to-back, one serving to inject carriers into the base region, the second to collect the carriers that have transmitted the

base. Because the collector can be back-biased to a high voltage, it can tolerate a large voltage swing, so with a high-impedance load, power gain is obtained. There the simplicity ends.

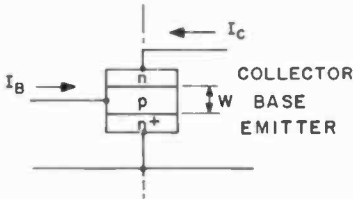


Fig. 13—A basic n-p-n transistor, common-emitter connected.

Consider an n-p-n transistor in a common-emitter circuit as shown in Fig. 13. When an electron is injected into the base, a hole joins it via the base connection to maintain charge neutrality. When the electron leaves the base and enters the collector, a hole leaves the base via the base lead. The result is a pair of pulses of base current separated by the transit time T as shown in Fig. 14. These pulses constitute that part of the base current that arises from high-frequency effects (recombination of holes and electrons in the base also give rise to a base current). In the rf case, an injected current of

$$i_e = i \sin \omega t \quad [52]$$

in similar manner gives rise to a base current

$$\begin{aligned} i_B &= i \sin \omega t - i \sin \omega(t - T) \\ &= 2i \sin \frac{\omega T}{2} \cos \omega \left(t - \frac{T}{2} \right) \end{aligned} \quad [53]$$

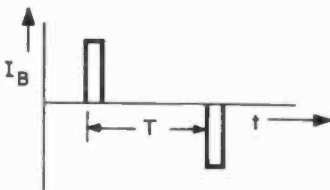


Fig. 14—Base-current pulses in a transistor with large base transit time.

For small transit angles, in-going and out-going currents cancel, but with a transit angle of 180° the base current becomes twice the injected current and the driving power becomes high. The obvious way to minimize the problem is to make the base thickness W small. The electrons move through the base with a velocity

$$v = \frac{D_n \partial n}{n \partial x} \sim \frac{D_n}{W}, \quad [54]$$

where

D_n = electron diffusion constant

n = electron density.

Hence the transit time is

$$T = \frac{W}{v} = \frac{W^2}{D_n}, \quad [55]$$

so reducing W pays off fast. There are limits on how far W can be reduced. For one thing, if the transistor is to operate with a high collector voltage, W must be large enough to prevent punch-through. In practice, W is reduced to a micron (10^{-4} cm) or less. Then connection to the base becomes mechanically difficult, so the emitter is formed by diffusing an n-type "dot" into the base as shown in Fig. 15.

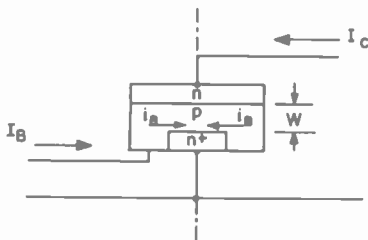


Fig. 15—A basic n-p-n transistor with diffused emitter, showing base-current flow.

Now, emitter and base connections can be made in the same plane, a distinct mechanical and electrical advantage. But now the base current flows radially along the emitter depletion layer and the voltage drop from edge to center "debiases" the center, so most of the injection takes place at the periphery of the dot. The result is an injection area

confined to the edge of the dot and a dead-head capacitance comprising the entire dot. The way to fix this unfavorable situation is to reduce the size of the individual dot and use many of them in parallel to maintain the desired current level. The result is the "overlay" structure shown schematically in Fig. 16.²⁷

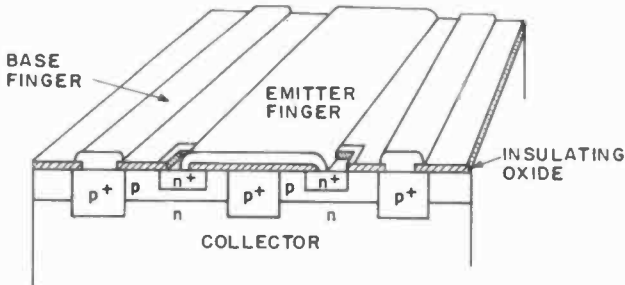


Fig. 16—An n-p-n transistor with overlay structure.

The RCA 40341 UHF transistor, using this structure, has 180 dots on 0.004-inch centers with a W of 0.070 inch. The small size of the structure and the tolerances required attest to the tremendous technology transistor engineers have developed.

While some high-frequency problems in bipolar transistors have been touched upon, not all have been, particularly the effects of high injection levels, which lead to base-widening and a variety of other effects. Many of these effects have not been studied to the point where a design procedure for circuits to utilize the transistor is available; so the best way to design a circuit is to set up the transistor in a circuit with enough degrees of freedom to obtain optimum performance at the required drive level, then remove the transistor and measure the impedances presented to the transistor by the input and output circuits. The procedure may sound inelegant but it works.

b. The Field-Effect Transistor

Recently there has been considerable interest in the field-effect transistor (FET) as a low-level, low-noise amplifier at microwave frequencies. Since the FET is a majority-carrier device, its electronic speed of response should be the electronic relaxation time

$$T = \frac{\epsilon}{\sigma}$$

about 10^{-12} sec for a conductivity σ of 1 ohm-cm. Regrettably, the electrodes hung on the semiconductor seem to reduce the maximum frequency at which gain is obtained.

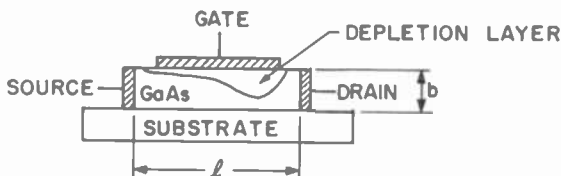


Fig. 17—A field-effect transistor with a Schottky-barrier gate.

The basic structure is as shown in Fig. 17. It consists of a bar of semiconductor, usually gallium arsenide because of its high mobility, on an insulating substrate, with a contact at each end and a plate on top. The contact at the left in the figure is the cathode, called the *source*, that on the right is the anode, called the *drain*, and the electrode on top is called the *gate* and the semiconductor beneath is called the *channel*. When biased negative, the gate becomes insulated from the semiconductor by a depletion layer. When the gate is made more negative the barrier layer widens, reduces the channel conductance, and ultimately cuts off the channel; and in this way control is achieved. The drain current is²⁸

$$I_D = GV_p \left[\frac{V_g}{V_p} - \frac{1}{3} - \frac{2}{3} \left(\frac{V_g}{V_p} \right)^{3/2} \right], \quad |V_d| > |V_g - V_p|, \quad [56]$$

where

$$G = \frac{wb}{l\rho_o} = \text{channel conductance.}$$

$$V_p = \frac{\rho_o}{2e\mu_n} b^2 = \text{punch-through voltage}$$

ρ_o = resistivity,

V_g = gate voltage,

V_d = drain voltage,

l = length,

b = thickness,

w = width.

imposed on the medium, and the equations are solved for the apparent dielectric constant ϵ' , then

$$\epsilon' = \frac{D}{E} = \epsilon \left[1 + \frac{k^2}{1 - \left(\frac{v}{v_s}\right)^2} \right], \quad [62]$$

where $k^2 = \frac{e^2}{c\delta} =$ electromechanical coupling coefficient

$v_s =$ velocity of sound

It will be noted that if v is made just a little larger than v_s , the dielectric constant becomes negative and one might expect something strange to happen. It does; if the velocity v is that of an electron stream that interacts with the piezoelectric field, the damping constant in the stream becomes

$$\alpha \sim \frac{-\frac{1}{2} k^2 \left(\frac{v}{v_s} - 1\right) \frac{\omega_R}{\omega}}{\left(\frac{v}{v_s} - 1\right)^2 + \left(\frac{\omega_R}{\omega}\right)^2 \left(1 + \frac{\omega^2}{\omega_R \omega_D}\right)^2}, \quad [63]$$

where $\omega_D = v^2/D =$ diffusion frequency,

$\omega_R = \sigma_0/\epsilon =$ electron relaxation frequency.

Hence the attenuation constant becomes negative when the electron velocity exceeds the sound velocity, so the wave grows. It was noted above that the experiments matched theory and they did in considerable detail:

1. The shapes of the curves of attenuation versus drift electric field matched theory.
2. The onset of amplification occurred at the expected electric field.
3. The maximum amplification occurred at the expected electric field.

The whole study was impressive and had many practical implications; the idea of a compact electrically variable delay line, particularly with gain, was enthralling.

However, coupling in and out with wide-band couplers proved formidable and terminating the sound waves at the ends proved equally

formidable. So now effort concentrates on passive delay lines using surface waves instead of bulk shear waves. Lithium niobate (LiNbO_3), because of its relatively low attenuation, is a favored material. Surface waves are easily quenched with a drop of fluid, such as acetone, or with Teflon. The wide-band coupling remains to be achieved.

Fig. 18 reminds me of a matter relating to traveling-wave devices which I mention with diffidence because it may seem trivial, yet I have seen such diagrams, with one line indicating input and another indicating output, misunderstood and misinterpreted. Consider the traveling-wave amplifier of Fig. 19. It has input and output couplers and

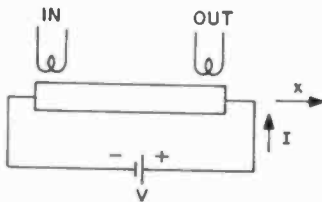


Fig. 19—Schematic representation of a traveling-wave amplifier.

passes a dc current I , so electrons move from input to output. Conservation of charge requires that

$$\frac{\partial j_x}{\partial x} + \frac{\partial \rho}{\partial t} = 0, \quad [64]$$

where j_x = current density,

ρ = charge density.

But, Gauss says

$$\rho = \epsilon \frac{\partial E}{\partial x} \quad [65]$$

so

$$\frac{\partial j_x}{\partial x} + \epsilon \frac{\partial^2 E}{\partial x \partial t} = 0, \quad [66]$$

which is integrable

$$j_x + \epsilon \frac{\partial E}{\partial t} = \text{a constant in } x = I/A \quad [67]$$

where A is the cross-sectional area of the device. Suppose, j_x consists of a dc component, j_o , as it must, and an ac component j_1 . Then

$$j_o = I/A \quad [68]$$

$$j_1 + \epsilon \frac{\partial E}{\partial t} = v. \quad [69]$$

Now, suppose the traveling-wave gain mechanism makes the convection current j_1 grow exponentially;

$$j_x = j_{x0} e^{ax}. \quad [70]$$

Then, the displacement current must go as

$$\epsilon \frac{\partial E}{\partial t} = -j_{x0} e^{ax}. \quad [71]$$

Now, the trick is to make input and output couplers that couple to only one component of the current. In practice, this is usually the convection current. Then there will be gain between couplers, even though the battery circuit doesn't know anything is going on.

7. The State of the Art

In assembling material for an assessment of the state of the art, the writer has relied on his own files and the files of co-workers who have kept abreast of progress in their own fields of interest. His own files consist in the main of charts, such as Fig. 20, to which points are added when new data are published, so that he can see at a glance the likely impact of new developments. To trace all of these data back to their original sources at this juncture would be an impossible task and would burden the paper with an enormous bibliography. Furthermore, the writer has been selective in his choice of data; all data on similar devices must conform to a pattern, any reasonable pattern, so that the data show a certain amount of self-consistency. He has had

the experience of designing equipment around a statistical fluctuation that turned out to be somewhat remote from the norm for a production run and would not wish anyone else a similar experience. Hence the data presented may show a tinge of conservatism.

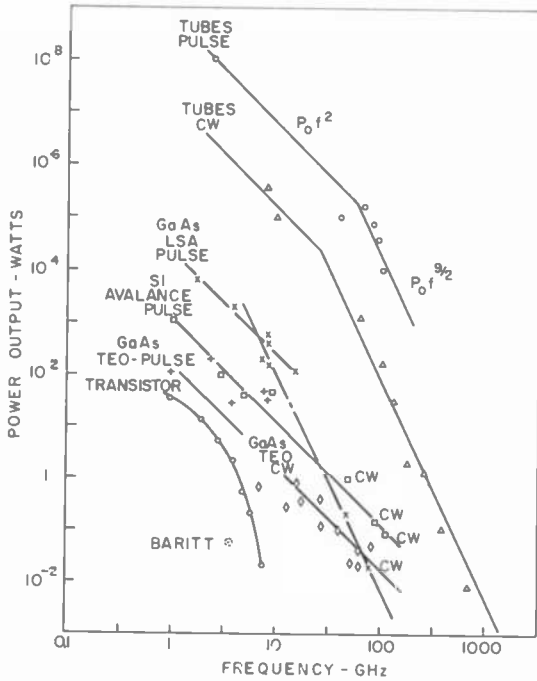


Fig. 20—The performance of power generators, vacuum tube and solid-state, versus frequency.

a. Power Generation

In his 1960 paper, the writer adduced arguments that the power output of any single device is circumscribed by fundamental limits to¹

$$P_o = j^2 \frac{\lambda^2}{\Delta\omega C}, \quad [72]$$

where P_o = power output
 j = current density

λ = wavelength of operation

$\Delta\omega = 2\pi \times$ the bandwidth

C = output capacitance per unit area as determined by space-charge considerations.

This is the well-known "Pf²" law. With the development of high-convergence electron guns for beam tubes, the current density may be determined by the field the device can tolerate rather than by the cathode itself. Then Eq. [72] may be written in another form which has the additional advantage that it applies equally to solid-state devices. The current density in a space-charge-limited device may be written²³

$$j = \frac{CV}{T} = \frac{\epsilon E_M}{T},$$
$$= \begin{cases} \frac{1}{4} C v_M E_M, & \text{for a vacuum device,} \\ \frac{1}{3} C v_M E_M, & \text{for a solid-state device,} \end{cases} \quad [73]$$

where

C = capacitance per unit area, as before,

ϵ = permittivity,

E_M = maximum tolerable field,

v_M = maximum electron (or hole) velocity,

T = transit time,

all under space-charge-limited conditions. Insertion of a combination of the above relations for j into Eq. [72] and reducing λ to $\lambda/2$, a more stringent limitation on moding, gives

$$P_{of} f^2 \leq \frac{c^2}{16} \frac{\omega}{\Delta\omega} \frac{v_M \epsilon_0 E_M^2}{\omega T}, \quad [74]$$

where ϵ_0 = permittivity of free space,

c = velocity of light.

The frequency and bandwidth are given by systems requirements; they are specifications to the device man. The transit angle, ωT , must

be of the order of unity at most to obtain efficiency. The maximum velocity is determined by the medium

$$v_M \leq \begin{cases} c & \text{for vacuum devices,} \\ v_s & \text{for solid-state devices,} \end{cases}$$

where

$$v_s = \text{saturation velocity} \sim 10^7 \text{ cm/sec,}$$

and the maximum tolerable field is

$$E_M \sim 10^5 \text{ volts/cm}$$

for both tubes and solid-state devices. Hence, one would expect the ultimate ratio of power from a single solid-state device to that of a single vacuum device to be

$$\frac{P_{SS}}{P_{VD}} \sim \frac{1}{3} \times 10^{-3}. \quad [75]$$

At the higher frequencies, Eq. [74] breaks down because circuit losses widen the bandwidth beyond that stipulated by systems requirements and the load is adjusted for maximum power output regardless of bandwidth. Then Eq. [74] becomes

$$P_o f^{3/2} \leq \frac{c^2}{64(2\pi)^2} \frac{\epsilon_o v_M E_M^2}{\epsilon K}, \quad [76]$$

where K is the factor that relates circuit resistance to frequency

$$r = Kf^{1/2}, \quad [77]$$

a skin-effect formula, so K embodies the properties of the materials of which the circuit is built and its geometrical configuration. As it turns out, Eq. [74] is valid up to about 30 GHz, and Eq. [76] above 30 GHz (see Fig. 20).*

The top curves in Fig. 20 show the performance of a variety of tubes: klystrons, magnetrons, and traveling-wave tubes. All have been

* Eq. [74] may apply to lasers as well. This possibility is explored in Appendix A.

brought to comparable states of performance. The topmost point is a "spectacular" but is included because it is the highest power reported and lies within gunshot of the value predicted by Eq. [74].³⁴ At the lower frequencies, the cw power available is about

$$P_o f^2 = 10^4 \text{ kW (GHz)}^2 \quad [78]$$

an advance of about 10^2 over the situation ten years ago. In addition, there is remarkable progress at the higher frequencies, extending into the millimeter-wave range.

The power output of solid-state devices lies below that of vacuum tubes by a factor of about 10^6 . If Eq. [75] is to be believed, the disparity will not shrink by more than a factor of about 10^3 . The most spectacular of the solid-state devices with respect to power are the LSA devices. However, as noted earlier, because of the high power densities in this mode of operation, duty cycles must be kept low, of the order of 10^{-6} . Above 10 GHz they have been operated under cw conditions and the plot looks like it might turn out to be $Pf^{0.2}$; it is too early to say. Silicon avalanche diodes have high efficiencies, particularly in the anomalous (trapatt) mode, and their performance as cw devices at the higher frequencies is also impressive in terms of power at frequency. The gallium arsenide TEO's lie a little below the silicon devices in the figure. However, power output is not the only measure of utility and, if they are indeed less noisy than the avalanche diodes, they may well take over local oscillator applications. Transistors have the advantage that they are three-terminal devices at the outset, so their application as amplifiers is straightforward.

All of the oscillators can in principle be made into amplifiers by overloading the circuit so the negative resistance of the device falls just short of cancelling the circuit loss. This manner of operation used to lead to awkward circuits, but the invention of a compact microstrip circulator has made the separation of input and output simple and elegant.³⁵ The wide bandwidth available from TEA's makes them contenders with traveling-wave tubes and a considerable part of the microwave spectrum has already been covered by such devices, in the main by Fred Sterzer and his co-workers at RCA, Princeton. The coverage is shown in Fig. 21.

So much for power generation.

b. Small-signal devices

While the major effort has been devoted to power generation the past ten years, there has been some progress on small-signal devices. Some

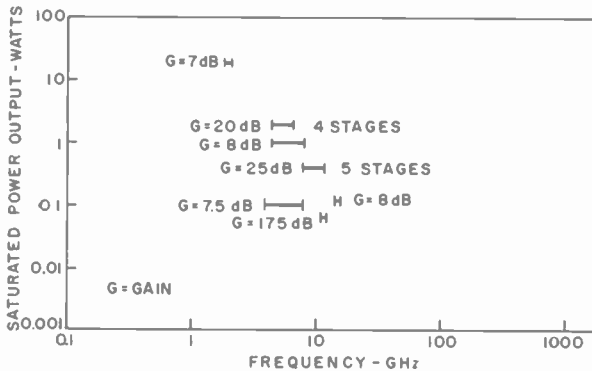


Fig. 21—The power output of a group of transferred-electron amplifiers versus frequency to show the frequency coverage.

of the older devices, notably the parametric amplifier and tunnel-diode amplifier, have matured and are in service. The field-effect transistors for microwave frequencies are still pretty much in the laboratory, but show great promise. The good old standby, the “crystal mixer,” continues to improve as the cutoff frequency is pushed upward, and its performance, even at 90 GHz, is respectable.

The crucial characteristics of a small-signal amplifier are its gain and noise figure, the former because it determines the contribution of the following amplifier stage to the overall noise figure. To display the noise properties of the older, mature devices and of the new devices,

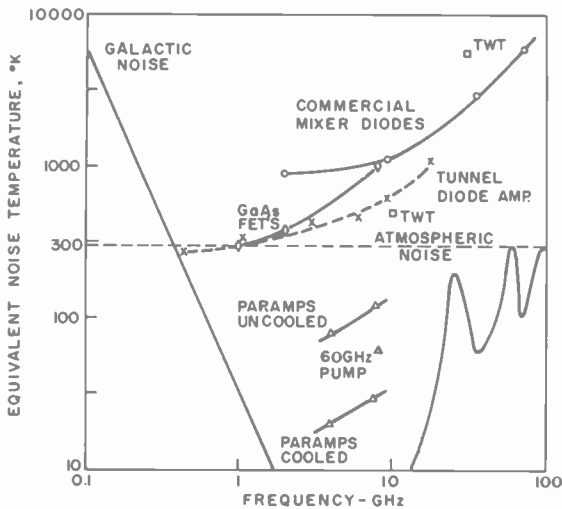


Fig. 22—The noise performance of a number of low-noise devices; parametric amplifiers, tunnel diodes, field-effect transistors and diode mixers.

their noise temperatures have been plotted versus frequency in Fig. 22. As is customary, the noise temperatures have been computed from

$$T_N = T_o(F - 1),$$

where T_N = equivalent noise temperature,

T_o = reference temperature (300°K in this case),

F = noise figure.

At the left in the figure is shown the noise temperature of galactic noise sources versus frequency; on the right, the noise temperature of the atmosphere with its two "windows" below 100 GHz. As is well-known, noise temperatures below these curves buy nothing in performance for upward-looking applications and noise temperatures below 300°K buy nothing for links where the signal must traverse the atmosphere.

1. Parametric amplifiers

Parametric amplifiers find their major application in satellite communication links where their outstanding performance really pays off. Uncooled parametric amplifiers achieve noise temperatures of about 100°K in S-band to X-band; and cooled amplifiers have noise temperatures of about 30°K in the same bands. The development of compact cryogenic refrigerators has made the cooled amplifier practical. The result of such cooling is the low noise figure and a stable amplifier, whereas an uncooled amplifier must be temperature compensated to keep the noise temperature from wandering. S- and K-band points for cooled and uncooled amplifiers are shown in Fig. 22. Between the lines connecting the pairs of points is a point for an uncooled amplifier pumped at a very high frequency (about 60 GHz). As stable high-frequency local oscillators of adequate power become available, noise temperatures may well drop even lower.

It is noted in passing that a parametric amplifier is itself a refrigerator. A thermodynamic derivation of the noise temperature of a parametric amplifier appears in Appendix B.

2. Tunnel-diode amplifiers

A plot similar to Fig. 22 ten years ago showed just one point on a tunnel-diode amplifier with a noise temperature of about 1200° at 4.5 GHz. Now tunnel-diode amplifiers have been operated up to about 18

GHz. As shown in Fig. 22, their performance is adequate for earth-bound links up to about 10 GHz and exceeds the performance of diode mixers up to the top point at about 18 GHz.

Thus the tunnel-diode amplifier is a simple and adequate amplifier for many applications, for example, weather radars.

3. Field-effect transistors

The performance of a few experimental field-effect transistors is shown in Fig. 22 by points that lie just above the tunnel-diode curve. The noise performance does not yet match that of tunnel-diode amplifiers except at frequencies below one GHz or so, but they are three-terminal devices, so require no circulator, and time may well improve their performance considerably.

4. Diode mixers

The topmost curve in Fig. 22 shows the performance of commercially available diodes as mixers. At 10 GHz they are matched by experimental field-effect transistors and outperformed by tunnel-diode amplifiers. But, as usual, at the frontier of the spectrum they stand alone, as they always have.

5. Acoustoelectric amplifiers

There is nothing to say except that they have been made to amplify. The principal immediate result of the work may well be the interest in surface waves and their application in delay lines and other signal-processing devices. The problem of broad-band coupling to signals of such minute wavelength (about 10^{-4} cm at 1 GHz) is formidable.

In the foregoing, nothing has been said about masers. Their role as low-noise amplifiers seems to have been preempted by parametric amplifiers in commercial service and they are to be found largely in radio telescopes where the ultimate in noise temperatures is required.

8. Conclusion

The past decade has brought remarkable progress in a number of areas:

1. The power output of transmitting tubes has increased about two orders of magnitude. This has been the result of refinement in engineering; no new principles of operation are involved.
2. Solid-state power sources, which were not even discussed in

a similar paper ten years ago, now dominate many applications up to L-band and they have been pushed up in frequency to about 100 GHz. There are a variety of such devices: transistors, avalanche diodes, transferred-electron devices, and now the baritt. It will take time for each to find its proper applications.

a. Transistors seem to be bogging down at about X-band. Hopefully, this is temporary.

b. Avalanche diodes in the anomalous (trapatt) mode dominate in pulse applications below C-band. Transferred-electron devices in the LSA mode do not produce the average power required in many applications.

c. Transferred-electron devices in the stable mode show promise of displacing traveling-wave tubes at modest power levels. Their bandwidth is impressive.

3. In the low-noise field, the promises of ten years ago for tunnel-diode and parametric amplifiers have been fulfilled in major part and they have found their role in communications. The field-effect transistor is beginning to challenge the tunnel-diode amplifier and it would occasion no surprise to the writer if it matched or overtook the tunnel diode in a few years. The crystal mixer, like the super-regenerative receiver, will always work when nothing else does. It has been a fruitful decade.

Acknowledgments

The writer gratefully acknowledges his indebtedness to Messrs. R. F. Ciafone and C. C. Foster, Jr., who supplied the impetus for this paper; to K. K. N. Chang, B. Hershenov, L. S. Napoli, and C. P. Wen who supplied background information, data, references, and advice as needed. I am grateful to all.

Appendix A

This appendix is devoted to an heuristic derivation of the formula

$$P_{of} f^2 \leq \frac{c^2}{16} \frac{\omega}{\Delta\omega} \frac{v_M E_M^2}{\omega T} \quad [74]$$

in a form that permits its application to lasers. The result is then compared with the performance of lasers.

Consider a diode of length l and cross section A through which pass particles of density n per unit volume at an average velocity v . In the course of transit each particle gives up an energy $\Delta\epsilon$, of uncertain amount, which appears as power output. Then the power output of the device is

$$P_o = Avn\Delta\epsilon. \quad [79]$$

All that is known of $\Delta\epsilon$ is that it satisfies the Heisenberg uncertainty principle, i.e.,

$$\Delta\epsilon\Delta t = h/2\pi, \quad [80]$$

where Δt = the uncertainty in time at which $\Delta\epsilon$ is given up,

h = Planck's constant.

Then

$$P_o = \frac{Avnh}{2\pi\Delta t}. \quad [81]$$

If this is multiplied, top and bottom, by the frequency ν (f in engineering nomenclature), the result is

$$P_o = \frac{Avnh\nu}{2\pi\nu t}. \quad [82]$$

Now, the uncertainty in time is measured by the spectral linewidth of the emission, so

$$\frac{\Delta t}{T} = \frac{\Delta\nu}{\nu}, \quad [83]$$

where $\Delta\nu$ = line width

$$T = l/v \\ = \text{average transit time} \quad [84]$$

Hence

$$\begin{aligned}
 P_o &= \frac{A\nu nh\nu}{2\pi T\Delta\nu} \\
 &= \frac{\nu}{\Delta\nu} \frac{A\nu nh\nu}{2\pi\nu T}
 \end{aligned}
 \tag{85}$$

$$= \frac{A\nu h\lambda}{2\pi T\Delta\lambda},
 \tag{86}$$

where

$$\lambda = c/\nu = \text{wavelength of the emission}$$

Eq. [85] is the form in which the formula will be checked against laser performance.

To obtain Eq. [74] consider Eq. [84]. Write

$$A = (\lambda/2)^2 = (c/2f)^2,
 \tag{87}$$

and

$$\nu \sim v_M/4,
 \tag{88}$$

as in Eq. [74], and express the energy density in electrical terms

$$nh\nu = \epsilon E^2
 \tag{89}$$

Then

$$P_o f^2 \sim \frac{c^2}{16} \frac{\omega}{\Delta\omega} \frac{v_M \epsilon E^2}{\omega T}
 \tag{90}$$

which is Eq. [74].

Now consider Eq. [85] again to derive the laser equation. The laser current density is

$$J = nqv,
 \tag{91}$$

where q is the particle charge, so

$$nv = J/q. \quad [92].$$

In terms of J , Eq. [85] becomes

$$P_o = A \frac{Jh\lambda}{2\pi Tq\Delta\lambda}. \quad [93].$$

Now consider three lasers in turn; a GaAs injection laser, a $\text{CO}_2\text{N}_2\text{Ne}$ laser and a YAG laser.

a. The GaAs Laser

The emission wavelength and line width of a particular GaAs laser are shown in Columns 1 and 2 of Table 1. The operating current density and junction area are shown in Columns 3 and 4. The transit

Table 1—Lasers

| Column | 1 | 2 | 3 | 4 | 5 | 6 | 7 |
|----------------------------------|-----------|-----------------|---------------------------|--------------------|---------------------|--------------------|----------------|
| Quantity | λ | $\Delta\lambda$ | J | A | T | P_o Calc | P_o Meas. |
| Units | Å | Å | A/cm ² | cm ² | Sec. | Watts | Watts |
| GaAs | 9000 | 2 | 5×10^4 | 5×10^{-4} | 5×10^{-12} | 16 | 10 |
| $\text{CO}_2\text{N}_2\text{Ne}$ | 10570 | 10 | $3 \times 10^{-2\dagger}$ | 1 | 10^{-10*} | 10 ² /m | 75/m |
| YAG | 10650 | 3 | $5 \times 10^{11\dagger}$ | 10^{-1} | 2×10^{-4} | 530 | 200 |

* Per mean free path

† At 1000 volts/cm

‡ $J = n q C$

time (Column 5) is the junction thickness divided by saturation velocity;

$$T \sim \frac{10^{-4}}{2 \times 10^7} = 5 \times 10^{-12} \text{ sec.} \quad [94]$$

Substitution of the quantities in the first five columns in Eq. [92] yields

$$P_o = 16 \text{ watts. (Column 6).}$$

The measured value was

$$P_o = 10 \text{ watts. (Column 7).}$$

b. The $\text{CO}_2\text{N}_2\text{Ne}$ Laser

Consider the laser as a series of diodes each having a length equal to the ionization distance. The ionization potential is about 20 volts and the ionization distance is about 1/50 centimeter.³⁶ Hence, the electric field should be

$$E = 20 \times 50 = 1000 \text{ volts/cm,}$$

which is indeed the operating voltage. Again, the operating parameters are shown in the first four columns of Table 1. The transit time per ionization length is

$$T = \frac{L}{\bar{v}} \quad [93]$$

where \bar{v} is the average electron velocity for a "hot" electron

$$\bar{v} = \sqrt{\frac{qEL}{2m}}, \quad [94]$$

and

$$\begin{aligned} L &= \text{ionization distance,} \\ E &= \text{electric field strength} \\ m &= \text{electron mass} \end{aligned}$$

Substitution of the values cited above in Eq. [93] and [92] gives $T \sim 10^{-10}$ sec.

Then substitution of all pertinent values in Eq. [82] gives a calculated value for the power output of $P_o = 100$ watts per meter (Column 6) against a measured value of $P_o = 75$ watts per meter (Column 7).

c. The YAG ($\text{N}_D^{3+}:\text{Y}_3\text{Al}_5\text{O}_{12}$) Laser

The only particles that move in a YAG laser are photons, so the computation of the current gets a little tremulous. But since this computation is heuristic at the outset, assume the current is the doping density times the velocity of the photons (the velocity of light) times the electronic charge

$$\begin{aligned}
 J &= nqC, \\
 &= 10^{20} \times 1.6 \times 10^{-19} \times 3 \times 10^{10} \\
 &\sim 5 \times 10^{11} \text{ amp/cm}^2.
 \end{aligned}
 \tag{95}$$

The pertinent operating data are shown in Table 1, as are the calculated power output

$$P_o = 530 \text{ watts},$$

and the measured value

$$P_o = 200 \text{ watts}.$$

Appendix B—The Parametric Amplifier as a Carnot Engine

As is well known, the noise temperature of an ideal parametric amplifier is

$$T_n = \frac{\omega_s}{\omega_i} T_i, \tag{96}$$

where ω_s is the signal frequency, ω_i is the idler frequency, and T_i is the temperature of the idler circuit.³⁸ Since T_n can be made less than T_i by making the idler frequency higher than the signal frequency, the device, so operated, is obviously a refrigerator. If so, it should be amenable to thermodynamic treatment in the manner of Einstein for a system with a single degree of freedom and of Nyquist for a system of many degrees of freedom.^{38, 39}

So, consider an electrical Carnot engine in which changes in intrinsic energy are given by⁴⁰

$$dU = TdS - \phi dQ, \tag{97}$$

where

T = temperature,

S = entropy,

ϕ = electrical potential,

Q = electrical charge.

Then the Carnot cycle looks as shown in Fig. 23. Along the isothermals T_1 and T_2

$$\phi Q = RT,$$

the gas law, where R is the gas constant. Along the adiabatics A_1 and A_2 ,

$$\phi = Q^\gamma = \text{constant}, \quad [98]$$

where γ is the ratio of the specific heat at constant ϕ , C_ϕ , to the specific heat at constant Q , C_Q .

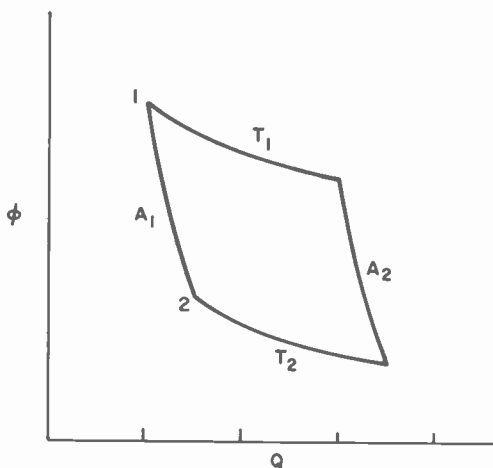


Fig. 23—Carnot cycle of a parametric amplifier.

Consider points 1 and 2 in the diagram. At point 1

$$\phi_1 Q_1 = RT_1 \quad [99]$$

at point 2

$$\phi_2 Q_2 = RT_2. \quad [100]$$

Because points 1 and 2 are connected by an adiabatic

$$\phi_1 Q_1^\gamma = \phi_2 Q_2^\gamma. \quad [101]$$

In a one-dimensional system, one-dimensional in the sense that only current flow along the length of a conductor is significant, ϕ and Q are connected by

$$Q = C\phi, \quad [102]$$

where C is a capacitance. Hence

$$Q_1 = C_1\phi_1, \quad [103]$$

and

$$Q_2 = C_2\phi_2. \quad [104]$$

Elimination of ϕ and Q in Eqs. [99], [100], and [101] yields

$$\frac{T_2}{T_1} = \left(\frac{C_1}{C_2} \right)^{\frac{\gamma-1}{\gamma+1}} \quad [105]$$

In a one-dimensional gas

$$C_v = \frac{1}{2} R \quad [106]$$

and

$$C_p = R + C_v = \frac{3}{2} R. \quad [107]$$

By analogy

$$C_\phi = \frac{1}{2} R \quad [108]$$

$$C_Q = \frac{3}{2} R \quad [109]$$

so

$$\gamma = \frac{C_Q}{C_\phi} = 3. \quad [110]$$

Hence

$$\frac{T_2}{T_1} = \left(\frac{C_1}{C_2} \right)^{1/2}. \quad [111]$$

If the engine comprises the (driven) capacitor C and a constant inductance L , Eq. [111] can be written

$$\frac{T_2}{T_1} = \left(\frac{LC_1}{LC_2} \right)^{1/2} = \frac{\omega_2}{\omega_1}, \quad [112]$$

where ω_1 and ω_2 are the resonance frequencies at points 1 and 2, respectively, or the resonance frequencies of any two points on the isothermals T_1 and T_2 connected by an adiabetic. So, if the engine is operated as a refrigerator, absorbing heat at a temperature T_2 and discharging heat at a temperature T_1

$$T_2 = \frac{\omega_2}{\omega_1} T_1, \quad [113]$$

which is the relation sought (Eq. [96]).

Furthermore, the efficiency of a Carnot engine is

$$\eta = 1 - \frac{E_1}{E_2} = 1 - \frac{T_1}{T_2}, \quad [114]$$

where E_1 is the heat energy discharged (or absorbed) at T_1 and E_2 is the heat energy absorbed (or discharged) at T_2 . If the engine is driven cyclically at a constant rate, the average heat energy discharged per unit time is the power P_1 and the average heat energy absorbed per unit time is the power P_2 . Hence

$$\eta = 1 - \frac{P_2}{P_1} = 1 - \frac{\omega_2}{\omega_1}, \quad [115]$$

and

$$\frac{P_1}{\omega_1} = \frac{P_2}{\omega_2}. \quad [116]$$

Thus, the Carnot engine satisfies a Manley-Rowe relation.⁴¹ It should be noted that the Manley-Rowe relations were originally derived by a consideration of coherent signals coupled by a variable reactance. The present relation (Eq. [116]) shows the same coupling between incoherent signals coupled by a variable reactance. That this should be so has been tacitly assumed in computations of the noise temperature of parametric amplifiers. It is not surprising, perhaps merely reassuring, that the result can be obtained from a thermodynamic argument.

References:

- ¹ L. S. Nergaard, "Amplification—Modern Trends, Techniques and Problems," *RCA Review*, Vol. 21, No. 4, p. 485, Dec. 1960.
- ² For a more complete, but equally simple discussion of semiconductors, see the first few chapters of *Microwave Solid-State Engineering* edited by L. S. Nergaard and M. Glicksman, D. van Nostrand Company, New York, N. Y. 1964. The chapters on the physics of the devices covered are valid, the state-of-the-art chapters are obsolete.
- ³ W. T. Read, "A Proposed High-Frequency Negative-Resistance Diode," *B.S.T.J.*, Vol. 37, No. 2, p. 401, March 1958.
- ⁴ F. B. Llewellyn and A. E. Bowen, "The Production of Ultra-High-Frequency Oscillations by Means of Diodes," *B.S.T.J.*, Vol. 18, p. 280, April 1939.
- ⁵ R. L. Johnston, B. C. DeLoach, and B. G. Cohen, "A Silicon Diode Microwave Oscillator," *B.S.T.J.*, Vol. 44, No. 2, p. 369, Feb. 1965.
- ⁶ B. C. DeLoach and R. L. Johnston, "Avalanche Transit-Time Microwave Oscillators and Amplifiers," *IEEE Trans. Elect. Dev.*, Vol. ED-13, No. 1, p. 181, Jan. 1966.
- ⁷ H. J. Prager, K. K. N. Chang, and S. Weisbrod, "High-Power, High-Efficiency Silicon Avalanche Diodes at Ultra-High Frequencies," *Proc. IEEE*, Vol. 55, No. 4, p. 586, April 1967.
- ⁸ R. L. Johnston, D. L. Scharfetter, and D. J. Bartelink, "High-Efficiency Oscillations in Germanium Avalanche Diodes Below the Transit-Time Frequency," *Proc. IEEE*, Vol. 56, No. 9, p. 111, Sept. 1968.
- ⁹ A. S. Clorfeine, R. J. Ikola, and L. S. Napoli, "A Theory for the High-Efficiency Mode of Oscillation in Avalanche Diodes," *RCA Review*, Vol. 30, No. 3, p. 397, Sept. 1969.
- ¹⁰ P. A. Levine and S. G. Liu, *IEEE Trans. Solid-State Circuits*, Vol. SC-4, No. 6, p. 384, Dec. 1969.
- ¹¹ D. J. Coleman and S. M. Sze, *B.S.T.J.*, Vol. 50, No. 6, p. 1695, May-June 1971.
- ¹² W. Schottky, "Vereinfachte und erweiterte Theorie der Randschichtgleichrichter," *Z. Physik*, Vol. 118, No. 9 and 10, p. 539, 1942.
- ¹³ W. Schottky, *Phys. Zeit.*, Vol. 15, p. 872, 1914.
- ¹⁴ B. K. Ridley and T. B. Watkins, "The Possibility of Negative Resistance Effects in Semiconductors," *Proc. Phys. Soc.*, Vol. 78, No. 2, p. 293, Aug. 1961.
- ¹⁵ C. Hilsom, "Transferred Electron Amplifiers and Oscillators," *Proc. IRE*, Vol. 50, No. 2, p. 185, Feb. 1962.
- ¹⁶ B. K. Ridley, "Specific Negative Resistance in Solids," *Proc. Phys. Soc.*, Vol. 82, No. 6, p. 954, Dec. 1963.
- ¹⁷ J. B. Gunn, "Microwave Oscillations of Current in III-V Semiconductors," *Solid State Comm.*, Vol. 1, No. 4, p. 88, Sept. 1963; J. B. Gunn, "Instabilities of Current in III-V Semiconductors," *IBM Jour. Research and Development*, Vol. 8, No. 3, p. 141, April 1964; J. B. Gunn, *Plasma Effects in Solids*, p. 199, Dunod, Paris, 1965.
- ¹⁸ H. Kroemer, "Theory of the Gunn Effect," *Proc. IEEE*, Vol. 52, No. 12, p. 1736, Dec. 1964.
- ¹⁹ A. R. Hutson, A. Jayarawan, A. G. Chenoweth, A. S. Cornell, and W. L. Feldman, "Mechanism of the Gunn Effect from Pressure Experiment," *Phys. Rev. Letters*, Vol. 14, No. 16, p. 639, April 1965.
- ²⁰ H. W. Thim, M. R. Barber, B. W. Hakki, S. Knight, and M. Uenohara, "Microwave Amplification in a DC-Biased Bulk Semiconductor," *Appl. Phys. Letters*, Vol. 7, No. 6, p. 167, Sept. 1965.
- ²¹ D. B. McCumber and A. G. Chenoweth, "Theory of Negative-Conductance Amplification and of Gunn Instabilities in 'Two-Valley' Semiconductors," *IEEE Trans. on Elect. Dev.*, Vol. ED-13, No. 1, p. 4, Jan. 1966.
- ²² J. A. Copeland, "A New Mode of Operation for Bulk Negative Resistance Oscillators," *Proc. IEEE*, Vol. 54, No. 10, p. 1479, Oct. 1966.
- ²³ W. K. Kennedy, Jr. and L. F. Estman, "High-Power Pulsed Microwave Generation in Gallium Arsenide," *Proc. IEEE*, Vol. 55, No. 3, p. 434, March 1967.
- ²⁴ B. S. Perlman, "Microwave Amplification Using Transferred-Electron Devices in Prototype Filter Equalization Networks," *RCA Review*, Vol. 32, No. 1, p. 3, March 1971.

- ²⁵ C. Hilsum and H. D. Rees, "Three-Level Oscillator: A New Form of Transferred-Electron Device," *Electronic Letters*, Vol. 6, No. 9, p. 277, April 1970.
- ²⁶ C. Hilsum, J. B. Mullin, B. A. Prew, H. D. Rees, and H. W. Straughan, "Instabilities of InP 3-Level Transferred-Electron Oscillators," *Electronic Letters*, Vol. 6, No. 10, p. 307, May 1970.
- ²⁷ D. R. Carley, P. L. McGeough, and J. F. O'Brian, "The Overlay Transistor Part 1: New Geometry Boosts Power," *Electronics*, Vol. 38, No. 17, p. 71, Aug. 1965.
- ²⁸ *Field Effect Transistors*, edited by J. T. Wallmark and H. Johnson, Prentice-Hall, Englewood Cliffs, N. J., 1966.
- ²⁹ W. Shockley, "A Unipolar 'Field-Effect' Transistor," *Proc. IRE*, Vol. 40, No. 11, p. 1365, Nov. 1952.
- ³⁰ A. R. Hutson, "Piezoelectricity and Conductivity in ZnO and CdS," *Phys. Rev. Letters*, Vol. 4, No. 10, p. 505, May 1960.
- ³¹ A. R. Hutson, J. H. McFee, and D. L. White, "Ultrasonic Amplification in CdS," *Phys. Rev. Letters*, Vol. 7, No. 6, p. 237, Sept. 1961.
- ³² D. L. White, "Amplification of Ultrasonic Waves in Piezoelectric Semiconductors," *J. Appl. Phys.*, Vol. 33, No. 8, p. 2547, Aug. 1962.
- ³³ A. R. Hutson and D. L. White, "Elastic Wave Propagation in Piezoelectric Semiconductors," *J. Appl. Phys.*, Vol. 33, No. 1, p. 40, Jan. 1962.
- ³⁴ L. S. Nergaard, "Tubes and/or Solid-State Devices for Power Generation," *Micro-wave Jour.*, Vol. 13, No. 4, p. 65, April 1970.
- ³⁵ P. B. McCoreson and L. B. Anderson, International Electron Dev. Meeting, Section 6, Washington, D. C., Oct. 27, 1966.
- ³⁶ B. Hershenov, "X-Band Microstrip Circulator," *Proc. IEEE*, Vol. 54, No. 12, p. 2022, Dec. 1966.
- ³⁷ Sanborn C. Brown, *Basic Data of Plasma Physics*, John Wiley and Sons, Inc., New York, N. Y., 1959.
- ³⁸ This relation is frequently expressed as $G_N = (\omega_p/\omega_1) |G|$, where G_N is the noise conductance, and $|G|$ the magnitude of the input conductance (see, e.g., Ref. [1]).
- ³⁹ A. Einstein, *Ann. d. Physik*, Vol. 22, No. 3, p. 569, Nov. 1907.
- ⁴⁰ H. Nyquist, "Thermal Agitation of Electric Charge in Conductors," *Phys. Rev.*, Vol. 32, No. 1, p. 110, July 1928.
- ⁴¹ This approach is just that used to derive the Gibbs-Helmholtz Equation; see, e.g., Leigh Pace, *Introduction to Theoretical Physics*, p. 266, D. van Nostrand Co., New York, N. Y. 1928.
- ⁴² J. M. Manley and H. E. Rowe, "Some General Properties of Nonlinear Elements-Part I. General Energy Relationships," *Proc. IRE*, Vol. 44, No. 7, p. 904, 1956.

Resolving Power Functions and Integrals of High-Definition Television and Photographic Cameras—A New Concept of Image Evaluation

Otto H. Schade, Sr., Consultant

RCA Electronic Components, Harrison, N. J.

Abstract—This paper demonstrates that the resolving power of photographic and television cameras can be calculated for all possible amplitudes of periodic (three-bar) and single-bar input signals in the "active" gray-scale range of an external scene.

The volume of these resolving-power functions can be specified by a single figure of merit; the mean resolving power in the image. The measure gives equal weighting to all resolving-power values in a logarithmic gray scale of two (100-to-1 range) for periodic and nonperiodic bar test objects and a given scene contrast.

The more informative gray-scale resolving-power functions $f_r(S)$ for three-bar and single-bar test objects can be calculated or determined by observation and maintain a direct link with visual assessments of image detail at any gray-scale level. The criterion for resolving power is by definition a fixed detail signal-to-noise ratio for a given test object ($K = 3.6$ or 6 for the patterns used here), and other values can be specified for a higher probability of detection. It is evident that any figure of merit derived for a single gray-scale level (typically $S = 0.5$) may disagree with observer ratings when the significant detail in the scene does not occur at this level.

Numerical evaluations demonstrate that a high-definition return-beam vidicon camera can outperform an excellent aerial film camera of equal format, particularly at low contrasts.

The analysis shows further that the absolute detection efficiency of existing high-definition cameras (television and film) is at best more than three orders of magnitude lower than that of a "perfect" camera and that the low-light efficiency of the television camera can be improved substantially by providing electron multiplication in the sensor or in an intensifier stage preceding charge storage and signal readout.

Introduction

The oldest measure of image definition is the resolving power. As a subjective measure determined by observation, it requires no knowledge of the physical factors involved. Modern image analysis, however, has provided an understanding of the physics of image formation and has correlated resolving power with an objective criterion determined from the transfer functions of the external imaging process. An accurate prediction of the resolving power of a system can now be made from objective data.

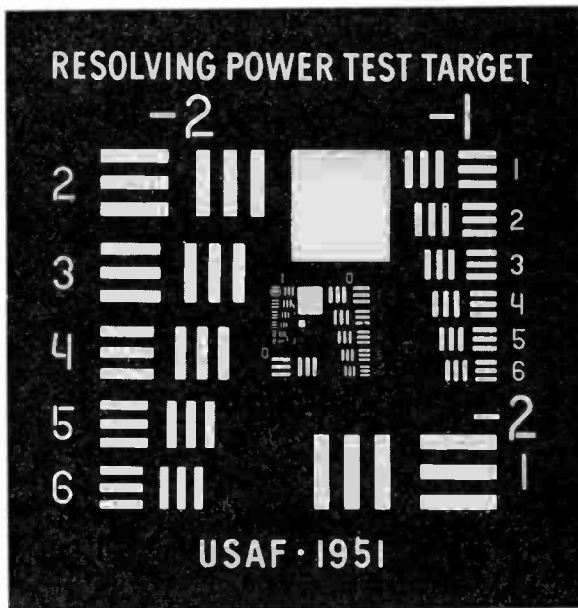


Fig. 1—Standard Resolving-Power Test target.

The objective criterion for the external imaging process is a detail signal-to-noise ratio $SNR_{\Delta}(f)$. This dimensionless quantity must have a certain value (K) for detection or recognition of a given test object in the presence of noise. This threshold value is a constant for a given type of test object independent of size provided the observer is permitted to adjust display brightness and magnification or viewing distance to optimum values for vision. A signal-to-noise ratio refers to a sampling area (\bar{a}), which is the area of the test object (a circle, square, or bar); in the case of complex objects, one may choose an elemental part of the test-object assembly such as the area of one

rectangular bar of the standard three-bar resolving-power test object shown in Fig. 1.

The threshold constant evaluated by psychophysical tests¹ for the bar area is $K = 3.6$ in a single image for a 50% probability, i.e., for resolving one of a pair of test objects in this test pattern.

Mathematical solutions for the resolving-power frequency (f_r) lead in general to simultaneous equations. One equation, the "threshold-function", expresses a factor or product (P) required by the threshold signal-to-noise ratio (K) as a function of spatial frequency. A second equation is set up to calculate the value (P) obtainable from the imaging system. This value equated to the threshold product yields the resolving-power frequency. An alternative method is to assume a resolving power (f_r) and product (P) and solve for an independent variable of the imaging system² such as the exposure or the conversion efficiency of the system.

A widely used threshold function is the sine-wave modulation factor $\bar{r}_{\text{thr}}(f)$ required for the threshold $\text{SNR}\Delta(f) = K$. The intersection of this function with the sine-wave modulation transfer function (MTF) of the system yields the resolving power frequency as illustrated by Fig. 2. The area bounded by these functions (MTFA) is a measure of the excess sine-wave response of the system. It has been proposed as a single figure of merit for rating image quality. Tests with aerial photographs of different contrasts and MTF's have given excellent correlation between the MTFA and photointerpreter ratings. A general acceptance of the MTFA as a unique quality measure, however, must be questioned for the following reasons.

The transfer functions of normal photographic cameras (film plus lens) are very much alike in shape, differing mainly by scale factors. It can be expected, therefore, that any rating based on a signal-to-noise ratio will rank images in the same order in agreement with observer judgment of quality. This is not the case, however, when a comparison is made of images having a different balance of MTF and noise, as illustrated by Fig. 2 for three systems having equal MTFA ratings. Figs. 2a and 2b show equal noise levels and threshold functions but very different resolving powers; Fig. 2c shows a very high MTF and a high noise level. When the exposure is reduced in the three systems by the same amount, the threshold functions have a higher slope (the slope angle is doubled in the figures as indicated by broken lines) and the MTFA's are no longer equal. This situation occurs in a single image at different gray-scale levels and depends not only on the shape of the MTF but on the balance of signal and noise determined by the relative exposure and the input contrast. Because important detail may

occur at a gray-scale level differing from the level for which the maximum resolving power or MTFA is determined, substantial differences can result with observer ratings.

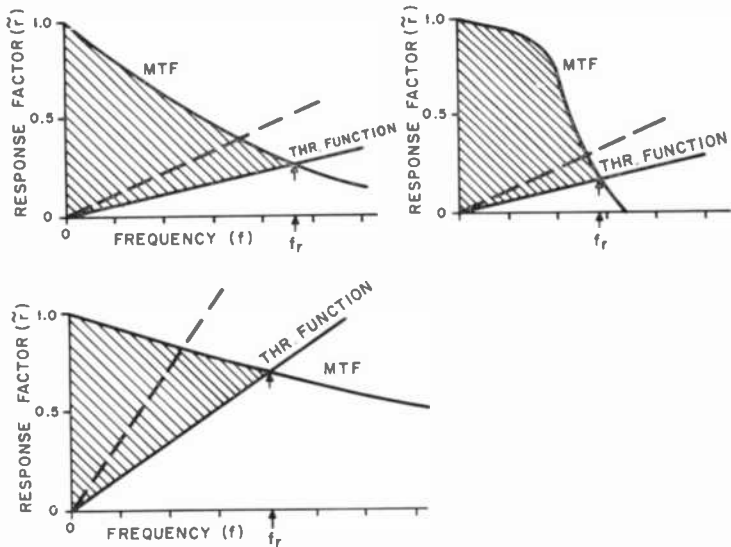


Fig. 2—Threshold functions and modulation transfer function areas (MTFA)

1. A New Concept of Image Evaluation

Detail signals, noise, and resolving power vary within the dynamic range of an image as a function of its active "video" gray scale (S). The active gray scale excludes haze and starts with $S = 0$ at the darkest part, the effective black level of the scene recorded by the sensor. The other end of the scale is the normalized value $S = 1$ located at the highlight level of the scene. This range contains all periodic and nonperiodic image detail displayed in the final copy. The haze of low-contrast scenes (below $S = 0$) is eliminated by "clipping" in the readout process (single-shot television readout) or in the copying process (film, normal fast-scan television) to restore a normal contrast for the active range in the final image by print-gamma control, regardless of scene contrast. This image processing does not change signal-to-noise ratios or resolving power when a perfect copying or display system is

used. Degradations introduced by the MTF or noise sources of a real display system can easily be included in the evaluation but are a separate problem that does not enter into a comparison of cameras.

A measure for the detail information contained in images made with different systems (photography, television) should be determined for a single-frame readout of the sensor image produced by a single-shot exposure of specified value, because sensors and readout systems may differ significantly in quantum and readout efficiency under different operating conditions (lag, saturation effects). The exposure may be optimized for each system when sensitivity is a secondary consideration.

Periodic Image Detail

The maximum possible amplitude of sine-wave or square-wave input signals that can exist at any given gray-scale level of the scene imaged on the sensor is limited by the exposure range $\Delta E = E_{\max} - E_{\min}$ to definite values as illustrated by Fig. 3a. The largest peak-to-peak square-wave amplitude in the scene is obviously $(E_{\max} - E_{\min})$ and occurs as a modulation of the gray-scale level $S = 0.5$. The maximum signal amplitude in the scene decreases linearly for lower or higher gray-scale levels because of the limits E_{\min} and E_{\max} . For high contrasts ($C_s \rightarrow \infty$) the exposure E_{\min} coincides with absolute zero; the maximum modulation factor of the gray-scale levels is unity for $S < 0.5$, decreases to lower values for $S > 0.5$, and becomes zero at $S = 1$.* The modulation $m_o = (C_s - 1)/(C_s + 1)$ normally specified by the contrast ratio $C_s = E_{\max}/E_{\min}$ is the absolute maximum value that can occur in a single image at the mean exposure level $E_s = (E_{\max} + E_{\min})/2 = E_{0.5}$. The general expression for the optical modulation $m_{o,s}$ at any gray-scale level and contrast is

$$m_{o,s} = a\rho_s m_o,$$

where a is an amplitude factor (zero to unity)

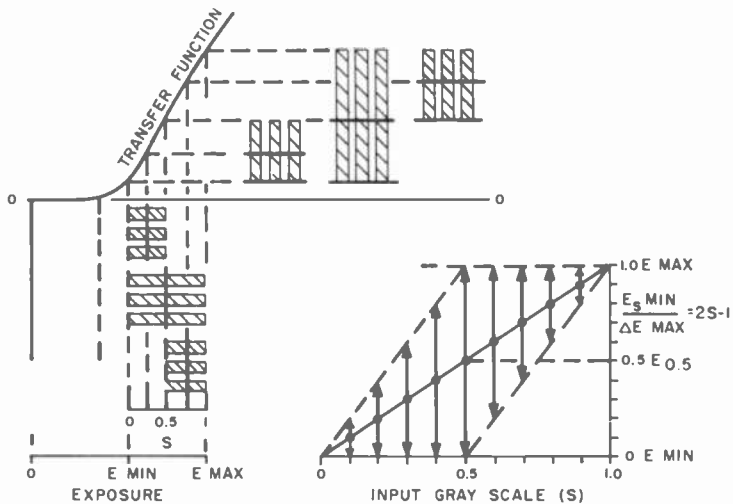
$$m_o = (E_{\max} - E_{\min}) / (E_{\max} + E_{\min})$$

$$\rho_s = m_{o,s} / m_o = (1 - S) / [0.5 + (S - 0.5)m_o] \quad \text{for } S > 0.5 \quad [1.1]$$

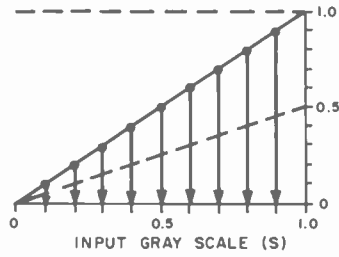
$$\rho_s = m_{o,s} / m_o = 2S / [1 - (1 - 2S)m_o] \quad \text{for } S < 0.5$$

The ratio ρ_s is plotted in Fig. 4 as a function of S . Exposure and gray-

* If the amplitudes are increased beyond these values the ac-axis of the waveform moves to a different S -scale level.



(A)



(B)

Fig. 3—Maximum input signal amplitudes for various gray-scale levels (S) in the active exposure range ($E_{max}-E_{min}$) of a scene: (a) periodic square-wave signals and (b) single-line signals.

scale level are related by the equation

$$E_s = E_{0.5} [1 + m_o(2S - 1)] \quad [1.2]$$

and depend on the scene contrast.

The complete resolving power functions of an image for periodic test objects are represented by the resolving-power volume Fig. 5a. The scales are logarithmic. Thus, the highlight range ($S > 0.5$) is relatively short. It is shown only for maximum signals. The broken diagonal lines are isometrics for constant resolving power in different

gray-scale levels. Numerical evaluation demonstrates that the functions $f_r(S)$ and $f_r(a)$, starting at any given level are virtually identical in shape and value, which allows specification of the total resolving power volume by a single function $f_r(S)$ for maximum amplitude $a = 1$. The "resolving-power area" specified by this function can vary for different systems because the shape of the function $f_r(S)$ is determined by the shape of the MTF and the values of signal and noise. A combination of low system noise and a low MTF results in a flatter curve than a higher system noise and a high MTF. Threshold or saturation limits cause a sharp decrease of resolving power.

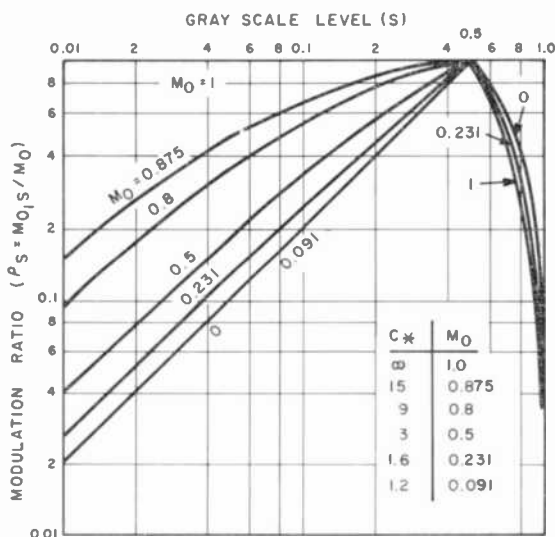


Fig. 4—Modulation ratio (ρ_s) as a function of gray-scale level (S) for various scene contrasts (Eqn. [1.1]).

The mean resolving power (MRP) in a 100:1 gray-scale range is a figure of merit defined in cycles/mm for a logarithmic gray scale by

$$\text{MRP} = \frac{1}{2} \int_0^2 f_r(S) d \log (100S) \quad [1.3]$$

Aperiodic Image Detail

Aperiodic detail signals (impulse signals) occur far more frequently in real scenes than do periodic signals. The resolving power of a system

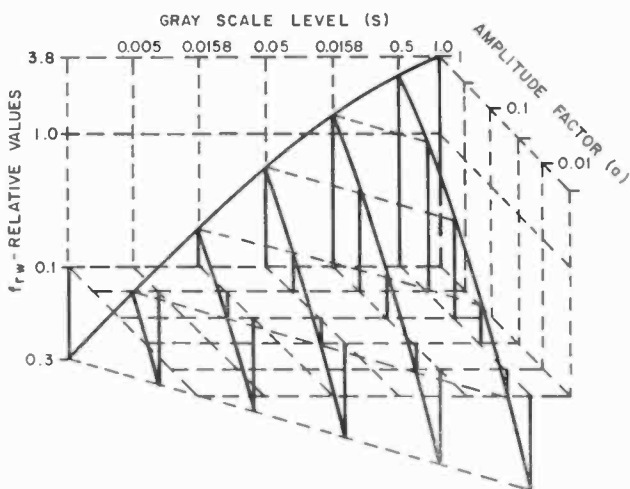
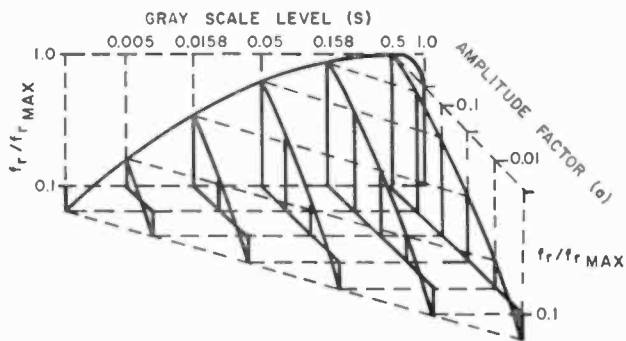


Fig. 5—Resolving power volumes for (a) three-bar test objects, (b) single-bar test objects.

to impulses generated by lines of various widths depends on the line signal amplitudes, the noise level, and the noise equivalent pass band (f_e), i.e., the integral of the squared sine-wave MTF of the system. In comparison with periodic test objects, the resolving power for single lines places more weight on a low noise level in the system and less weight on an extended frequency response, which contributes little to the integral (f_e).

A single bar of the standard three-bar test object (Fig. 1) is a convenient line test object. Although single-line test objects have a continuous frequency spectrum, it is common practice to express the

line width (W_o) of the test object in terms of a resolving-power frequency by the reciprocal value

$$f_{r,w} = \frac{1}{2W_o} \quad [1.4]$$

The line width (w_i) in the image is increased by the spread function of the system to an equivalent square pulse width

$$w_i = W_o(f_{r,w}/f_e) \quad [1.5]$$

where

$$f_e = \int_0^{f_{r,w}} \bar{r}^2(f) df$$

is the noise equivalent pass band of the system. Neglecting the small spread of the bar length, the mean amplitude of the signal pulse from the line object is decreased by the bandwidth ratio ($f_e/f_{r,w}$) and the noise is decreased by the square root of this ratio. Thus, the ratio $(f_e/f_{r,w})^{1/2}$ takes the place of the equivalent square-wave response factor ($r\bar{\Delta}$) in equations for the detail SNR. The threshold constant for single-bar test objects ($\bar{a} = 5w^2$) has the value $K = 6$ for a 50% probability of detection in a single image frame.*

The input signal will be defined as a "black" bar signal extending from the gray-scale level down to the picture black level $S = 0$. This choice results in pulse signal amplitudes increasing linearly with the gray scale to a maximum amplitude ($E_{\max} - E_{\min}$) at $S = 1$, as shown in Fig. 3b. Noise in a photographic system is determined by the mean exposure value

$$\bar{E} = 0.5[E_{\max} + E_{\min}][1 + m_o(S - 1)] \quad [1.6]$$

shown by a broken line half-way below the S -level. Thus, the pulse modulation is equivalent to a bidirectional modulation given by

$$m_{o,s} = m_o S [1 - (1 - S)m_o]^{-1} \quad [1.7]$$

The resolving-power volume for single-bar test objects is illustrated by

* The value K decreases to $K = 6/\sqrt{3} = 3.45$ in a normal television image (30 frames/sec) where the eye integrates 3 frames in a storage time of 1/10 second.

Fig. 5b. The functions $f_{r,w}(S)$ are more linear, attain considerably higher values than the periodic functions $f_r(S)$ for the same system, but decrease to lower values at low gray-scale levels because of the higher value of the threshold constant. The mean value

$$\overline{\text{MRP}} = (\text{MRP}_3 + \text{MRP}_1)/2 \quad [1.8]$$

of the resolving powers in the gray-scale range of the image is a figure of merit giving equal weight to periodic and aperiodic test signals.

The exposure of the sensor will be specified by the mean value $E_{0.5}$ of the total active exposure range. This value is a natural choice for resolving-power calculations, particularly for photographic cameras and intensifier television cameras where the mean signal level determines the noise level of the system. The noise of return-beam vidicons is essentially constant read-beam noise, because the beam current is determined by the high-light exposure (E_{max}). The mean exposure $E_{0.5}$ of the gray scale, however, is retained as a reference value for a comparative evaluation of resolving-power functions and is easily calculated from the maximum exposure.

High-definition return-beam vidicon (RBV) cameras operate normally in the single-exposure readout mode in which the beam reads out only the active exposure region. (The haze charges in the sensor are removed by an erase-prepare cycle before a new exposure.) The modulation Eqs. [1.1] and [1.2] and Fig. 4 are especially useful for photographic systems, whereas Fig. 3 leads to simpler relations for return-beam vidicons.

The calculation of the resolving-power functions and integrals for periodic and aperiodic line test objects is demonstrated in Sections 2, 3, and 4 for high-definition television and photographic cameras. The results are summarized in Section 6, which includes a discussion of the absolute detection efficiency of these cameras.

2. High-Definition Television Cameras

The derivation of basic equations for calculating the resolving power of film and television cameras from the transfer functions of the systems has been given in earlier papers^{1,2} and need not be repeated in detail. A brief discussion of the nonlinear sensor and readout transfer functions of return-beam vidicon (RBV) cameras is in order to set up equations and graphs for easy evaluation of the resolving power for the standard periodic three-bar test object as well as single-bar test objects as functions of exposure and gray scale.

2.1 The Sensor Transfer Function $V_s(E)$

The exposure E_{\max} is given in photometric units, lumen $s/m^2 =$ meter candle seconds (mcs) by

$$E_{\max} = 1.239 c(C_{(1)} V_E) 10^{-6} K_c \left(\frac{1}{\lambda_m \epsilon_m} \right) \quad [2.1]$$

where $c \geq 1$ is a dielectric trapping factor; $C_{(1)}$ is the sensor storage capacitance in picofarads per mm^2 ; V_E is the total potential caused by an exposure; ϵ_m is the quantum efficiency at λ_m , the wavelength (μm) of maximum energy response of the sensor; and $K_c = 680 [\int L(\lambda) w(\lambda) d(\lambda)] / [\int R(\lambda) w(\lambda) d(\lambda)]$ is the conversion factor lumens/watt. When the quantum efficiency of the sensor is independent of potential, the peak-to-peak video signal potential (V_{sm}), contrast ratio, and total sensor potential (V_E) are related by the simple equation

$$V_E = V_{sm} C_c / (C_c - 1), \quad [2.2]$$

which may be substituted into Eq. [2.1]. The quantum efficiency of antimony trisulfide sensors, however, is a function of polarizing potential. A typical function $\epsilon_m(V_p)$ for the compound antimony trisulfide-oxisulfide (ASOS) photoconductor used in high-resolution return-beam vidicons is given in Fig. 6a. The porous (SPS) layer used in standard 1-inch vidicons requires higher potentials, does not reach as high a quantum efficiency as the ASOS layer, and obeys a square law from $V_p = 10$ to 100 volts. Typical constants for ASOS sensors and 5000°K sunlight are $K_{5000} = 422$, $\lambda_m = 0.6$, $c = 1.5$, $C_{(1)} = 160$, yielding $E = 0.21 V_E / \epsilon_{0.6}$. For a polarizing potential V_{p0} of 20 volts, the exposure (E) calculated with Eq. [2.1] is $0.338 V_E$, shown by the broken lines in Fig. 6b. These linear functions are valid only at very small exposures because the effective polarizing voltage at the end of an exposure has decreased to $V_p = V_{p0} - (V_s + V_{\min} + V_d)$, where V_{\min} is the "haze" potential (caused by E_{\min}) and V_d is the charge potential from dark currents. As a consequence, the quantum efficiency decreases as a function of signal amplitude and progressively reduces the sensor "gamma", because the exposure for a given potential V_E must be increased for $C_c = \infty$ to

$$E_{\max} = E_{\max,0} (\epsilon_{V_{p0}} / \epsilon_{V_p}),$$

as shown by the solid-line function $V_{sm}(E_{\max})$. The signal potential for lower contrasts is an increment ΔV_s on the solid-line curve $C_c = \infty$

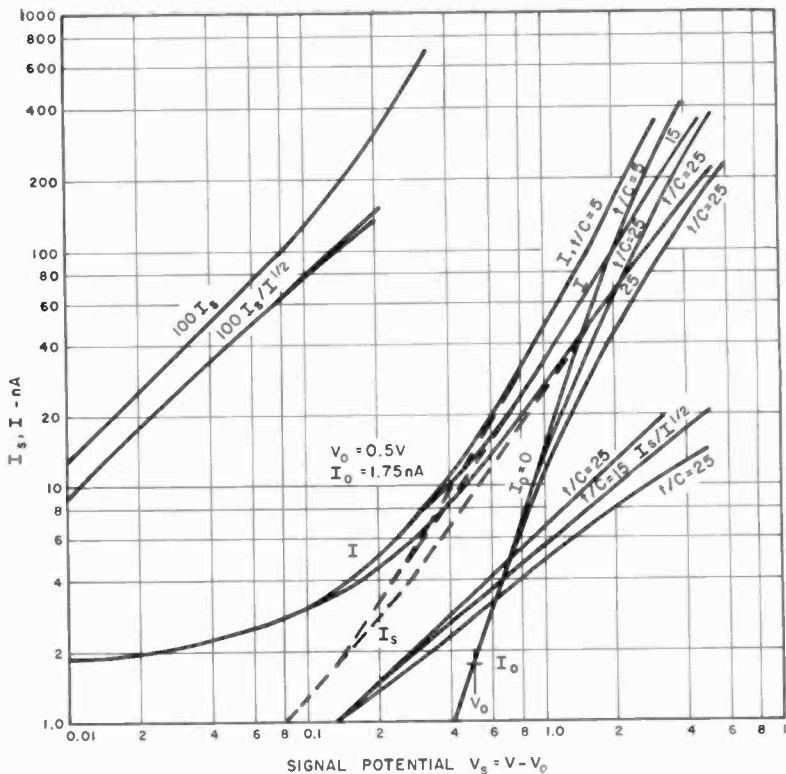


Fig. 7—Readout transfer functions $I(V_s)$ and $I_s(V_s)$ for the electron beam and optics of return-beam vidicons (18- μ m gun aperture) for $V_0 = 0$ and $V_0 = 0.5$ volt and three ratios (t/C).

where \bar{n}_{sr} is the number of signal electrons in the return beam, read out per sampling area \bar{a}_0 when the electron beam scans a large uniformly exposed area. There is no degradation of signals by the MTF of the camera. The mean squared noise in the denominator, however, depends on the size of the sampling area and is the sum of three noise powers: (1) the transferred noise from signal electrons, (2) the transferred noise from excess charges due to dark current and residual charges (V_d, V_r), and (3) the read-beam noise, which is the dominant noise component. All are expressed in terms of the number of signal electrons \bar{n}_{sr} in the return beam. The term $g\dot{\gamma}_r^2$ is the transfer factor for the mean squared noise.

Taking the square root and combining terms Eq. [2.3] simplifies to

$$\text{SNR}_{o(f)} = \left(\frac{\bar{n}_{sr}}{p + I_b'/I_{s0}} \right)^{1/2} \quad [2.4]$$

The signal current I_{s0} is measured in the sensor or target lead, not in the return beam, and I_b' is the beam current approaching the target. The number of signal electrons in the sampling area \bar{a}_o can be expressed by the total target signal current, $\bar{n}_s = I_{s0}t \times \tau_m \bar{a}_o / Ae$, and the sampling area by the frequency equivalent $1/4f^2$, leading to the equation

$$\text{SNR}_{o(f)} = \left(\frac{I_{s0}t\tau_m/e}{p + I_b'/I_{s0}} \right)^{1/2} (2fA^{1/2})^{-1} \quad [2.5]$$

where t is the readout time, τ_m is the mesh transmittance, e the electron charge, f the spatial frequency pass band of the camera, and A is the total sensor area. The factor p is the transferred target noise term discussed subsequently.

The detail signal to noise ratio $\text{SNR}_\Delta(f)$ for a bar test pattern is obtained by changing the square sampling area \bar{a}_o to a rectangular area $\bar{a} = \bar{a}_o(l/w)$ and the large-area signal current to a difference signal $I_s = I_{s0}r\bar{\Delta}$, reduced in amplitude by the square-wave response factor $r\bar{\Delta}$ of the camera.* (The square-wave modulation transfer function $r\bar{\Delta}(f)$ is abbreviated by MTF_Δ in this paper.) Thus,

$$\text{SNR}_{\Delta(f)} = \text{SNR}_{o(f)}(l/w)^{1/2}r\bar{\Delta},$$

and with Eq. [2.5],

$$\text{SNR}_{\Delta(f)} = \left(\frac{I_{s0}t(l/w)\tau_m/e}{p + I_b'/I_s} \right)^{1/2} r\bar{\Delta}(2fA^{1/2})^{-1}. \quad [2.6]$$

The input signal modulation (m_o) does not appear as a signal term because haze charges from the exposure E_{\min} are not read out in the single-exposure readout mode of operation. It follows that *beam noise* is determined only by the signal component of the exposure and *is not a function of contrast!* The noise in the sensor, however, is a function of input contrast or modulation (m_o) as shown by the expression for the transferred sensor noise

* The response factor $r\Delta_f$ is calculated from the sine-wave response factor r_f with $r\Delta_f = [8/\pi^2][r_f + (1/9)r_{3f} + (1/25)r_{5f} + \dots]$. For $r_f < 0.7$, the first term is sufficient.

$$p = \eta_c \tau_m \dot{\gamma}_r^2 \rho_w^2 \left(\frac{1}{2m_o} + \frac{V_d + V_r}{V_s} \right). \quad [2.7]$$

The product $\eta_c \tau_m \dot{\gamma}_r^2$ is the transfer factor for mean squared noise, and $\rho_w = (f_e/f)^{1/2}$ expresses the noise bandwidth reduction caused by the MTF product of the sensor and readout system. The maximum contribution of sensor noise to the total noise occurs at low contrasts (small values m_o) and can be assessed by comparing the magnitude of p with the beam noise I_b'/I_s . It is easily seen by inspection of Eqs. [2.6] and [2.7] that the worst-case condition occurs at high exposures, low contrast, and maximum signals, where the readout efficiency η_c is high, m_o is small and I_b'/I_s has a minimum value.

Numerical evaluations with typical constants show that the total rms noise is increased approximately 8% by target noise at high signal currents (100 nA). The rms noise contribution by p decreases to 4% at $1/2$ signal amplitude and becomes negligible for lower signals or higher contrasts. Thus, target noise is a second order effect in these cameras and can be neglected to simplify Eq. [2.6] to the following form,

$$\text{SNR}_{\Delta(f)} \simeq I_s \left(\frac{t(l/w) \tau_m m_b}{eI} \right)^{1/2} r\bar{\Delta} (2f\sqrt{A})^{-1}, \quad [2.8]$$

where I_b'/I_s is replaced by $I/I_s m_b$ and $I = (I_o + I_s)$ is the total readout current. It follows that the noise is "white" noise as in a photographic system, because the significant noise source is located at the camera output.

The $4\frac{1}{2}$ inch return-beam vidicon has an ASOS sensor area A of 50×50 mm; with $l/w = 5$ for standard resolving power test objects, the detail SNR for this camera is

$$\text{SNR}_{\Delta(f)} = I_s \left(\frac{t m_b \tau_m}{I} \right)^{1/2} 1770 r\bar{\Delta} \left(\frac{1}{f} \right), \quad [2.9]$$

where I_s and I are expressed in nA, f in cycles/mm, m_b is the maximum beam modulation factor and $r\bar{\Delta}$ is the equivalent square-wave response factor of the camera including the lens.

2-4 Resolving-Power Functions of Return-Beam Vidicon Cameras

The threshold function most suitable for these solutions is the product $P = (I_s/I^{1/2})$ expressed as a function of f_r . It is obtained by substi-

tuting the threshold value $SNR_{\Delta(f)} = K = 3.6$ into Eq. [2.9],

$$P = I_g/I^{1/2} = f_r/[492 (tm_b\tau_m)^{1/2}r\Delta] \quad [2.10]$$

The square-wave response functions (MTF_{Δ}) of the perfect F/5.6 lens and three different RBV cameras (with this lens) are shown in the upper part of Fig. 8. The MTF of a perfect diffraction-limited F/5.6 lens is representative of the performance of the best high-aperture lenses covering a 50×50 mm format at the present state of the art and is used for comparison of high-definition cameras in this paper. Corresponding threshold functions calculated with Eq. [2.10] and typical constants are plotted in the lower part of this figure. The functions for $r\bar{\Delta} = 1$ permit assessment of the MTF effect on resolving power. The $MTF_{\Delta 1}$ represents an ultra-high-resolution camera using

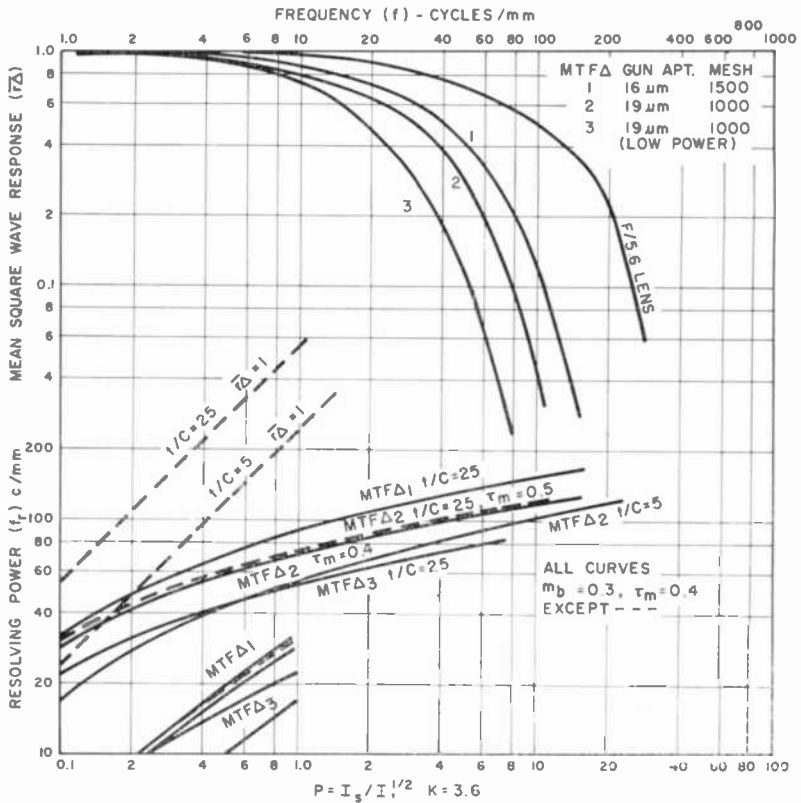


Fig. 8—Equivalent square-wave response functions $\bar{r}\Delta(f)$ (top curves), and threshold functions $P(f_r)$ for slow-scan readout of return-beam vidicon cameras with perfect F/5.6 lens (bottom curves).

a finer field mesh and smaller gun aperture (used in a 2-inch RBV) than MTF_{Δ_2} which represents a "standard" 4½-inch RBV. MTF_{Δ_3} is a "low power" value obtained when this tube is operated with a drift space potential reduced from the normal value of 600 volts to 160 volts, which results in a 3.7 to 1 reduction of the focusing and deflection power. Exposures and gray-scale values can now be determined from the transfer functions of the camera.

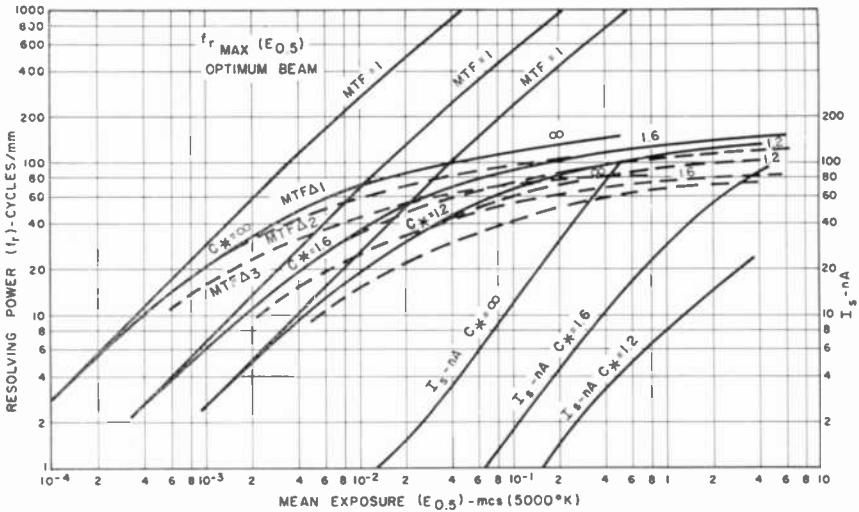


Fig. 9—Maximum resolving power (f_r) and signal currents (I_s) of 4½-inch return-beam vidicon cameras with perfect F/5.6 lens for a 10 second slow-scan readout as a function of a mean exposure ($E_{0.5}$) and contrast (C_*).

2.4(a) The maximum resolving power as a function of exposure, $f_r(E_{0.5})$

The beam current is optimized for each highlight exposure to accommodate a full modulation of the gray scale. Select a maximum current I_s and ratio $I_s/I^{1/2}$. Find the resolving power f_r for the camera MTF in Fig. 8. The current ratio determines the values I_s and V_s on the readout transfer function in Fig. 7. The exposure required for V_s is obtained from Fig. 6 and the mean exposure is computed by

$$E_{0.5} = 0.5\hat{E}(1 + 1/C_*) \quad [2.11]$$

The resolving powers for several MTF's of the camera can be tabulated simultaneously from the threshold functions (Fig. 8) for

each current ratio and exposures for three contrasts are obtained from Fig. 6 as illustrated by Table 1. Graphs of these functions are shown in Fig. 9. The curves $MTF = 1$ are quantum-limit curves computed for unity MTF. It should be noted that the signal currents $I_s(E_{0.5})$ decrease to very small values at low exposures where a "clean" image requires excellent uniformity of the sensor. Amplifier noise is not a problem because of the electron multiplier.

2.4(b) Resolving Power versus Gray Scale in a Single Image, $f_r(S)$

Select a mean exposure level $E_{0.5}$ and contrast C , and compute E_{max} with Eq. [2.11]. Determine V_{sm} from Fig. 6 and the corresponding currents I_s and I from Fig. 7. With I as a constant (fixed beam current) tabulate a set of decreasing values $I_s/I^{1/2}$ and find f_r from Fig. 8 as illustrated by Table 2 (columns 1 to 5). Determine the potential V_s corresponding to I_s from Fig. 7 and the exposure E_{max} for the contrast C , from Fig. 6. The corresponding gray-scale value is given by $S = 0.5 E_{max,s}/E_{max,0.5}$. This part of the calculation furnishes the resolving powers for $S < 0.5$ and can be used for all contrasts because the "haze" is clipped out in the readout process.

The resolving power for $S > 0.5$ is computed by different methods, depending on the linearity of the sensor transfer function $V(E)$. This function is nonlinear for large signals and high contrasts. In this case the signal current is calculated from the transferred difference $I_{smax} - I_{smin}$. The calculation for $C = \infty$ is illustrated by Table 2. Assume a set of values $S > 0.5$ and determine the ratio $E_{smin}/\Delta E_{max} = 2S - 1$ (see Fig. 1). Calculate the exposure $E_{min} = E_{max}/C$. The exposure for the selected gray-scale level is then given by

$$E_{min,s} = E_{min} + (2S - 1)(E_{max} - E_{min}). \quad [2.12]$$

Next determine the signal potential V_{min} from the primary transfer curve $C = \infty$ in Fig. 6, and from V_{min} determine I_{smin} with Fig. 7. The signal current I_s is the difference $(I_{smax} - I_{smin})$ where I_{smax} is the maximum highlight current ($I_{smax} = 75.25$ nA for the example). From I_s calculate the ratio $I_s/I^{1/2}$ for which Fig. 8 yields the resolving power.

The sensor transfer function is substantially linear for low-contrast signals. Potential increments are directly proportional to exposure increments and the potential difference ΔV_s can be computed with

$$\Delta V_s = 2(1 - S)V_{smax}. \quad [2.13]$$

V_{smax} is the maximum signal listed for the contrasts $C = 1.6$ and 1.2

Table 1—Resolving-Power Functions f_r ($E_{0.5}$) for 4½-inch Return-Beam Vidicons (F/5.6 Lens, $t/C = 25$, $t = 10$, $\tau_m = 0.4$ for MTF_{Δ_1} and 0.5 for MTF_{Δ_2} and MTF_{Δ_3})

| $I_S/I^{1/2}$ | f_r (cycles/mm) | | I_S (nA) | V_S (volts) | $C_s = \infty$ | | $C_s = 1.6$ | | $C_s = 1.2$ | |
|---------------|----------------------|------------------|---------------|------------------|--------------------|--------------------|--------------------|--------------------|--------------------|--------------------|
| | MTF_{Δ_1} | MTF_{Δ_2} | | | E_{max} (mcs) | $E_{0.5}$ (mcs) | E_{max} (mcs) | $E_{0.5}$ (mcs) | E_{max} (mcs) | $E_{0.5}$ (mcs) |
| 10 | 150 | 120 | 98.25 | 2.8 | 1.0 | 0.5 | 7.0 | 5.7 | — | — |
| 7.0 | 140 | 112 | 50. | 1.7 | 0.58 | 0.29 | 2.15 | 1.745 | — | — |
| 4.75 | 130 | 100 | 24. | 1.0 | — | — | — | — | 4.25 | 3.9 |
| 3.25 | 120 | 98 | 12. | 0.62 | 0.205 | 0.104 | 0.6 | 0.487 | 1.6 | 1.465 |
| 1.58 | 100 | 82 | 3.5 | 0.245 | 0.08 | 0.04 | 0.218 | 0.1765 | 0.48 | 0.44 |
| 0.7 | 80 | 67 | 1.11 | 0.09 | 0.03 | 0.015 | 0.08 | 0.065 | 0.17 | 0.156 |
| 0.325 | 60 | 52 | 0.49 | 0.039 | 0.0126 | 0.0063 | 0.035 | 0.0284 | 0.076 | 0.07 |
| 0.145 | 40 | 37.5 | 0.205 | 0.0165 | 0.0054 | 0.0027 | 1.0145 | 0.0118 | 0.0315 | 0.0288 |
| 0.096 | 31.5 | 30 | 0.134 | 0.0108 | 0.0036 | 0.0018 | 0.0095 | 0.00772 | 0.020 | 0.0183 |
| 0.054 | 20 | 20 | 0.076 | 0.0062 | 0.00205 | 0.00102 | 0.0055 | 0.00446 | 0.017 | 0.0107 |
| 0.0205 | 10 | 10 | 0.03 | 0.0024 | 0.00077 | 0.00038 | 0.00205 | 0.00166 | 0.0044 | 0.0040 |

From Fig. 8

From Fig. 6

E_{max} and E_{min} are given in mcs.

Table 2—Resolving-Power Functions $f_r(S)$ for Return-Beam Vidicons ($E_{o.s} = 0.4$ mcs and $t/C = 25$ sec/ μ F)

| I_s (nA) | $I_s/I^{1/2}$ | $f_r, MTF\Delta$ (cycles/mm) | V_s (volts) | E_{max} (mcs) | S | S | S | $(2S-1)$ | $E_{min,s}$ (mcs) | V_{min} (volts) | I_{smin} (nA) | I_s (nA) | $I_s/I^{1/2}$ | $f_r, MTF\Delta$ (cycles/mm) | |
|---|---------------|---------------------------------|------------------|--------------------|--------|------|-----|----------|----------------------|----------------------|--------------------|---------------|---------------|---------------------------------|----|
| | | 1 2 3 | | | | | | | | | | | | 1 2 3 | |
| $C_o = \infty, V_{o.s} = 2.28, I = 77$ nA, $I_s = 75.25$ nA | | | | | | | | | | | | | | | |
| 75.25 | 8.58 | 148 | 2.28 | 0.8 | 0.5 | 0.7 | 0.4 | 0.32 | 0.96 | 22.5 | 52.75 | 6.0 | 136 | 110 | 79 |
| 50 | 5.7 | 135 | 1.68 | 0.58 | 0.363 | 0.8 | 0.6 | 0.48 | 1.4 | 39. | 36.25 | 4.12 | 126 | 102 | 72 |
| 30 | 3.42 | 120 | 0.98 | 0.39 | 0.244 | 0.9 | 0.8 | 0.64 | 1.85 | 57. | 18.25 | 2.08 | 108 | 88 | 64 |
| 10 | 1.14 | 92 | 0.545 | 0.18 | 0.1125 | 0.95 | 0.9 | 0.72 | 2.06 | 65. | 10.25 | 1.165 | 92 | 76 | 56 |
| 7.525 | 0.858 | 85 | 0.44 | 0.145 | 0.0905 | | | | | | | | | | |
| 5 | 0.57 | 74 | 0.322 | 0.105 | 0.0655 | | | | | | | | | | |
| 3 | 0.342 | 61 | 0.215 | 0.070 | 0.0438 | | | | | | | | | | |
| 1 | 0.114 | 35 | 0.082 | 0.027 | 0.0169 | | | | | | | | | | |
| 0.5 | 0.057 | 22 | 0.041 | 0.0135 | 0.0085 | | | | | | | | | | |
| $C_o = 1.6, V_{o.s} = 0.52, I_s = 9.4$ nA, $I = 11.5$ nA | | | | | | | | | | | | | | | |
| 9.4 | 2.77 | 115 | 0.52 | 0.493 | 0.5 | 0.7 | 0.6 | 0.312 | 0.208 | 2.9 | 6.5 | 1.91 | 105 | 86 | 64 |
| 5.0 | 1.47 | 99 | 0.32 | 0.288 | 0.292 | 0.8 | 0.4 | 0.208 | 0.312 | 4.8 | 4.6 | 1.35 | 79 | 79 | 59 |
| 2.0 | 0.588 | 75 | 0.152 | 0.134 | 0.136 | 0.9 | 0.2 | 0.104 | 0.416 | 7.0 | 2.4 | 0.705 | 80 | 66 | 50 |
| 1.0 | 0.294 | 56 | 0.082 | 0.072 | 0.073 | | | | | | | | | | |
| 0.5 | 0.147 | 40.5 | 0.040 | 0.0355 | 0.036 | | | | | | | | | | |
| 0.2 | 0.059 | 22.5 | 0.016 | 0.014 | 0.0142 | | | | | | | | | | |
| 0.1 | 0.03 | 13.2 | 0.082 | 0.007 | 0.0071 | | | | | | | | | | |
| $C_o = 1.2, V_{o.s} = 0.225, I_s = 3.25$ nA, $I = 5.0$ nA | | | | | | | | | | | | | | | |
| 3.25 | 1.45 | 99 | 0.225 | 0.437 | 0.5 | 0.7 | 0.6 | 0.135 | 0.090 | 1.12 | 2.13 | 0.95 | 88 | 72 | 54 |
| 2.0 | 0.894 | 8.6 | 0.15 | 0.288 | 0.329 | 0.8 | 0.4 | 0.090 | 0.135 | 1.72 | 1.53 | 0.682 | 79 | 66 | 50 |
| 1. | 0.446 | 67 | 0.082 | 0.153 | 0.175 | 0.9 | 0.2 | 0.045 | 0.180 | 2.48 | 0.77 | 0.344 | 61 | 53 | 39 |
| 0.7 | 0.313 | 58 | 0.057 | 0.108 | 0.133 | | | | | | | | | | |
| 0.35 | 0.157 | 42 | 0.028 | 0.054 | 0.0616 | | | | | | | | | | |
| 0.1 | 0.0446 | 18 | 0.0083 | 0.0157 | 0.018 | | | | | | | | | | |
| 0.07 | 0.0313 | 13.7 | 0.0057 | 0.0108 | 0.0123 | | | | | | | | | | |
| 0.05 | 0.0223 | 10.2 | 0.004 | 0.0076 | 0.0087 | | | | | | | | | | |

in Table 2. The signal V_{\min} is now simply $V_{\min} = V_{S_{\max}} - \Delta V_S$, and succeeding columns in Table 2 list the values $I_{S_{\min}}$, the signal current $I_S = I_{S_{\max}} - I_{S_{\min}}$, and the ratio $I_S/I^{1/2}$ by which f_r is determined with Eq. [2.10] or Fig. 8.

The resolving-power functions $f_r(S)$ for the three MTF Δ 's of the 4½-inch RBV camera (F/5.6 lens) listed in Table 2 are plotted in Fig. 10. The mean resolving power (MRP3) has been computed with Eq. [1.3].

The exposure $E_{0.5} = 0.4$ mcs was selected for comparison with an aerial film camera containing type 3414 high-definition film. The RBV camera can operate with higher or lower exposures. The peak resolving power at $S = 0.5$ can be taken from Fig. 9. The $f_r(S)$ functions become flatter for higher exposures and f_r decreases faster for $S < 0.5$ at lower exposures. Single-bar resolving power functions are evaluated in Section 4.

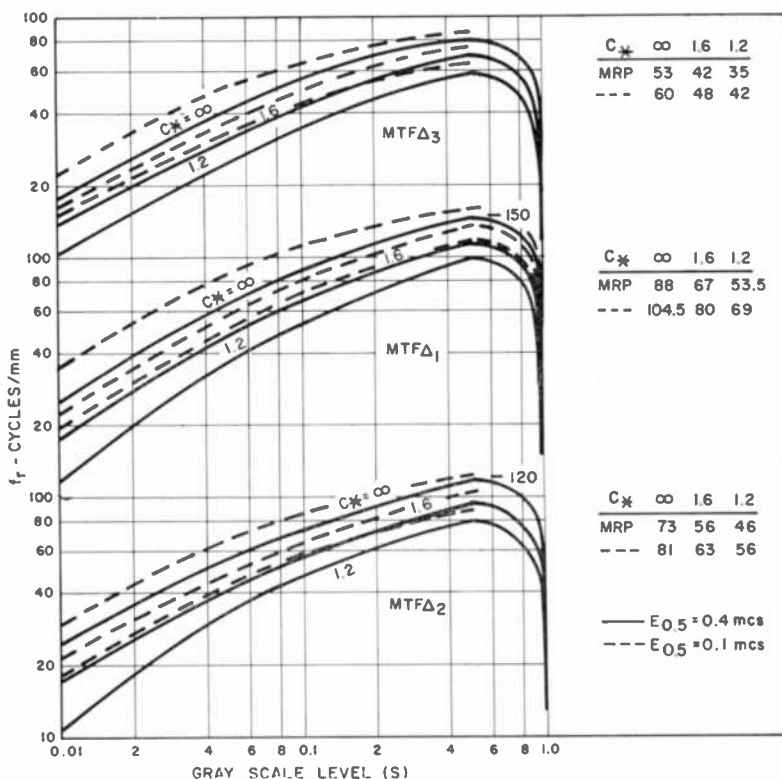


Fig. 10—Resolving power versus gray-scale level ($f_r(S)$) for three MTF Δ 's of 4½-inch return-beam vidicon cameras, two exposures, and three contrast ratios with perfect F/5.6 lens.

3. Photographic Cameras

A good approximation of the detail signal-to-noise ratio for three-bar test objects is given by¹

$$SNR_{\Delta(f)} = SNR_{o(f)} (l/w)^{1/2} \gamma 2m_{o,s} \bar{\Delta}_f \quad [3.1]$$

where

$$SNR_{o(f)} = \frac{4.88 \times 10^3}{D^{1/2} G f} \quad [3.2]$$

is the large-area signal-to-noise ratio for a selected frequency band (f).

The film granularity $G = 1000\sigma_D$ is measured with a $48\text{-}\mu\text{m}$ aperture at the net density $D = 1$. The exponent of D is 0.5 for high-resolution films that have a single grain size and approximately 0.45 for films

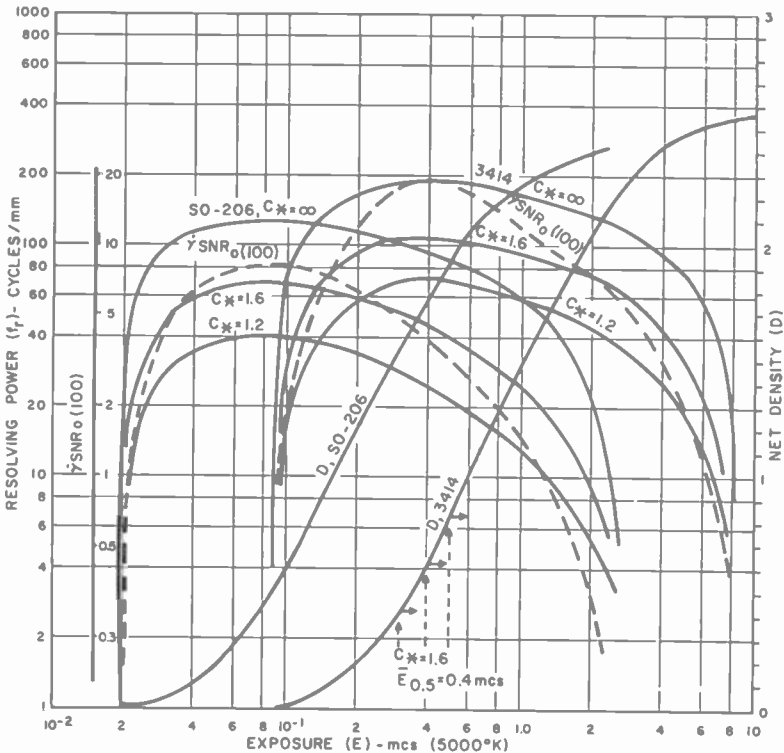


Fig. 11—Density (D), reference signal-to-noise ratio ($\gamma SNR_{o(100)}$) and maximum resolving power (f_r) of photographic cameras with perfect F/5.6 lens and high definition films as functions of exposure.

with composite grain sizes such as TRI-X, double X and Pantomic-X film.*

It is convenient to compute the reference product $\gamma \text{SNR}_{o(100)}$ for $f = 100 \text{ c/mm}$ shown by broken-line curves as a function of E in Figs. 11 and 12. The signal-to-noise ratio $\text{SNR}_{o(f)}$ is then expressed by $\text{SNR}_{o(f)} = \text{SNR}_{o(100)}(100/f)$, which is substituted with the threshold constant $\text{SNR}_{\Delta(f)} = K = 3.6$ into Eq. [3.1] to yield

$$m_{o,s} \gamma \text{SNR}_{o(100)} = \frac{0.806 f_r}{100 r \bar{\Delta}_f} \quad [3.3]$$

The right side of this equation is the threshold function

$$P = \frac{0.806 f_r}{100 r \bar{\Delta}_f} \quad [3.4]$$

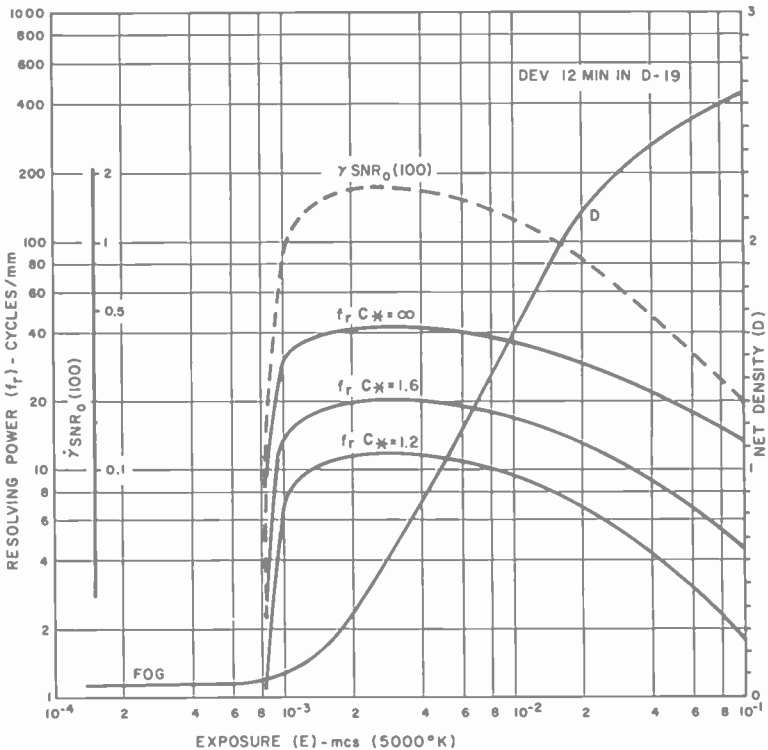


Fig. 12—Density (D), reference signal-to-noise ratio ($\gamma \text{SNR}_{o(100)}$) and maximum resolving power (f_r) of photographic camera with F/5.6 lens and TRI-X film.

* Trade name of the Eastman Kodak Co., Rochester, N.Y.

plotted in Fig. 13 for several lens-film combinations. The product

$$P_s = m_{o,s} \gamma \text{SNR}_{o(100)} \quad [3.5]$$

on the left side of Eq. [3.3] is a function of exposure and contrast.

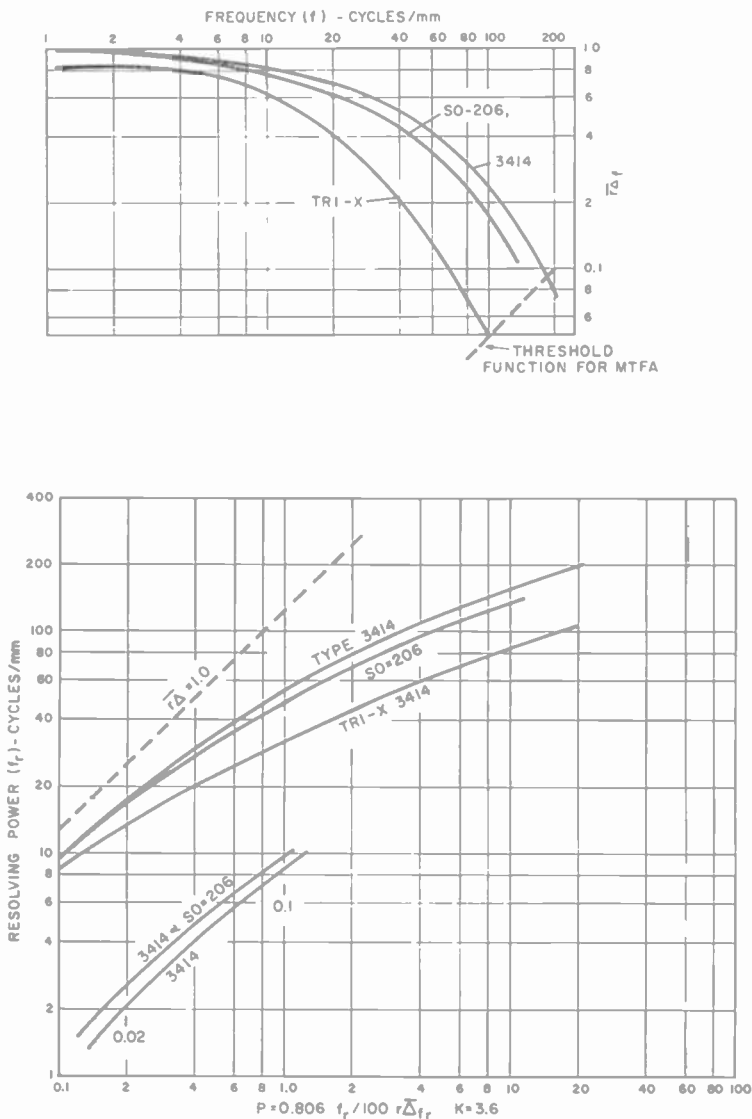


Fig. 13—(a) Square-wave response ($r\Delta_r$) and (b) threshold functions of photographic cameras with perfect F/5.6 lens.

3.1 The Resolving-Power Functions $f_r(E_{0.5})$; $S = 0.5, m_{0,S} = m_0$

The product P_B (Eq. 3.5) is computed as a function of exposure $E_{0.5}$ of the film type for the selected contrast $m_0 = (C_* - 1)/(C_* + 1)$. Since $P_B = P$, the resolving power of the camera can be found directly from the graph in Fig. 13 to plot the functions $f_r(E_{0.5})$ shown in Figs. 11 and 12.

3.2 The Resolving-Power $f_r(S)$ for a Single Image ($m_{0,S} = m_0 \rho_m$)

The modulation ratio ρ_m for the factor $m_{0,S}$ is a function of S given by Eq. [1.1] or Fig. 4. Table 3 illustrates the progressive steps to calculate the resolving power $f_r(S)$ for 3414 film at the optimum* exposure $E_{0.5} = 0.4$ mcs.

The functions from Table 3 are plotted in Fig. 14. The gray scale

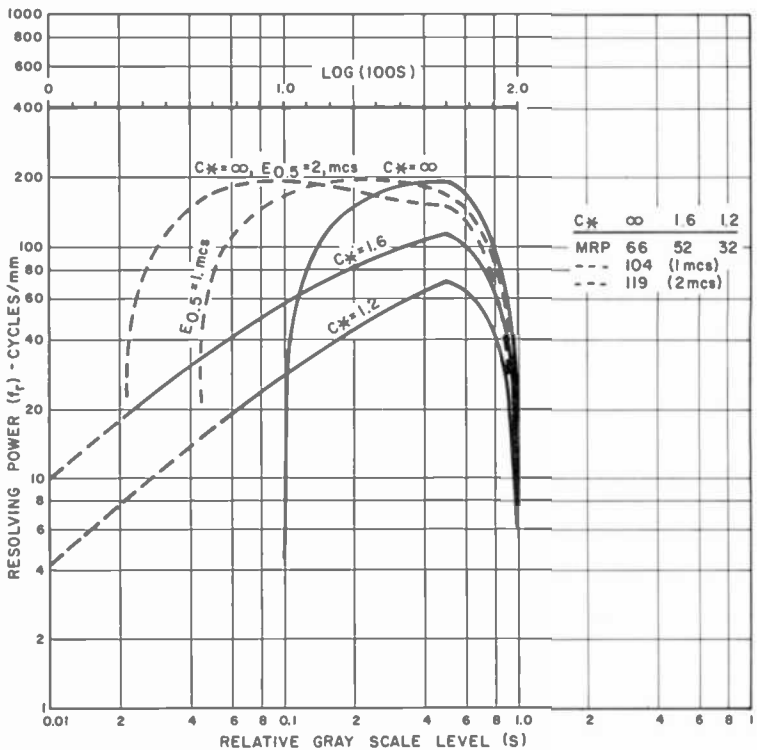


Fig. 14—Resolving power versus gray-scale level of 3414 film camera with perfect F/5.6 lens, mean exposure $E_{0.5} = 0.4$ mcs (solid lines).

* For medium and low contrasts

Table 3—Resolving-Power Calculation $f_r(S)$ for Type 3414 Film Camera With Perfect F/5.6 Lens

| $C_s = \infty$ | | | | | | $C_s = 1.2$ | | | | | |
|----------------|-------|-----------------------|------------|-------|-------|-------------|-------|-----------------------|------------|-------|-------|
| S | E_S | $\gamma SNR_{e(cms)}$ | m_{eP_m} | P_S | f_r | S | E_S | $\gamma SNR_{e(cms)}$ | m_{eP_m} | P_S | f_r |
| 0.5 | 0.4 | 19.0 | 1.0 | 19.0 | 198 | 0.6 | 0.48 | 19 | 0.66 | 11.8 | 168 |
| 0.4 | 0.32 | 18.0 | 1.0 | 18.0 | 192 | 0.8 | 0.64 | 16 | 0.25 | 4 | 108 |
| 0.3 | 0.24 | 15.5 | 1.0 | 15.5 | 182 | 0.9 | 0.72 | 14.8 | 0.115 | 1.7 | 72 |
| 0.2 | 0.16 | 8.6 | 1.0 | 8.6 | 148 | | | | | | |
| 0.125 | 0.10 | 2.0 | 1.0 | 2.0 | 78 | | | | | | |
| 0.11 | 0.088 | 0 | 1.0 | 0 | 0 | | | | | | |

Eqn (1.1) Fig 11
or
Eqn (1.2) Fig 11

| $C_s = 1.6$ | | | | | | $C_s = 1.2$ | | | | | |
|-------------|-------|-----------------------|------------|-------|-------|-------------|-------|-----------------------|------------|-------|-------|
| S | E_S | $\gamma SNR_{e(cms)}$ | m_{eP_m} | P_S | f_r | S | E_S | $\gamma SNR_{e(cms)}$ | m_{eP_m} | P_S | f_r |
| 0.5 | 0.4 | 19 | 0.231 | 4.4 | 111 | 0.4 | 19.0 | 0.091 | 0.074 | 1.72 | 72 |
| 0.4 | 0.362 | 19 | 2.207 | 3.95 | 108 | | | 0.0565 | 1.07 | 66 | 66 |
| 0.3 | 0.362 | 19 | 0.152 | 2.9 | 93 | | | 0.0382 | 0.725 | 56 | 56 |
| 0.2 | 0.345 | 18.8 | 0.105 | 2.02 | 79 | | | 0.0195 | 0.37 | 44 | 44 |
| 0.1 | 0.326 | 18.5 | 0.0565 | 1.05 | 56 | | | 0.0095 | 0.18 | 15.7 | 15.7 |
| 0.05 | 0.316 | 18.1 | 0.0295 | 0.535 | 36 | | | 0.0038 | 0.072 | 7.5 | 7.5 |
| 0.02 | 0.311 | 18 | 0.0117 | 0.21 | 17.8 | | | 0.0019 | 0.036 | 4.2 | 4.2 |
| 0.01 | | 18 | 0.0059 | 0.106 | 10 | | | 0.073 | 1.39 | 65 | 65 |
| 0.6 | 0.427 | 19 | 0.17 | 3.24 | 98 | | | 0.0365 | 0.69 | 46 | 46 |
| 0.8 | 0.455 | 18.7 | 0.081 | 1.52 | 68 | | | 0.0155 | 0.295 | 23 | 23 |
| 0.9 | 0.474 | 18.2 | 0.032 | 0.58 | 38.5 | | | | | | |

| $C_s = 1.2$ | | | | | |
|-------------|------|--------|-------|-----|------|
| S | a | aP_S | f_r | S | a |
| 0.5 | 1.0 | 4.4 | 111 | 0.5 | 1.0 |
| | 0.4 | 1.76 | 79 | | 0.4 |
| | 0.1 | 0.44 | 35 | | 0.1 |
| | 0.04 | 0.176 | 17.5 | | 0.04 |
| | 0.01 | 0.044 | 5 | | 0.01 |

is cut off at $S = 0.1$ in the high-contrast image ($C. = \infty$) because of the exposure threshold of the film (see Fig. 11). This cutoff is a general characteristic of all films. The film threshold is of no importance for lower contrasts (in this case $C. < 9.0$) and can be eliminated by reducing higher contrasts to this value by a pre-exposure. Higher exposures increase the range for $C. = \infty$ but give poorer performance for $C. < 9$.

The contrast $C. = \infty$ or $C. = 1000$ used for resolving-power ratings is a laboratory condition that does not occur in aerial images because of lens flare and haze. The arrows in Fig. 11 indicate that the exposure $E_{0.5} = 0.4$ mcs is optimum for this film type because it is centered on the peak of the $\gamma\text{SNR}/\sigma_{(100)}$ curve. Exposure and development of the film must be closely controlled and restoration of a normal print contrast requires expansion of the short "video" density range ΔD by a high-gamma printing process.

The small density range introduces a limitation caused by random density variations in film manufacture. These variations (ΔD) are in the order of 0.01 for most films, which make questionable the usefulness of density differences $\Delta D < 0.01$ corresponding to S -scale values indicated by broken lines in Fig. 14.

The gray-scale functions $f_r(S)$ for type SO-206 and TRI-X type 2403 film are shown in Fig. 15.

A reduction of input modulation below the maximum amplitude $a = 1$ causes f_r to decrease along the curve $f_r(S)$. The exact values are slightly lower because P_s decreases linearly with a reduction of modulation when the noise is constant. The error is small as seen from the numerical values for $C. = 1.6$ and 1.2 in Table 3.

4. Single-Line Resolving-Power $f_{r,w}(S)$

The number of bars in a standard resolving-power test object is reduced to a single bar. The square-wave response ($r\bar{\Delta}$) of the system to the bar frequency in Eqs. [2.8] and [3.1] must be replaced by the total equivalent pass band; i.e., the bandwidth factor* $(f_e/f_r)^{1/2}$ and the threshold constant K is increased to 6, which results in the following threshold function for 4½-inch return-beam vidicons:

$$I_s/I^{1/2} = f_{r,w}/295(tm_b\tau_m)^{1/2}(f_e/f_{r,w})^{1/2}. \quad [4.1]$$

Graphs of the bandwidth factors and threshold functions are shown in

* f_e is computed from the sine-wave MTF of the camera as defined for Eq. [1.5].

Fig. 16. The calculation of the exposure and gray-scale level required by the threshold product is illustrated in Table 4 for the RBV camera and for a mean exposure $E_{0.5} = 0.4$ mcs. Most of the data can be copied from Table 2, because the relation of currents, signal potentials, and peak exposures are identical for a given mean exposure ($E_{0.5}$). The gray-scale values, however, are now

$$S = \hat{E} / \hat{E}_{\max} \tag{4.2}$$

The threshold function for film is similarly

$$P_w = \frac{1.34 f_{r,w}}{100 (f_e / f_{r,w})^{1/2}} \tag{4.3}$$

obtained from $m_{o,s} \dot{\gamma} SNR_{o(100)} = \frac{1.34 f_{r,w}}{100 (f_e / f_{r,w})^{1/2}}$.

The left side (P_B) must be computed for the mean pulse level \bar{E}

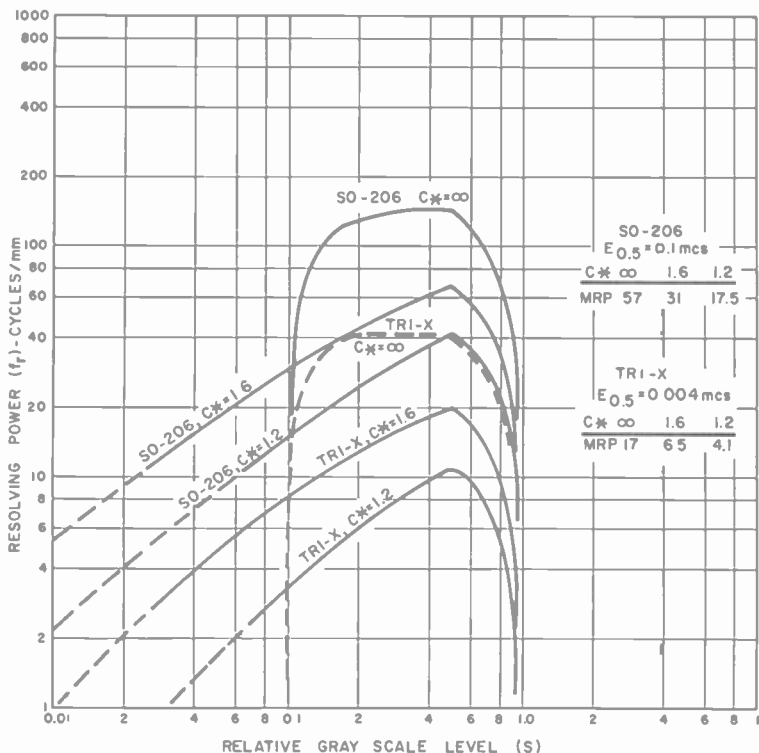


Fig. 15—Resolving power functions $f_r(s)$ for SO-206 and TRI-X film cameras with perfect F/5.6 lens.

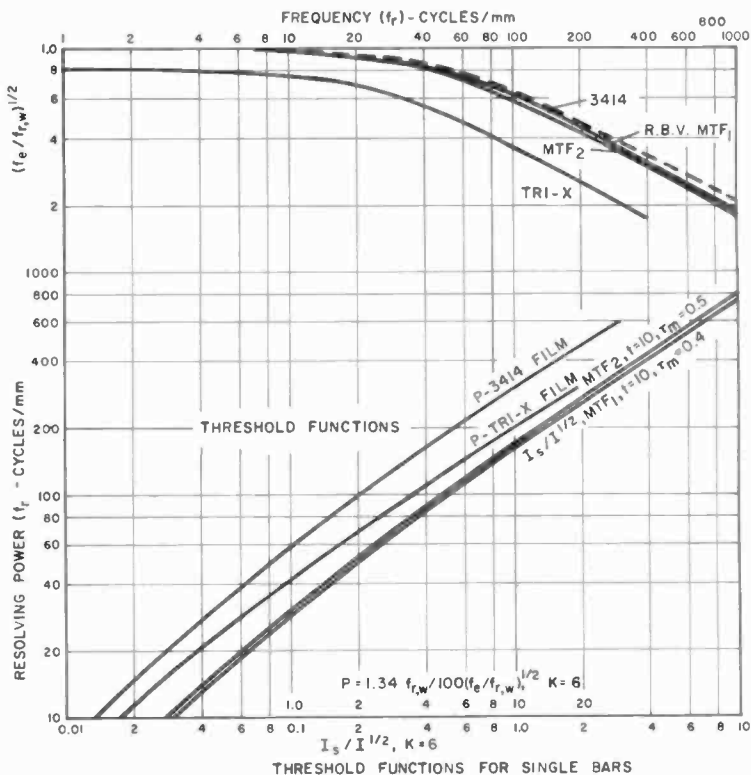


Fig. 16—Bandwidth factors $(f_e/f_r)^{1/2}$ and threshold functions for the evaluation of single-bar resolving powers of high-definition television and film cameras with perfect F/5.6 lens.

Table 4—Single-Bar Resolving Power $f_{r,w}$ (S) for 4½-Inch Return-Beam Vidicons with F/5.6 Lens ($E_{0.5} = 0.4$ mcs, $t/C = 25$ sec/ μ F, $t = 10$ sec)

| I_s (nA) | $I_s/I^{1/2}$ | $f_{r,w}$ MTF Δ_1 | MTF Δ_2 | V_s (volts) | \hat{E} (mcs) | S |
|---------------------------|---------------|-----------------------------|----------------|------------------|--------------------|--------|
| $C_o = \infty, I = 77$ nA | | | | | | |
| 75.25 | 8.58 | 680 | 720 | 2.18 | 0.8 | 1.0 |
| 50.0 | 5.7 | 510 | 540 | 1.68 | 0.58 | 0.725 |
| 30.0 | 3.42 | 365 | 380 | 1.18 | 0.39 | 0.487 |
| 10.0 | 1.14 | 178 | 182 | 0.545 | 0.18 | 0.225 |
| 7.525 | 0.858 | 146 | 150 | 0.44 | 0.145 | 0.181 |
| 5.0 | 0.57 | 110 | 115 | 0.32 | 0.105 | 0.131 |
| 3.0 | 0.342 | 76 | 79 | 0.22 | 0.07 | 0.0875 |
| 1.0 | 0.114 | 32 | 38 | 0.082 | 0.027 | 0.0338 |
| 0.5 | 0.057 | 18 | 19 | 0.041 | 0.0135 | 0.017 |

(continued next page)

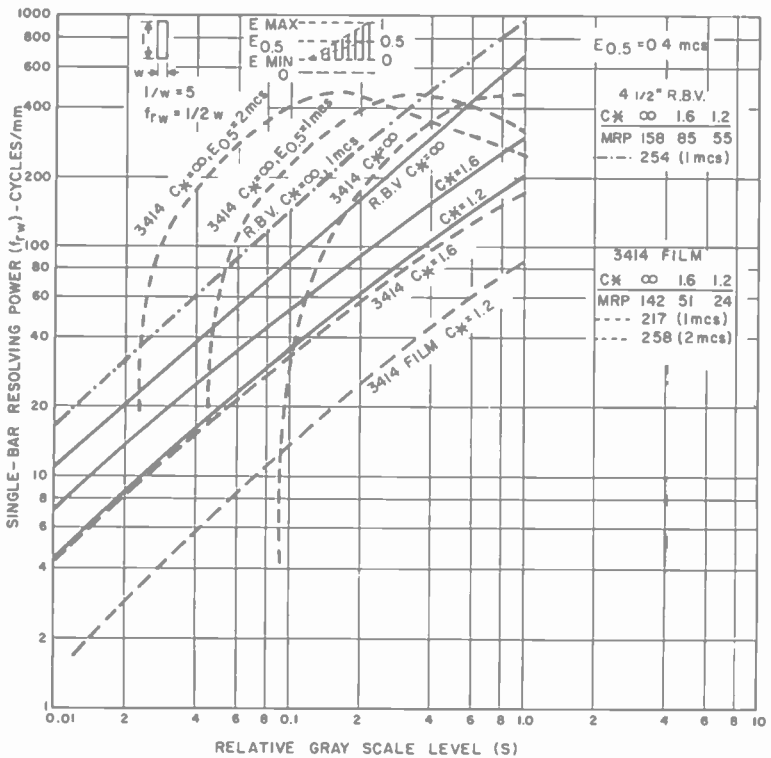
Table 4 (Continued)

 $C_s = 1.6, I = 11.5$ nA

| | | | | | | |
|-----|-------|------|------|-------|--------|--------|
| 9.4 | 2.77 | 320 | 330 | 0.52 | 0.493 | 1.0 |
| 5.0 | 1.47 | 208 | 213 | 0.32 | 0.288 | 0.585 |
| 2.0 | 0.588 | 111 | 118 | 0.152 | 0.134 | 0.272 |
| 1.0 | 0.294 | 68 | 71 | 0.082 | 0.072 | 0.142 |
| 0.5 | 0.147 | 40 | 42 | 0.04 | 0.0355 | 0.072 |
| 0.2 | 0.059 | 18.2 | 19.5 | 0.016 | 0.014 | 0.0284 |
| 0.1 | 0.03 | 10.0 | 10.8 | 0.082 | 0.007 | 0.0142 |

 $C_s = 1.2, I = 50$ nA

| | | | | | | |
|------|-------|------|------|--------|-------|-------|
| 3.25 | 1.45 | 208 | 212 | 0.225 | 0.437 | 1.0 |
| 2.0 | 0.90 | 150 | 155 | 0.15 | 0.288 | 0.66 |
| 1.0 | 0.446 | 92 | 96 | 0.082 | 0.153 | 0.35 |
| 0.7 | 0.313 | 72 | 75 | 0.057 | 0.108 | 0.247 |
| 0.35 | 0.157 | 42 | 44 | 0.028 | 0.054 | 0.123 |
| 0.1 | 0.045 | 14.4 | 15.2 | 0.0083 | 0.016 | 0.037 |
| 0.07 | 0.031 | 10.1 | 11.0 | 0.0057 | 0.011 | 0.025 |

Fig. 17—Single-bar resolving-power functions $f_{r,w}(S)$ for high-definition television and film cameras.

$= (\hat{E} + E_o)/2$ for $C_s = \infty$ because of the film threshold E_o . For lower contrasts the value is given by Eq. [1.6]. The product $\dot{\gamma} \text{SNR}_{o(100)}$ is taken from Fig. 11 for the level \bar{E} as listed in Table 5, and multiplication by $m_{o,s}$ from Eq. [1.7] yields the product P_S . The resolving power $f_{r,w}$ is obtained from Fig. 16 for the value $P = P_S$.

Plots of the resolving-power functions $f_{r,w}(S)$ are shown in Fig. 17.

Table 5—Single-Bar Resolving Power $f_{r,w}(S)$ for 3414 Film with F/5.6 Lens ($E_{0.5} = 0.4$ mcs)

| $C_s = \infty, m_{o,s} = 1$ | | | | | |
|-----------------------------|---------------------------------|--|-------------------|--------------------------|-----------------------------------|
| S | \hat{E} (S-Level) (mcs) | \bar{E} $(\hat{E} + 0.09)/2$ (mcs) | P_S | $f_{r,w}$ (cycles/mm) | |
| 1.0 | 0.8 | 0.445 | 19 | 450 | |
| 0.8 | 0.64 | 0.365 | 19 | 450 | |
| 0.6 | 0.48 | 0.285 | 17.5 | 425 | |
| 0.5 | 0.40 | 0.255 | 16.2 | 410 | |
| 0.4 | 0.32 | 0.205 | 13 | 350 | |
| 0.3 | 0.24 | 0.165 | 9 | 275 | |
| 0.2 | 0.16 | 0.125 | 4.8 | 180 | |
| 0.1 | 0.088 | 0.089 | 1.0 | 58 | |
| $C_s = 1.6$ | | | | | |
| S | \bar{E}^* (mcs) | $\dot{\gamma} \text{SNR}_{o(100)}$ | $m_{o,s}^\dagger$ | P_S | $f_{r,w}^\ddagger$ (cycles/mm) |
| 1.0 | 0.4 | 19 | 0.231 | 4.4 | 170 |
| 0.8 | 0.382 | 19 | 0.207 | 3.95 | 158 |
| 0.6 | 0.362 | 19 | 0.152 | 2.9 | 128 |
| 0.4 | 0.345 | 18.8 | 0.105 | 2.02 | 98 |
| 0.2 | 0.326 | 18.5 | 0.056 | 1.05 | 60 |
| 0.1 | 0.316 | 18.1 | 0.03 | 0.535 | 35 |
| 0.04 | 0.311 | 18 | 0.012 | 0.21 | 15 |
| 0.02 | 0.31 | 18 | 0.006 | 0.106 | 8.2 |
| $C_s = 1.2$ | | | | | |
| S | \bar{E}^* (mcs) | $\dot{\gamma} \text{SNR}_{o(100)}$ | $m_{o,s}^\dagger$ | P_S | $f_{r,w}^\ddagger$ (cycles/mm) |
| 1.0 | 0.4 | 19 | 0.091 | 1.72 | 88 |
| 0.8 | 0.4 | 19 | 0.074 | 1.42 | 77 |
| 0.6 | 0.4 | 19 | 0.0565 | 1.07 | 60 |
| 0.4 | 0.4 | 19 | 0.0382 | 0.725 | 45 |
| 0.2 | 0.4 | 19 | 0.0195 | 0.37 | 25.5 |
| 0.1 | 0.4 | 19 | 0.0095 | 0.18 | 13.2 |
| 0.04 | 0.4 | 19 | 0.0038 | 0.072 | 5.6 |
| 0.02 | 0.4 | 19 | 0.0019 | 0.036 | 2.8 |

* From Eq. [1.6].

† From Eq. [1.7].

‡ From Fig. 16.

5. Evaluation of the MTFA

The MTFA⁵ is the area bounded by the threshold function $\bar{r}_{\text{thr}}(f)$ (required by the threshold value K) and the sine-wave MTF of the system (see Fig. 2). The square-wave MTF Δ is equally suitable for a comparison of systems and is used here for convenience. The threshold function for the "white" noise in return-beam vidicon and photographic cameras is a 45° line drawn through the previously computed resolving-power points in a log log plot of the square-wave MTF Δ of the system as illustrated by a partially drawn broken line in Fig. 13 for photographic film. A set of threshold lines for ten gray-scale levels in a single image (equal log spacings) is shown in Fig. 18 for the RBV camera (MTF Δ_1). The resolving powers are taken from Fig. 10.

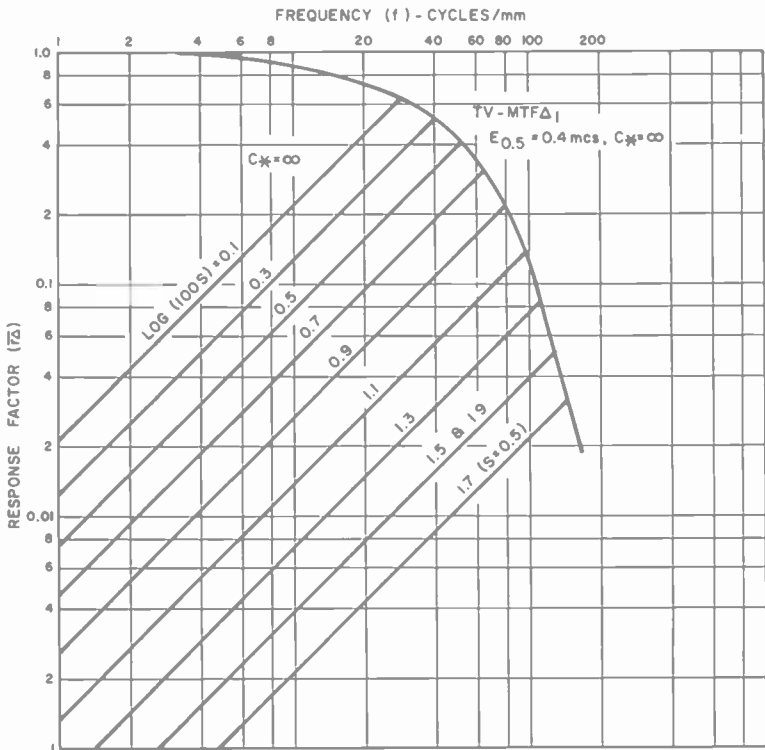


Fig. 18—Graph for evaluation of the square-wave MTF for the high-definition return-beam vidicon camera.

The MTF values for this camera and for a 3414 film camera are shown as a function of the gray-scale level in Fig. 19a, where they can be compared with the resolving-power functions $f_r(S)$ for the same cameras (Fig. 19b). It is evident that the relative MTF rating of the cameras is a strong function of the gray-scale level and very similar to resolving-power ratings.

MTFA's can obviously not be determined for single-line test objects.

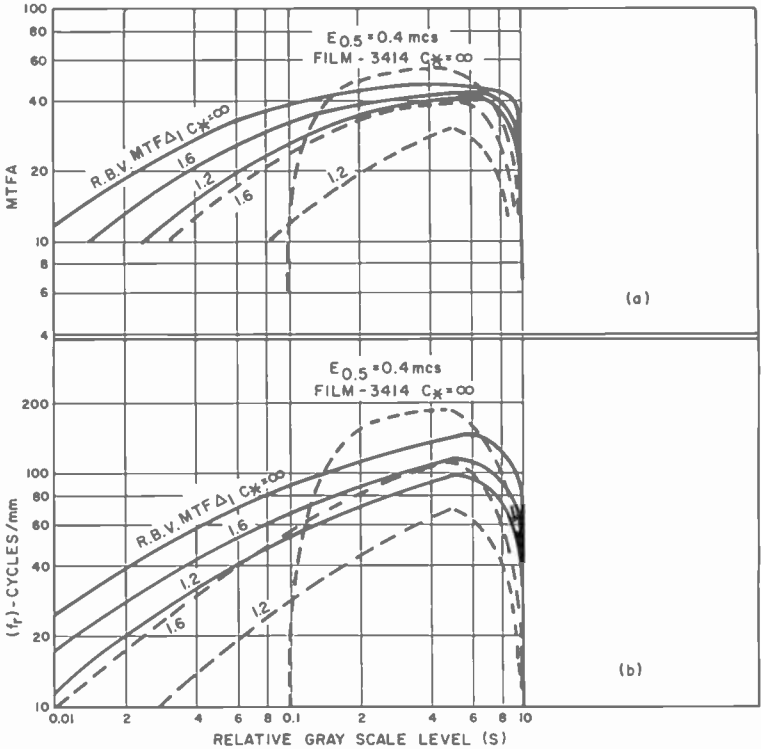


Fig. 19—(a) The square-wave modulation transfer area (MTFA) as a function of gray-scale level in a single image of a return-beam vidicon and film camera and (b) the resolving-power functions $f_r(S)$ for the same cameras.

6. Performance of High-Definition Television and Film Cameras

The general performance of two systems can be appraised by the relative position, values, and range of the maximum resolving-power functions $f_r(E_{0.5})$ shown in Fig. 20 for three contrast ratios. All cameras contain a "perfect" F/5.6 lens, which represents the MTF of the best high-aperture lenses covering a 50×50 format.

scale,* whereas its resolving power is substantially lower at low contrasts. The comparison for single-line resolving powers shown in Fig. 17 gives a similar result (even more favorable to the RBV camera) at low contrasts.

6.1 Figures of Merit

The various figures of merit computed for the two cameras are summarized in Table 6. The last three columns list the relative rating of the television camera versus film camera obtained from the ratio of the figures of merit. The comparison shows that a normal resolving-power rating based on a single value gives virtually the same rating as the MTF_A for all contrasts. The MRP₃ rating (three-bar test objects) for the complete gray scale reverses the rating for high contrast, because the gray-scale range of the film is shortened by the film threshold.

Table 6—Figures of Merit for High-Definition Television and Film Cameras with Perfect F/5.6 Lens at Mean Exposure $E_{0.5} = 0.4$ mcs

| Contrast Ratio C_o | 3414 Film Camera | | | RBV Camera, MTF ₁ | | | Ratio of Figures of Merit TV/Film | | |
|--|--------------------------|------|------|---------------------------------|-----|------|---|------|------|
| | ∞ | 1.6 | 1.2 | ∞ | 1.6 | 1.2 | ∞ | 1.6 | 1.2 |
| $f_{r(max)}$ | 190 | 112 | 70 | 150 | 115 | 100 | 0.79 | 1.03 | 1.43 |
| MTFA | 55 | 40 | 30 | 47 | 43 | 40 | 0.85 | 1.07 | 1.33 |
| MRP ₃ | 66 | 56 | 32 | 88 | 67 | 53.5 | 1.34 | 1.19 | 1.71 |
| | Single-line test objects | | | | | | | | |
| $f_{r,w(max)}$ | 450 | 150 | 75 | 540 | 265 | 174 | 1.2 | 1.77 | 2.32 |
| MRP ₁ | 142 | 51 | 23.5 | 158 | 85 | 55 | 1.11 | 1.67 | 2.35 |
| (MRP ₁ + MRP ₃)/2 | 104 | 53.5 | 27.7 | 123 | 76 | 54 | 1.18 | 1.42 | 1.95 |

The television camera is rated considerably higher at the low contrast $C_o = 1.2$. The relative ratings of the two cameras retain the same ordering for single-line test objects as given by the MRP₃ evaluation. The resolving power ($f_{r,w}$) is 20% higher for the television camera, and the MRP₁ rating is 11% higher for high-contrast scenes. The MRP₁ rating of the television camera exceeds the film camera rating by 67% at medium contrast ($C_o = 1.6$) and by 135% for a low contrast ratio of 1.2 to 1. The remarkably high resolving power of the television camera for single-line test objects is confirmed by ob-

* Higher exposures increase the performance for $C_o = \infty$ (see Fig. 14) but reduce the performance for contrasts $C_o < 9$.

servation of short single-line detail of known width in actual scenes made with a similar camera* at a distance of 5 miles. The MTF_A for periodic test objects becomes more significant when integrated for all gray-scale levels. The MTF_A(*S*) is shown in Fig. 19a. The integral is computed with

$$\int \text{MTFA}(S) = \int_0^2 \text{MTFA}(S) d \log (100S) \quad [6.1]$$

given in Table 7. The MTF_A integral gives the same ordering as the mean resolving power (MRP₃). The difference between the television and film camera is increased roughly 12% in favor of the television camera at all contrasts. It is evident that an MTF_A cannot be computed for aperiodic test objects.

Table 7— $\int \text{MTFA}(S)$ for High-Definition Television and Film Cameras with Perfect F/5.6 Lens at Mean Exposure $E_{0.5} = 0.4$ mcs

| Contrast ratio C_s | 3414 Film Camera | | | RBV Camera | | | Ratio TV/Film | | |
|-----------------------|------------------|-----|-----|------------|-----|-----|---------------|------|------|
| | ∞ | 1.6 | 1.2 | ∞ | 1.6 | 1.2 | ∞ | 1.6 | 1.2 |
| $\int \text{MTFA}(S)$ | 45 | 44 | 26 | 68 | 58 | 51 | 1.51 | 1.32 | 1.95 |

The mean resolving powers MRP₃ and MRP₁ for periodic and single-line test objects are a logical choice for a figure of merit because they give equal weight to the visibility of all detail within the logarithmic gray-scale range of the image, including all possible signal amplitudes as illustrated by the resolving power volumes Fig. 5a and 5b. A single figure of merit can be obtained by taking the mean value

$$\overline{\text{MRP}}_g = (\text{MRP}_1 + \text{MRP}_3)/2 \quad [6.2]$$

which assigns equal importance to the detection of periodic and aperiodic detail in the image. These ratings are given in the last row of Table 6.

The complete functions $f_r(S)$ and $f_{r,w}(S)$ are much more informative than a mean value because they permit a correct assessment of image detail at any gray-scale value.

* Tests at Wright Patterson Air Force Base.

6.2 Efficiency of High-Resolution Cameras

The efficiency of a camera can be appraised by comparing the exposure ($E_{0.5}$) with the exposure (\bar{E}_o) required by a "perfect" camera for a specified detail signal-to-noise ratio or resolving power. The efficiency for a given resolving power is the detection efficiency (η_f) defined by the exposure ratio

$$\eta_f = (\bar{E}_o/E_{0.5})_f \quad [6.3]$$

A perfect camera can be defined in several ways. The spectral sensitivity of real sensors is limited to a spectral pass band ($\Delta\lambda$) and generally peaks at a certain wavelength of radiation (λ_m). As a first choice one may consider a sensor having a constant quantum efficiency of unity. This "perfect" sensor has a spectral energy response proportional to λ^{-1} and peaks at the "blue" end of the pass band where the energy quantum has its largest value, whereas a constant energy response can have a quantum efficiency of unity only at the "red" end of the spectral pass band. Thus the choice of a "perfect" sensor depends on the application, and a definition useful for a comparison of cameras with different sensors requires selection of a bandwidth ($\Delta\lambda$) including the total spectral pass bands of both sensors.

This problem can be bypassed by retaining the spectral response of the individual cameras and increasing the efficiency ϵ_m at the peak-response of the sensors in both cameras to unity. The quantum-limited exposure \bar{E}_o so defined will be derived for the television camera and expressed in terms applicable to photographic cameras.

The exposure $E_{0.5}$ for the mean signal level in the perfect camera ($c = 1$, $\epsilon = 1$) is obtained by substitution of Eq. [2.2] and [2.11] into Eq. [2.1], yielding

$$E_{0.5} = \frac{1}{2m_o} 1.239 (c_{(1)} V_{sm}) 10^{-6} K_c \left(\frac{1}{\lambda_m} \right). \quad [6.4]$$

For unit efficiencies ($\tau_m = m_b = r\bar{\Delta} = 1$), $\text{SNR}_{\Delta(f)} = K = 3.6$, and a noise-free beam ($I_b'/I_{s0} = 0$) Eq. [2.6] can be solved for the product $(I_b/A)t$. This value multiplied by 10^{12} equals the product $C_{(1)}V_{sm}$ in Eq. [6.4], and substitution yields the exposure for the perfect camera,

$$\bar{E}_o = 5.1 (K_c/\lambda_m) 10^{-13} f_r^2 \left(\frac{1}{m_o^2} \right). \quad [6.5]$$

The absolute quantum limit $f_r(\bar{E}_o)$ is a $1/2$ -power curve. The constants for sunlight (5000°K) are $K_c/\lambda_m = 422/0.5$ for the ASOS sensor and $K_c/\lambda_m = 490/0.45$ for most photographic films. The absolute limits are very similar for both cameras as illustrated in Fig. 20.

6.3 Efficiency of Return-Beam Vidicon Cameras

The exposure required for a given resolving power can be expressed by the following equation

$$E_{0.5}(f_r) = \bar{E}_{o(f_r)} \left[\frac{c}{\epsilon} \frac{1}{\eta_c \tau_m} \frac{2m_o I}{I_s m_b} \left(\frac{1}{r\bar{\Delta}} \right)^2 \right] f_r, \quad [6.6]$$

where

c = dielectric trapping factor

ϵ = effective quantum efficiency of sensor

$\eta_c = I_s(t/C)/V_s =$ readout efficiency, I_s in μA , t/C in $\text{sec}/\mu\text{F}$.

The bracketed term is the reciprocal detection efficiency $1/\eta_f$. The beam noise term ($2m_o I/I_s m_b$) is derived as follows. The mean squared noise in the readout system is proportional to the current $I_{bn} = I_s(I/I_s m_b)$, whereas the noise source in a perfect camera is proportional to the mean current $I = I_s/2m_o$ from the exposure. The exposure factor is the ratio $I_{bn}/I = 2m_o(I/I_s m_b)$. Eq. [6.6] is solved progressively, starting with a resolving power f_r and associated value $r\bar{\Delta}$, to obtain the current ratio ($I_s/I^{1/2}$) with Eq. [2.10] or Fig. 8 and the values I_s and V_s from the readout transfer function Fig. 7. The exposure \bar{E}_o is given by Eq. [6.5]. The evaluation is illustrated by Table 8. The first four columns are taken from Table 1. The exposure factors in columns 5 through 8 can now be computed for the sensor (5), the readout system including the current loss on the field mesh (6), the increase required because of excess beam noise (7), and the MTF loss including the F/5.6 lens (8). The product $1/\eta_f$ multiplied by \bar{E}_o gives the exposure $E_{0.5}$ needed by the camera. It is apparent that the detection efficiency η_f is disappointingly small.

The major loss at high exposures is obviously the MTF loss ($1/r\bar{\Delta}^2$) in the camera. Beam noise and readout losses become dominating at low exposures when the signal potentials are very small. This relationship is also shown by the quantum limit curve $\text{MTF} = 1$ in Fig. 9 computed for $r\bar{\Delta} = 1$ (a curve for $r\bar{\Delta} = 1$ is given in Fig. 8). This

Table 8—Efficiency Analysis by Exposure Factors for 4½-inch RBV Camera (F/5.6 Lens, MTF_Δ, *m*₀ = 1, *t*/*C* = 25, *t* = 10)

| <i>f_r</i> | <i>I_s</i> | <i>V_s</i> | <i>r_Δ</i> | <i>c/ε</i> | $1/\eta_c\tau_m$ | Beam Noise | $1/r\bar{\Delta}^2$ | $1/\eta_l$ | \bar{E}_0 | <i>E_{0.5}</i> |
|----------------------|----------------------|----------------------|----------------------|------------|------------------|------------|---------------------|------------|-----------------------|------------------------|
| 150 | 98.25 | 2.8 | 0.03 | 2.68 | 2.85 | 6.8 | 1110 | 57300 | 8.05×10^{-6} | 4.66×10^{-1} |
| 120 | 12 | 0.62 | 0.071 | 2.42 | 5.17 | 7.65 | 198 | 19000 | 5.15×10^{-6} | 9.75×10^{-2} |
| 80 | 1.11 | 0.09 | 0.215 | " | 8.1 | 17.2 | 21.6 | 7280 | 2.28×10^{-6} | 1.65×10^{-2} |
| 40 | 0.205 | 0.0165 | 0.51 | " | 8.05 | 63.7 | 3.85 | 4770 | 5.74×10^{-7} | 2.73×10^{-3} |
| 20 | 0.076 | 0.0062 | 0.73 | " | 8.15 | 160 | 1.87 | 5900 | 1.43×10^{-7} | 8.44×10^{-4} |
| 10 | 0.03 | 0.0024 | 0.95 | " | 8.0 | 396 | 1.11 | 8500 | 3.58×10^{-8} | 3.04×10^{-4} |

function is calculated by assuming f_r and going through the same process. It cannot be obtained from Table 8 by simply leaving out the multiplier $1/r\bar{\Delta}^2$ because currents and potentials are entirely different for $r\bar{\Delta} = 1$.

Lower contrasts displace the absolute quantum limit to higher exposures by the factor $1/m_o^2$ (see Fig. 20), whereas the f_r functions of the RBV camera are displaced only by $1/m_o$ because the beam-noise term contains a cancelling factor (m_o).

A smaller black-level bias (V_o) reduces the beam noise but decreases the readout efficiency and the product decreases. A faster readout increases the currents, but not the potentials and results in a lower readout efficiency. A reduction of the readout time from 10 to 2 seconds, for example, reduces t/C to 15 secs/ μ F and shifts all RBV curves in Fig. 20 to higher exposures by a factor of 2.2.

The principal cause for the readout loss at low exposures is the exponential characteristic of the read beam. The effect of this characteristic is demonstrated by calculating the readout efficiency and beam noise for beams for an ideal cathode emitting monochromatic electrons at 0°K and from a solid-state emitter operating at room temperature 300°K, assuming electron optics with unit magnification. The results are shown in Table 9. A beam modulation $m_b = 0.3$ is retained because m_b is determined largely by electron reflection at the sensor.

Table 9—Readout and Beam Noise Loss for Low-Temperature (300°K) Electron Beams ($m_o = 1$). Values for Ideal (0°K) and Standard Beam Temperatures at the Sensor Are Also Given

| f_r | Temp. (°K) | m_b | $I_s/I^{1/2}$ | I_s (nA) | V_s (volts) | V_o (volts) | $1/\eta_c$ | Beam Noise Factor | Relative Sensi- tivity |
|-------|---------------|-------|---------------|---------------|------------------|------------------|------------|-------------------------|------------------------------|
| 40 | 0 | 0.3 | 0.145 | 0.021 | 0.000525 | 0.0 | 1.0 | 6.67 | 30.6 |
| 40 | 300 | 0.3 | 0.145 | 0.091 | 0.008 | 0.03 | 3.52 | 28.6 | 2.03 |
| 40 | Standard | 0.3 | 0.145 | 0.205 | 0.0165 | 0.5 | 3.22 | 63.5 | 1.0 |
| 20 | 0 | 0.3 | 0.054 | 0.0029 | 0.0000725 | 0.0 | 1.0 | 6.67 | 78.5 |
| 20 | 300 | 0.3 | 0.054 | 0.029 | 0.0029 | 0.03 | 4.0 | 75.5 | 1.73 |
| 20 | Standard | 0.3 | 0.054 | 0.076 | 0.0062 | 0.5 | 3.27 | 160.0 | 1.0 |

For a monochromatic beam (0°K) the signal currents and potentials become extremely small for a given resolving power because the relative sensitivity is increased by a large factor over that of a normal beam. The more realistic 300°K beam provides a relatively small increase in sensitivity. When used in a real camera, actual electron temperatures increase and the improvement is smaller because of

electron energy spread in the focusing system.* It is pointed out that a nearly monochromatic beam is not a practical solution because it images the field mesh. The beam does not go sufficiently out of focus between nodal points. A solid-state readout by direct contact has amplifier noise problems. Sensors with lower storage capacitance can be used to increase the potentials and readout efficiency at low exposures. This advantage is traded for a lower MTF (because of the greater thickness of the sensor) and a lower maximum charge density, which limits the maximum resolving power. This situation is analogous to a change of grain size in photographic emulsions where larger grains provide higher signals for a given exposure and quantum efficiency but cause a reduction of MTF and resolving power. The best solution for eliminating readout noise is a gain mechanism in the sensor or preceding charge storage and readout. The first solution is similar to the local amplification from atoms to grains in a photographic emulsion but requires separation of the sensor and storage surface and an additional focusing system in television camera tubes as for light intensifiers preceding charge storage (used in low-light-level television cameras). The additional electron optic degrades the MTF and resolving power of a high-definition camera. Sophisticated designs may approach an overall maximum resolving power of 100 cycles per mm. It follows that optimum performance at lower exposures requires a specialized sensor and charge storage section as in photographic cameras.

The efficiency of photographic and high-definition television cameras can be compared by the relative locations of their resolving-power functions and quantum limits shown in Fig. 20. The $\frac{1}{2}$ -power lines $f_r(\bar{E}_0)$ at the left side are the quantum-limited resolving power functions of perfect cameras determined by Eq. [6.5]. These quantum limits move to higher exposures by factors $1/m_o^2$ for lower contrasts. The horizontal spacings between those lines and the corresponding resolving-power functions $f_r(E_{0.5})$ of the real camera are the exposure factors, numerically equal to the reciprocal detection efficiency ($1/\eta_f$). The broken-line extensions of the initial slopes of the RBV curves are the f_r functions computed for unit MTF (Compare Fig. 9) readout and beam-noise loss is given by the horizontal spacings of these functions to the quantum limit curves $f_r(\bar{E}_0)$.

The broken-line curves show the quantum limits and resolving-power functions of photographic cameras.

The efficiency of the conversion process from input quanta to

* The electron temperature from the cathode of a "standard" electron gun (1160°K) is increased to 2000-3000°K at the sensor, because of the magnification in the electron optics of the gun and the focusing system: $T_{B(\text{sensor})} \approx T_E/M_o^2M_f^2$.

photoelectrons, silver atoms, and grains in the photographic emulsion can be appraised by writing an equation for the exposure similar to Eq. [6.6],

$$\bar{E}_{0.5}(f_r) = \bar{E}_{o(f_r)}/\eta_f = \bar{E}_o \left[\left(\frac{c}{\epsilon_1 \epsilon_2} \right) \left(\frac{1}{\eta_c \gamma^2} \right) \left(\frac{1}{r\bar{\Delta}} \right)^2 \right] f_r \quad [6.7]$$

The factor c is an electron trapping factor (similar to the dielectric factor of ASOS sensors), ϵ_1 is the efficiency of the primary process, ϵ_2 the efficiency of the conversion process to silver atoms, and $\eta_c \gamma^2$ is the development or readout efficiency, which must have a built-in threshold to prevent thermal exposure and goes to zero at high exposures because of the finite number of developable grains in the emulsion. The total conversion loss (first two products) is obtained by computing f_r for $r\bar{\Delta} = 1$. The 3414 film, for example, would give the high resolving powers indicated by crosses at $E = 0.317$ mcs for three contrasts. The spacings from these points to the quantum limit curves indicate a maximum overall conversion efficiency (without MTF loss) slightly less than one percent. The same result is obtained for the other film types.

The circles on the $1/2$ -power lines are the "rated resolving powers" of 5 film types for $C. = \infty$. These values are degraded only by the MTF product of the films and the microscope objectives used in resolving-power tests. The TRI-X value on the line is computed from the published MTF curve of the film; the rated value for this film is higher. The MTF loss caused by the perfect F/5.6 camera lens is obviously larger for the high-definition film cameras.

A film "speed" rating is given by the Aerial Exposure Index (E.K.) along the top of Fig. 20.

References:

- ¹ O. H. Schade, Sr., "An Evaluation of Photographic Image Quality and Resolving Power" *J. SMPTE*, Vol. 73, p. 81, Feb. 1964.
- ² O. H. Schade, Sr., "The Resolving Power Functions and Quantum Processes of Television Cameras," *RCA Review*, Vol. 28, p. 460, Sept. 1967.
- ³ O. H. Schade, Sr., "High Resolution Return Beam Vidicon Cameras: A Comparison With High Resolution Photography," *J. SMPTE*, Vol. 79, p. 694, Aug. 1970.
- ⁴ O. H. Schade, Sr., "Electron Optics and Signal Readout of High Definition Return Beam Vidicon Camera," *RCA Review*, p. 60, March 1970.
- ⁵ W. H. Chammam and A. Olin, *Photo. Science and Eng.*, Vol. 9385, p. 397, Dec. 1965.

Techniques for High-Data-Rate Two-Dimensional Optical Pattern Recognition

R. Croce and G. Burton

RCA Advanced Technology Laboratories, Burlington, Mass.

Abstract—Two optical processing systems are described that reduce complex two-dimensional information to a level that can easily be interpreted by an operator or a small special purpose computer. The data reduction is accomplished by preprocessing optical data using two dimensional adaptive filtering techniques, providing direct conversion of the pre-processed data to electrical signals, and performing parallel processing of the resulting electrical signals. The heart of the systems is the ability to interface between the optical and electrical signal-processing operations and to provide mechanisms for adaptive feedback control from an operator or computer.

The systems incorporate components that have undergone significant improvement in performance characteristics over recent years. These include adaptive two-dimensional spatial filters, optical sensor arrays, analog parallel-processing logic circuits, and high-resolution return-beam-vidicon cameras.

Optical processing systems are shown to offer an advantage over digital systems, especially when the imagery to be processed has information content greater than that normally contained in television imagery.

Introduction

Two-dimensional optical image-processing systems offer a potential for tremendous time saving when searching large amounts of image material for information content. Recognition systems can relieve an operator of much tedious searching, by scanning the input imagery

and signaling the occurrence or position of a predetermined set of two-dimensional objects, e.g., optical character recognition. Enhancement systems present the operator with a modified version of input imagery that is more readily analyzed. An excellent review of two-dimensional optical processing techniques and application are found in Reference 1.

These image processors have potential application in areas such as reduction of data for transmission purposes; screening of photographic reconnaissance imagery by evaluating image quality and picture content; processing of data received from satellites to determine cloud motion or improve picture quality; character reading; and map matching. One-dimensional optical processors, although successfully applied (see Refs. (2)-(4) for examples), are special cases of two-dimensional processors and generally operate at lower data handling rates.

The main advantages of an optical over a digital processor are a large time-bandwidth product, high data input rate due to the ability to handle two-dimensional data in parallel fashion, and ease of forming the two-dimensional Fourier transform of large images.

Despite these advantages, however, application of optical processing systems on a wide scale has been limited. One of the reasons for this has been their inability to interface efficiently between the optical and electrical signal domains and to provide adaptive capabilities. Thus, a hybrid processor that would combine the input and preprocessing capability of an optical system and the decision making and adaptive ability of a digital system or a system with direct operator feedback is very desirable.

The recent development of a number of optical techniques and components has made feasible certain operations and system configurations that can now overcome some of the obstacles to a hybrid system. Two possible hybrid processing systems that demonstrate the implementation of a recognition and an enhancement system are discussed.

Digital Processing of Two-Dimensional Data

Digital image processing generally involves the following four steps:

1. Scanning of an input transparency producing digitized image data
2. Operating on the digital data to generate a signal function such as the discrete Fourier transform (DFT)
3. Convolution of the signal function with a reference function.
4. Conversion of the convolved data into an output image or operating on that data with pattern recognition algorithms.

Match filtering may be performed by using a reference function matched to the pattern of interest and then detecting correlation (amplitude) peaks in the resulting output data. The reference function can also be selected to modify the input data so as to enhance significant image characteristics. Digital computer image processing offers the advantages of ease of implementing amplitude and phase functions and the ability to perform certain nonlinear processes.

To illustrate the process of taking the two-dimensional discrete Fourier transform by a digital computer, consider an image having N^2 elements and 64 gray levels. The Fourier transform of the sampled image $f(l,k)$ is given by

$$G(r_x, r_y) = \sum_{l=0}^{N-1} \sum_{k=0}^{N-1} f(l,k) \exp \left\{ \frac{2\pi j}{N} (kr_x + lr_y) \right\}$$

where

$$r_x = 0, 1, 2 \dots, N-1,$$

$$r_y = 0, 1, 2 \dots, N-1,$$

or

$$\begin{aligned} G(r_x, r_y) &= \sum_{l=0}^{N-1} \exp \left\{ \frac{2\pi j l r_y}{N} \right\} \left\{ \sum_{k=0}^{N-1} f(l,k) \exp \left\{ \frac{2\pi j k r_x}{N} \right\} \right\} \\ &= \frac{1}{N} \sum_{l=0}^{N-1} F(r_x, l) \exp \left\{ \frac{2\pi j l r_y}{N} \right\} \end{aligned}$$

The term $F(r_x, l)$ is simply the one-dimensional discrete Fourier transform of each line in the picture, i.e., k assumes values from 0 to $N-1$ corresponding to the sampled values along any line l . The transform $G(r_x, r_y)$ is produced by taking the transform of each line forming $F(r_x, l)$, and then rotating the image 90 degrees and taking a second Fourier transform. The term $f(l,k)$ represents the N^2 samples of the image, with each sample quantized according to image brightness into 64 levels represented by six bits. The number of Fourier coefficients produced is N^2 , corresponding to the initial number of picture samples, and the number of quantizing levels for each N coefficients is six bits,⁵ corresponding to the picture gray scale.

The scanning devices usually employed for entering image data into a computer include flying-spot scanners, direct electron-beam

readers, laser-beam scanners, Nipkow disks, linear arrays of diodes, and two-dimensional diode arrays. For good resolution and high signal-to-noise ratio, the scanning rate is limited, and the quantized signal level must be about two to three times the value of the rms noise. The scanning processes generally involve such difficulties as

1. controlling scanning-beam shape and scan linearity,
2. maintaining an accurate gray-scale reproduction in the output image,
3. high cost and maintenance requirements of the scanning system,
4. low data handling rate (since the time to take N^2 samples quantized to 2^4 levels is proportional to AN^2).

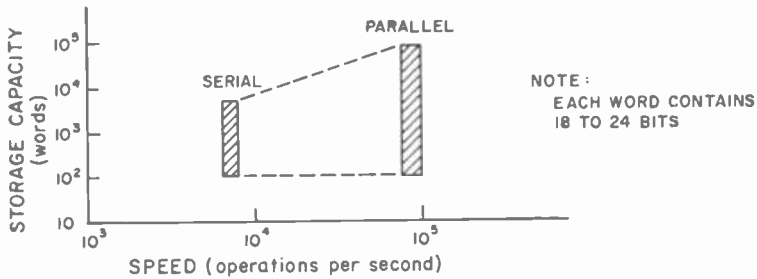


Fig. 1—Capacity and speed of a “small” computer.

The main drawback associated with digital processors is that trade-offs must inevitably be made between resolution, processing time, and the size and complexity of the computer to be used. Computer size is related to computer speed and memory capacity. For example, a “small” computer may be defined as one having the capacity and speed shown in Fig. 1. Although computers may be designed specifically for the parallel processing of large quantities of data (i.e., the Illiac 3 and 4 at the University of Illinois), they are large and expensive.

Complementary metal oxide semiconductor (CMOS) computers currently under development fall into the small-computer category. These “mini-computers” are small in size, light in weight, and have low power consumption, but their processing capabilities in terms of speed and storage capability fall far below that required to process large volumes of high-resolution ($1,000 \times 1,000$ lines) two-dimensional input data at high rates. The computational requirements for performing convolution and Fourier transformations, assuming 10^5 operations per second, are presented in Table 1. It should be noted that the informa-

Table 1—Computational Requirements for Performing Convolution and Fourier Transforms

| Mathematical Function | | Formula ^a | B, Number of Operations (upper bound) ^b | N ^b | Computation Time (C, B) ^c |
|-----------------------|---------------------------------|--|---|------------------------------------|--------------------------------------|
| One Dimension | Discrete Time ^d | $\sum_{k=0}^{N-1} g(x_k) h(x_q - x_k), q = 0, 1, \dots, N-1$ | N ² (for all q) | 1024 8192 | 10 sec 10 min |
| | Discrete Frequency ^e | $\sum_{r_x=0}^{N-1} G(r_x) H(r_s) \exp \left\{ \frac{2\pi j k r_s}{N} \right\}$ $k = 0, 1, 2, \dots, N-1$ | Direct 3N ² + N FFT 6N log ₂ N + N | 1024 8192 | 30 sec 33 min 0.6 sec 6 sec |
| Two Dimensions | Discrete Time | $\sum_{k=0}^{N-1} \sum_{l=0}^{N-1} g(x_k, x_l) h(x_q - x_k, y_w - y_l)$ $q, w = 1, 0, \dots, N-1$ | N ⁴ | 10 ² 10 ³ | 17 min 2800 hr |
| | Discrete Frequency ^f | $\sum_{r_x=0}^{N-1} \sum_{r_y=0}^{N-1} G(r_x, r_s) H(r_s, r_y) \exp \left\{ \frac{2\pi j (r_x k + r_y l)}{N} \right\}$ $l = 0, 1, 2, \dots, N-1$ $k = 0, 1, 2, \dots, N-1$ | Direct 3N ⁴ + N ² FFT 12N ² log ₂ N + N ² | 10 ² 10 ³ | 51 min 8400 hr |
| Convolution | | | | 10 ² 10 ³ | 8 sec 20 min |

Table 1—Computational Requirements for Performing Convolution and Fourier Transforms—(continued)

| Mathematical Function | | Formula ^a | B, Number of Operations (upper bound) ^b | N ^b | Computation Time (C _t B) ^c |
|-----------------------|----------------|---|--|--|--|
| Fourier Transform | One Dimension | $G(r_x) = \sum_{k=0}^{N-1} g(x_k) \exp \left\{ \frac{-2\pi j k r_x}{N} \right\}$ $r_x = 0, 1, 2, \dots, N-1$ | Direct N ² | 1024 8192 | 10 sec 11 min |
| | Two Dimensions | $G(r_x, r_y) = \sum_{k=0}^{N-1} \sum_{l=0}^{N-1} g(x_k, y_l)$ $\exp \left\{ \frac{-2\pi j (k r_x + l r_y)}{N} \right\}$ $r_x = 0, 1, 2, \dots, N-1$ $r_y = 0, 1, 2, \dots, N-1$ | FFT 2N log ₂ N Direct N ⁴ | 1024 8192 10 ² 10 ³ | 0.2 sec 2.0 sec 17 min 2800 hr |
| | | | FFT 4N ² log ₂ N | 10 ² 10 ³ | 1.7 sec 4 min |

^a $r_x = f_x NX$ where f_x is the spacial frequency in the x dimension.
^b N is the number of sample points along one dimension.
^c C_t , the time to perform one multiplication and addition, is assumed to be 10 μ s.

^d References 6 and 8.
^e Reference 7.
^f Reference 6.
^g References 5 and 6.

tion in Table 1 does not reflect the improvements attainable using Hadamard transforms⁸ and pipeline fast Fourier transforms,⁹ and does not include the additional time required to scan the input image or display the final output. Storage requirements are proportional to N for the one-dimensional case and N^2 for the two-dimensional case.

Consideration of the computer time and storage requirements leads to the conclusion that computers, over the next few years, will not be able to compete efficiently with the data-handling rates of optical processors when performing complex computations involving the convolution or transformation of two-dimensional inputs having resolutions greater than those associated with normal television systems. The purpose of the hybrid processing schemes developed in the following sections is to circumvent these computational difficulties by using an optical processor to perform the sampling, Fourier transformation, and filtering operations, while using a small computer to handle the control and decision functions.

The discussion presents two base-line processing schemes for high-data-rate, two-dimensional optical pattern recognition and image enhancement. These systems incorporate new devices and techniques that have been developed at RCA Laboratories, Princeton, N.J., at the RCA Advanced Technology Laboratories at Camden, N.J. and at Burlington, Mass. The processing schemes described afford semi-automated systems that either recognize or assist an operator in recognizing a particular two-dimensional object in a set of objects and/or in background clutter.

Two-Dimensional Feature Identification by Frequency-Domain Sampling

In the scheme shown in Fig. 2, two-dimensional pattern recognition is performed by sampling the two-dimensional Fourier transform of the input image. Sampling is accomplished by properly configuring an array of photosensors located in the Fourier transform plane of an optical system.

Before specifying the array to be used to sample the Fourier spectrum, consideration must be given to available methods of decoding the array. Although a large-area array represents the ultimate in processing capability, it is presently not possible to integrate large-area sensors and decoders in such a way that every photosensor can be integrated with its own amplifier and processing logic. The possibility of a large sensor array having only a limited number of output leads, with each output selected on the basis of the absolute value of the energy at each photosensor, does not appear feasible in the near future.

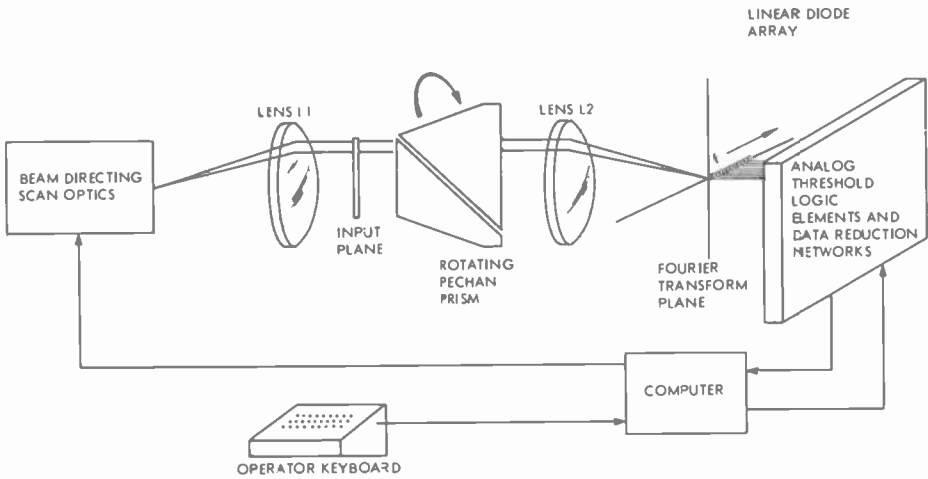


Fig. 2—Two-dimensional pattern recognition by frequency-domain sampling.

In the scheme under discussion the array is linear and consists of 100 photodiodes, with the transform rotated over the array by means of a rotating Pechan prism located between the input plane and lens L2 as shown in Fig. 2. The operation results in a two-dimensional sampling of the transform. Alternatively, other inverting type prisms such as an Abbe prism may be used or the array itself could be rotated.

The diodes in the linear array are read out in parallel, maintaining the high bit rate inherent in the optical processor. The basic operation performed is the extraction of feature information contained in the Fourier transform of the input transparency. Preprocessing of this information is performed in parallel by making comparisons between the relative energy content in each of the (spatial) frequency channels, as indicated by the magnitude of the signal from each photosensor. A parallel processing logic technique is shown schematically in Fig. 3. This technique incorporates analog threshold logic (ATL), which has been successfully used on real-time flash-detection, voice-recognition, and engine-testing systems. The features selected in this scheme characterize the Fourier spectrum of the input object by its slope features, i.e., negative, positive, maximum, or minimum slope features.

The basic ATL element has a dc output that is linearly proportional to the sum of the two inputs from adjacent diodes provided this sum is above a predetermined threshold and less than that which would exceed the saturation limit of the circuit. By using ATL elements, not

only the presence or absence of a feature but also its relative magnitude is detected, thereby transferring more information to the subsequent processing and decision circuits. The extracted features may be classed as sustained for those occurring at a fixed time or dynamic for those that occur as a function of time, i.e., as the prism rotates.

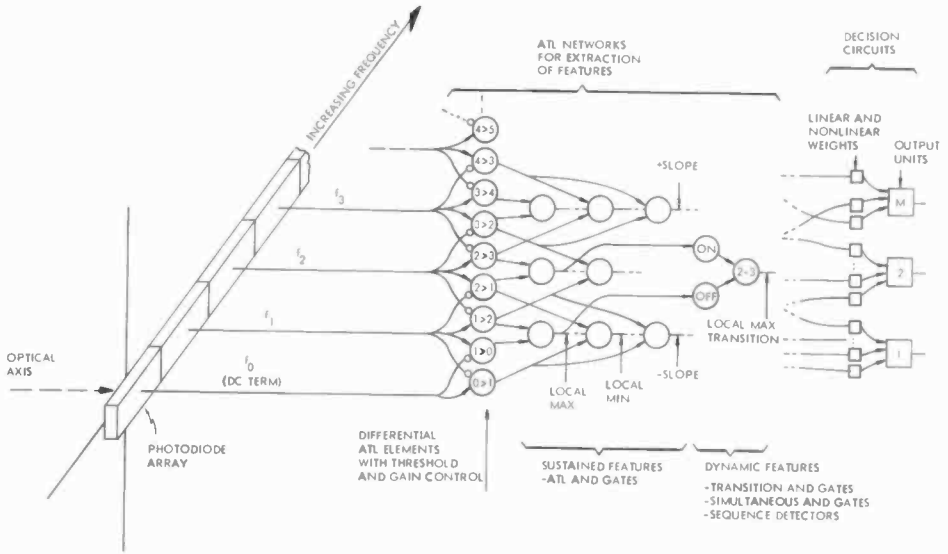


Fig. 3—A parallel-processing logic technique employing analog threshold logic.

The input transparency* to be examined is placed in the input plane shown in Fig. 2. A beam from the variable-aperture laser scanning system is used to scan the transparency. The beam size is determined by the image (target) size, which is estimated from a priori knowledge; e.g., aircraft altitude and related factors in the case of aerial photographs. For high signal-to-noise ratios, ideally only one target and minimal background should be in the beam at any one time. To increase data rate in a practical system, however, a beam having a diameter 3, 5, or even 10 times the maximum target dimension may be used.

* Although current research appears promising, at the present time there is no generalized real-time read-write medium that can replace a film transparency as the input. When such a medium becomes available, it can be incorporated directly into either of the schemes described. One obvious application would be the direct processing of video signals.

Pre-sensor processing could be performed by imaging various filter functions onto a temporary storage medium located in front of the photosensitive array. Since the detectors are located in the Fourier plane, only real filter functions would be used. For example, a typical real filter function might weight the spatial frequency components by attenuating the low-frequency terms and passing the high-frequency terms. The implementation of a filter projection system is detailed in the next section.

Target features to be recognized are programmed into the system by a small computer that controls the decision logic (gain or threshold settings) of the ATL elements. The computer also controls the size of the scanning beam and selects the proper pre-filter to be used in the system, based on information supplied by the operator via keyboard entry.

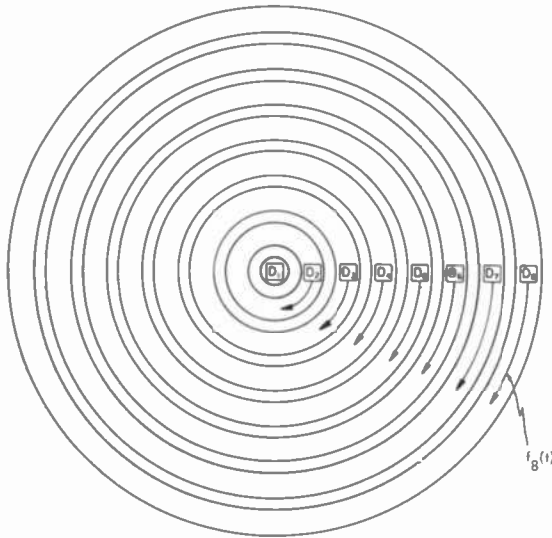


Fig. 4—Scanning by rotating fourier transform over the linear array.

1. Scanning and Feature Extraction

The scanning operation produced by rotating the Fourier transform over the linear array is depicted in Fig. 4. Image features may be extracted in two directions simultaneously. The first extraction may

be made along the detector array, while the second may be made by examining the waveform sets generated by the rotation of the Fourier transform across the diode array. This is similar in concept to a sampling scheme described in Ref. (10).

As the spatial Fourier spectrum of the input image is rotated through diode D_d , the signal generated is given by $f_d(t)$. The signal $f_d(t)$ is periodic, where the period T is the time required for the transform to make one complete rotation. At any given sample time t_k the signal from diode D_d is given by $f_d(t)_k$. Time in this system is related to rotation of the image, whereas the radial position of diode D_d in the Fourier plane corresponds to spatial frequency.

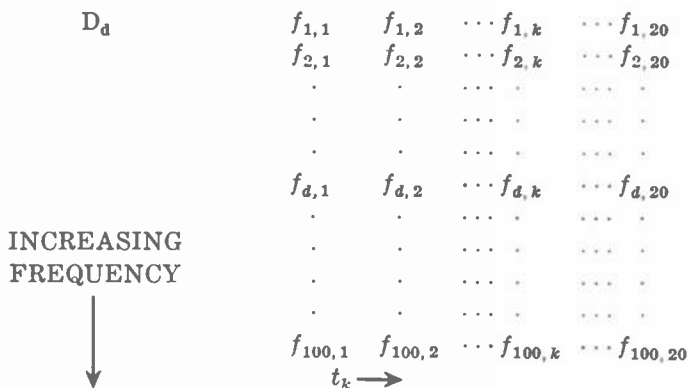


Fig. 5—Matrix of samples of 100 diodes sampled 20 time during one image rotational period.

Although a linear array of 100 photosensors is assumed, it is possible to consider the sensors as producing a two-dimensional field; i.e., the 100 sample points at time t_k may be delayed and compared to the sample points at some other time t_r , as the Fourier transform is rotated. If the array is sampled 20 times during one rotation of the image, the field, when combined with the appropriate delays, would consist of an array of 100 by 20 samples. The resulting matrix of points is shown in Fig. 5, with sample point f_{dk} corresponding to the output of the d th diode at time t_k , with the proper delay settings necessary to compare all the points at time t_r , given by $\Delta t = t_r - t_k$. Methods for reducing the 100 by 20 array of samples f_{dk} to a smaller N by K array of samples are presented in the Appendix.

In the sensor field shown in Fig. 5, the rows correspond to a particular spatial frequency channel, with the lowest frequency corresponding to the top row and succeeding rows corresponding to successively higher frequencies.

Since the shape characteristics of the spectrum contain the important feature information, the analog threshold elements indicated in Fig. 3 are configured to pick out sustained variations (i.e., peaks, nulls, and frequency slope magnitude) along the diode array and dynamic variations as a function of time. When a predetermined number of such variations have been found, a detection is indicated. The total number of detected variations is independent of orientation of the image. Due to the nature of Fourier transforms, translation of the object in the input plane does not affect the intensity distribution (or decision logic) in the Fourier plane. Therefore, the recognition scheme involves a translation- and rotation-invariant algorithm.

The final method selected for extraction and image classification ultimately determines the amount of processing logic to be integrated with the sensor array and the size of the computer required. In addition to the ATL techniques, various other classification methods may be used to simplify and/or optimize the processing of sensor data.^{11, 12, 13}

2. Size-Invariant Algorithm

The frequency extent of a Fourier transform is inversely proportional to the size of the stimulus object in the input plane. Therefore, although the Fourier transform of a given object retains its relative shape, the spread along a frequency axis changes with object size. Since the decision logic necessary to recognize the transform is sensitive to the frequency spread, the decision logic must be modified (by changing gain or threshold settings) according to the size of the input image. The fact that the shape of the transform is a function only of the object type, however, can lead to the development of an iterative size-invariant algorithm based on the sample $f_d(t_k)$. If the presence of a particular target in a certain target set is assumed, it is possible to test this assumption by estimating the size that the target must have been to produce the observed transform by determining the number of frequency channels that contain a significant amount of signal energy. The proper decision logic for that object type can then be implemented and the final decision made as to whether the assumed object type is indeed present.

The total energy per channel may be found by integrating the output

of each photosensor during one rotation, or by summing the values of the samples taken during one rotation of the image.*

3. Noise Sources

There are two primary sources of noise in this processing scheme: photodetector noise and amplitude variation. Photodetector noise arises from the detector dark current (a Poisson-distributed random process for small signals), thermal noise (a Gaussian-distributed process whose samples are independent), and noise current generated by the signal current (which is Poisson-distributed for small signals). The laser fluctuations originate in thermal sources and are also Gaussian. If a sufficiently large signal is assumed, all the processes can be considered as Gaussian.

4. Preliminary Design Parameters

The following design parameters are being incorporated into a feasibility unit since they can easily be implemented with presently available components. The input transparency is assumed to be a 35-mm frame containing 14 lines/mm or 333 by 500 resolution elements on a 24- by 36-mm format. The input is scanned by an overlapping pattern as shown in Fig. 6. The two dimensional scanning system may be a pair of ultrasonic light modulators, galvanometer deflectors, or motor-driven mirrors. The galvanometer-type deflector is selected for this initial base-line system, since it is a proven device of moderate cost having good operational characteristics.

The maximum size of the scan beam is initially assumed to encompass 100 resolution elements across the diameter of the input imagery, corresponding to 100 resolution elements in the Fourier plane. For a smaller scanning aperture the number of resolution elements in the Fourier plane decreases due to aperture constraints.

It is assumed that each of the 100 diode elements has a diameter of 25 μm , which corresponds to the state of the art in available arrays. The Fourier transform lens is selected so that the diffraction-limited spot size, δ , is within the 25 μm diameter, or

$$\frac{F}{D} = f/n_0 \leq \frac{\delta}{2.44\lambda} = 16.4,$$

* If negligible energy is found in the higher-frequency channels, those channels may be eliminated during subsequent processing of that particular sample, thus effecting a preliminary reduction in the volume of data that has to be handled.

where the wavelength $\lambda = 6328 \text{ \AA}$, and $\delta = 25 \text{ }\mu\text{m}$. Assuming an f number equal to 8 for a lens with a diameter, D , of 50 mm, the focal length is 450 mm. Since the spread of energy in the Fourier plane is given by

$$v_{\max} = Ff_s\lambda$$

where f_s , the highest spatial frequency on the input film, is equal to 14 lines/mm, then

$$v_{\max} = 3.54 \text{ mm.}$$

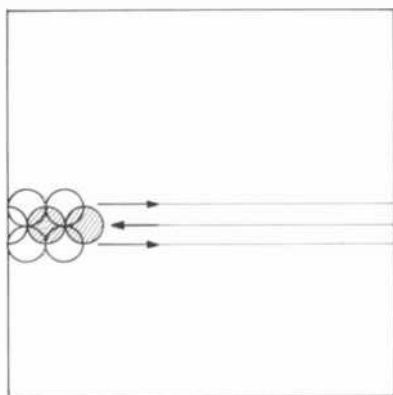


Fig. 6—Overlapping scan pattern.

A maximum extent of 3.54 mm for the diode array (an element spacing of $3.54 \text{ }\mu\text{m}$) corresponds to practical array technology.

Optical Filtering Using Real and Complex Filter Techniques

The second scheme, shown in Fig. 7, uses matched filter and image-enhancement techniques to increase the operator's ability to distinguish two-dimensional patterns within the transparency.

New material and the rapid advances in coherent optics and holography have made it possible to perform spatial filtering in the Fourier transform plane by use of read-write storage media, thereby producing a processor capable of adaptive filter control. The material selected for use as read-write storage media must have the following characteristics:

1. Sufficiently high sensitivity at wavelengths compatible with currently available lasers so that an image may be stored at a high data rate.
2. A thickness compatible with the depth of focus of the optics used in the processing system.
3. Little fatigue at the wavelength selected for readout, but capable of fast erasure.
4. Good uniformity and optical quality.
5. Resolution comparable to that of the input transparency.

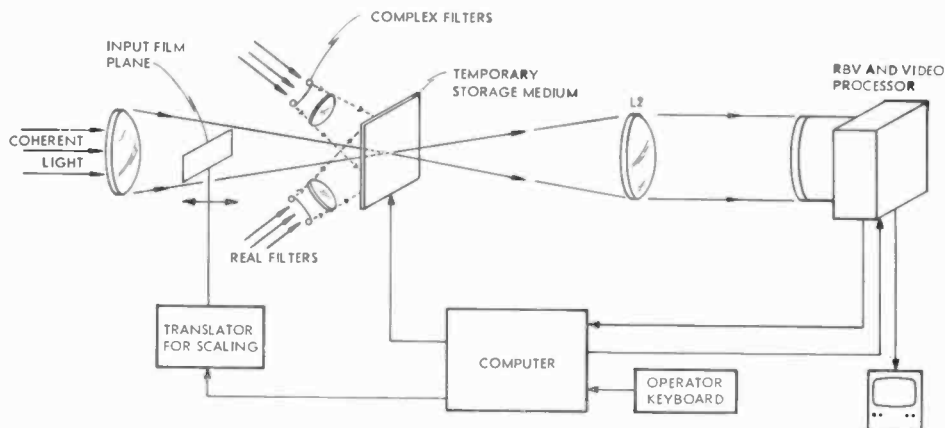


Fig. 7—Two-dimensional pattern recognition technique employing matched filters and image-enhancement.

Potential storage materials include: organic¹⁴⁻¹⁶ and inorganic¹⁷ photochromics; thermoplastics;¹⁸ electro-optic materials such as zinc sulfide,¹⁹ lead zirconate-lead titanate ceramics,^{20,21} and bismuth titanate;²² magnetic storage (of binary filters)²³ in manganese bismuth;^{24,25} electron-beam-addressed KDP and KP*P crystals;^{26,27} lithium niobate and barium sodium niobate;²⁸ and use of the reversible phase transition in chalcogenide alloys.²⁹

The thermoplastic and electro-optic materials are presently the most attractive, since high sensitivity may be obtained by overcoating them with photoconductive materials. Image information may then be efficiently stored by a bulk transfer of the image as a charge pattern onto the surface of the photoconductor. The charge pattern produces an electric field across the material that causes a deformation of the heated thermoplastic or a change in the birefringent properties of the

electro-optic crystals. Further advantages of the thermoplastic materials are that upon cooling the information is frozen into the surface of the thermoplastic, resulting in no fatigue during readout, and the recorded image exhibits high diffraction efficiency.

Filter functions to be imaged onto the storage medium are stored in cassettes in an off-axis position, as shown in Fig. 7, and imaged onto the storage medium, which is located in the Fourier plane. Both real and complex filtering of the two-dimensional input functions are possible using this scheme.

Although a transparent medium is depicted in Fig. 7, the concept will work equally well for a reflective filter. In both cases, the registration accuracy at the Fourier transform plane is critical, and the ultimate accuracy required depends on the resolution in line pairs on the input imagery. One method of eliminating some of the requirements on the projection system is to store the filters on cassette as Fraunhofer holograms. The advantage of the Fraunhofer hologram projection is that the reconstructed image is relatively insensitive to the positioning of the filter frame in the cassette and can therefore be positioned quickly and accurately. Moreover, reconstructed images from Fraunhofer holograms, especially when stored on a phase media, are less susceptible to scratches such as might be caused by the transport mechanism.³⁰

In addition to the use of filters, image enhancement can be accomplished within the output display. A high-resolution return-beam-vidicon camera³¹ is attractive for this application, since it can store up to 10,000 lines per picture (sufficient for most imagery). The camera has the ability to be electronically zoomed, so that any area on the image can be enlarged and displayed on a lower-resolution monitor. Standard video signal-processing techniques, such as edge enhancement and gray-scale adjustment, may be used to complement the optical processor.

The relative scaling of the object transform and the filter transform shown in Fig. 7 may be changed by either moving the film plane with respect to the transforming lens, thereby changing the scaling on the object transform, or by using optics with zoom capability. Rotation of the two transforms with respect to each other can be accomplished optically or by rotating the filter plane storage medium.

In this processing scheme the operator has the option of controlling all functions through keyboard entry. He may, for example, improve contrast or produce edge enhancement by the proper filter functions, or he may regulate the picture gray scale in the camera video.

Correlation and matched filtering may be performed using complex filters. Two methods of improving the detection probabilities for the resulting correlation peaks are (1) to use the output signal-to-noise ratio as a criterion for determining the "goodness" of match of the filter selected, and (2) to use digital discrimination techniques such as those discussed in the literature.³³

In addition to producing matched filter functions, complex filters may also be used for scene subtraction or image enhancement.^{33,34} When used in this mode, differences that occur within a known scene are emphasized in the output image.

Assuming that the original input plane contains 1000 by 1000 resolution elements, the complex filter must store 1000 by 4000 resolution elements (considering the high frequency spatial carrier) in order to guarantee separation of the zero- and first-order terms in the output image. If the birefringent properties of the electro-optic devices discussed previously are used and if the polarizer losses are tolerable, these resolution requirements may be relaxed somewhat with any overlap between terms being countered by use of the polarizer.

The design of the lens to be used in the processor eventually requires a trade-off between cost and performance. One general rule is that if diffraction-limited operation is desirable, aberrations must be held below $\lambda/4$ to satisfy the Rayleigh resolution criteria.

Alternative Techniques

1. Self-Scanned Arrays

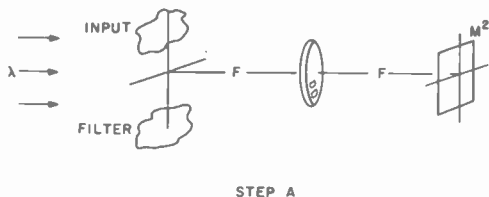
Large photoconductive arrays and decoders have been fabricated using thin-film technology.³⁵ These devices have application to the present configuration, since each element can be accurately addressed, allowing

1. Bit-by-bit regulation of gray-scale content,
2. The application of data compression and redundancy reduction techniques on a bit-by-bit basis,
3. High-resolution detection of edges.

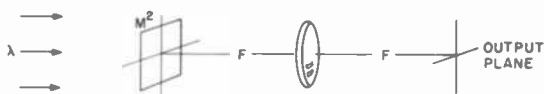
Ideally, circuits for performing these functions should be integrated with the photosensors; present technology requires, however, that these circuits be external to the array.

When compared to their vidicon counterpart, these arrays are smaller, require less power, and have longer life and are simpler and more flexible to operate. Also, they do not have the disadvantages (scan nonlinearity and loss of edge resolution) normally associated with beam-readout devices.

The largest arrays developed to date are 512 by 512 elements. Although still plagued by fabrication problems, these arrays have achieved a fair degree of success. They are not now recommended for incorporation into a system, but it is expected that advances in the next few years will make this possible.



STEP A



STEP B

2. Weaver-Goodman Technique

When a complex matched filter is to be used to detect a known signal in the presence of white noise, an alternative technique may be used to construct the filter function. This technique avoids the necessity for critical position accuracies inherent in forming a filter in the spatial frequency domain. This technique, known as the Weaver-Goodman technique³⁶ and shown in Fig. 8, is a two-step process requiring the on-line formation of an intermediate image on a square-law imaging medium (M^2) such as film, which is then used to produce the output correlation function via a coherent imaging system.

The possibility of using such a system to eliminate the need for producing and implementing complex storage functions is very attractive. The square-law property might be incorporated into the photoconductor layer of the sandwich-type devices discussed previously.

Appendix—Application of Pattern-Recognition Techniques— Data Reduction and Contrast-Invariant Algorithm

One of the principle difficulties historically encountered in the optical processing of information has been in developing a unit that can

accept a large number of sample points from a two-dimensional scene at high bit rates and convert these to a smaller number of points suitable for processing by parallel-processing (ATL) logic in conjunction with a dedicated or general-purpose computer. The computer would make a final decision as to the class of objects present or determine the next iteration required of the data. It is the purpose of this Appendix to indicate how pattern-recognition techniques developed for digital processing of information may be applied to this preprocessor to effect a data reduction and a contrast-invariant algorithm.

1. Continuous Form

The time waveform from diode D_a (generated by the rotation of the Fourier transform over the linear array) is $f_a(t)$ * and is assumed to be a function from an ergodic random process. By the theory of orthogonal functions this waveform may be approximated by

$$\hat{f}_a(t) = \sum_{j=1}^J f_{aj} \varphi_{aj}(t)$$

in the interval $a < t < b$.

The $\varphi_j(t)$ terms** forms an orthonormal set in the interval $a < t < b$, and f_{aj} is given by

$$f_{aj} = \int_a^b f_a(t) \varphi_j(t) dt.$$

The error for the approximation is

$$\epsilon_a = \int_a^b f_a^2(t) dt - \sum_{j=1}^k f_{aj}^2.$$

* The average value of the time waveform is assumed to be zero in this development. Since the waveform out of the diode is a positive waveform $g_a(t) \geq 0$, $f_a(t)$ will be assumed to be given by $f_a(t) = g_a(t) - \langle g_a(t) \rangle$.

** $\varphi_j(t)$ and λ_j will be used instead of $\varphi_{aj}(t)$ and λ_{aj} with the understanding that $\varphi_j(t)$ and λ_j apply to the output from one diode; i.e., $f_a(t)$.

This error is minimized by maximizing $\sum_{j=1}^J f_{dj}^2$. This maximization

is satisfied when the $\varphi_j(t)$ terms are solutions of

$$\lambda_j \varphi_j(t) = \int_a^b \varphi_j(s) r_d(t,s) ds,$$

where $\lambda_j = \langle f_{dj}^2 \rangle$, and $r_d(t,s)$ is the autocorrelation function of f_d .

The maximization procedure requires that $\varphi_j(t)$ terms be selected that correspond to the highest eigenvalues (λ_j) of $f_d(t)$. Since $\lambda_j = \langle f_{dj}^2 \rangle$, the proper choice of the $\varphi_j(t)$ terms produces the maximum value for f_{dj} . This procedure is used to determine J $\varphi_j(t)$ terms that result in J samples of f_{dj} where $j = 1, 2, 3, \dots, J$.

A contrast-invariant algorithm may be developed that forms the correlation coefficient ρ_{dj} of the $\varphi_j(t)$ and $f_d(t)$ terms instead of just f_{dj} .

$$\rho_{dj}(f_d(t), \varphi_j(t)) = \frac{\text{cov}[f_d(t), \varphi_j(t)]}{\sigma[f_d(t)]\sigma[\varphi_j(t)]},$$

where

$$\begin{aligned} \text{cov}[f_d(t), \varphi_j(t)] &= \langle f_d(t) \varphi_j(t) \rangle - \langle f_d(t) \rangle \langle \varphi_j(t) \rangle \\ &= \langle f_d(t) \varphi_j(t) \rangle \\ &= \int_a^b f_d(t) \varphi_j(t) dt = f_{dj}. \end{aligned}$$

Since $\langle f_d(t) \rangle$ was set equal to zero in this development, the last term $\langle f_d(t) \rangle \langle \varphi_j(t) \rangle$ disappears. If $g_d(t)$ is used, this term would be retained instead of $f_d(t)$. As a result the samples g_{dj} would be given by

$$g_{dj} = \int_a^b g_d(t) \varphi_j(t) dt = \int_a^b f_d(t) \varphi_j(t) dt + \langle g_d(t) \rangle \langle \varphi_j(t) \rangle.$$

Using this result

$$\begin{aligned} \text{cov} [g_d(t), \varphi_j(t)] &= \int_a^b f_d(t) \varphi_j(t) dt + \langle g_d(t) \rangle \langle \varphi_j(t) \rangle \\ &\quad - \langle g_d(t) \rangle \langle \varphi_j(t) \rangle \\ &= \int_a^b f_d(t) \varphi_j(t) dt, \end{aligned}$$

which is identical to the results obtained by using $f_d(t)$.

When determining the $\varphi_j(t)$ terms for the case where $g_d(t)$ is used, the following equation is used:

$$\lambda_j \varphi_j(t) = \int_a^b \varphi_j(s) \langle f_d(t) f_d(s) \rangle ds$$

where $f_d(t) = g_d(t) - \langle g_d(t) \rangle$ and $\lambda_j = \langle f_{dj}^2 \rangle$. Hence, it may be seen from the foregoing discussion that subtracting the dc component $\langle g_d(t) \rangle$ from the input signal prior to the filter function $\varphi_j(t)$ is equivalent to subtracting the product of the time average of the filter function $\langle \varphi_j(t) \rangle$ and $\langle g_d(t) \rangle$ from the signal out of the filter. The former is easier to implement and will be assumed.

From the expression for ρ_{dj} the terms $\sigma[f_d(t)]$ and $\sigma[\varphi_k(t)]$ are simplified, since $\langle f_d(t) \rangle = 0$ and $\langle \varphi_j^2(t) \rangle = 1$, so that

$$\begin{aligned} \sigma[f_d(t)] &= \langle f_d^2(t) \rangle^{1/2}, \\ \sigma[\varphi_j(t)] &= (1 - \langle \varphi_j(t) \rangle)^{1/2}, \end{aligned}$$

and

$$\rho_{dj} = \frac{f_{dj}}{\langle f_d^2(t) \rangle^{1/2} (1 - \langle \varphi_j(t) \rangle)^{1/2}}.$$

If the time average of $\varphi_j(t)$ is zero,

$$\rho_{dj} = \frac{f_{dj}}{\langle f_d^2(t) \rangle^{1/2}},$$

which states that the samples f_{dj} are normalized by the rms value of the signal $f_d(t)$. When $\langle \varphi_j(t) \rangle \neq 0$, f_{dj} is normalized with respect to $(\langle f_d^2(t) \rangle - \langle \varphi_j(t) \rangle^2)^{1/2}$. When $\varphi_j(t) = f_j(t)$, $\langle \varphi_j(t) \rangle = 0$.

2. Discrete Form

The output from the linear diode array containing 100 diodes at time t_k is represented by F_k , the vector of samples ($f_{1k}, f_{2k} \cdots f_{50k}$) from a Gaussian process. The covariance matrix of F_k is given by:

$$B_k = \langle F_k F_k^T \rangle = \begin{vmatrix} \langle f_{1k} f_{1k} \rangle & \langle f_{2k} f_{1k} \rangle & \cdots & \langle f_{50k} f_{1k} \rangle \\ \langle f_{1k} f_{2k} \rangle & \langle f_{2k} f_{2k} \rangle & \cdots & \cdot \\ \cdot & \cdot & \cdots & \cdot \\ \langle f_{1k} f_{50k} \rangle & \cdots & \langle f_{50k} f_{50k} \rangle \end{vmatrix}$$

To reduce the vector set to a smaller N -dimensional vector where $N < 50$, a vector w_{kj} is chosen such that

$$w_{kj}(B_k - \lambda_j I) = 0.$$

Now the solution may be found for w_{kj} and the w_{kj} terms corresponding to the $J = N$ largest eigenvalues λ_j chosen. The w_{kj} terms will be represented by w_j terms with the understanding that they apply to a particular vector F_k . The detection scheme then becomes

$$\begin{pmatrix} X_1 \\ X_2 \\ \cdot \\ \cdot \\ \cdot \\ \cdot \\ X_N \end{pmatrix} = \begin{pmatrix} W_1^T \\ W_2^T \\ \cdot \\ \cdot \\ \cdot \\ \cdot \\ W_N^T \end{pmatrix} \begin{pmatrix} f_{1k} \\ f_{2k} \\ \cdot \\ \cdot \\ \cdot \\ \cdot \\ f_{nk} \end{pmatrix}$$

where $W_j^T = [W_{j1}W_{j2} \cdots W_{jn}]$

$$X_1 = W_{11}f_{1k} + W_{12}f_{2k} + \cdots + W_{1,100}f_{100,k}$$

$$X_2 = W_{21}f_{1k} + W_{22}f_{2k} + \cdots + W_{2,100}f_{100,k}$$

\(\cdot\)
 \cdot
 \cdot
 \cdot
 \cdot
 \cdot

$$X_N = W_{N1}f_{1k} + W_{N2}f_{2k} + \cdots + W_{N,100}f_{100,k}$$

and the circuit implementation is as shown in Fig. 9. Similar to the continuous case, this may be normalized with respect to the input energy such that the correlation coefficient in discrete form is given

by P_{jk} where $\sum_{j=1}^{50} W_j^2 = 1$ and,

$$P_{jk} = \frac{X_{jk}}{\left[\frac{\sum_{j=1}^n f_{jk}^2}{n} - \frac{\sum_{j=1}^n f_{jk}^2}{n^2} \sum_{j=1}^n W_j \right]^{1/2}}$$

This analysis also applies to the sample vectors F_d containing samples $(f_{d1}, f_{d2}, f_{d3} \cdots f_{dk})$ from the time waveform $f_d(t)$ where k represents the number of times $f_d(t)$ is sampled during one period.* Hence, the two-dimensional array of sample points may be reduced in

* Using the data reducing algorithm with k set equal to 20 produces $J = K < 20$ sample points.

two directions by considering (1) samples along the diode array and (2) samples taken while the image is scanned.

Note, however, that $W_{jd} \neq W_{jk}$, and, therefore, the result of reducing the matrices in two directions is to produce two new matrices; i.e., an $N \times 20$ matrix and a $100 \times K$ matrix. Techniques for combining these matrices into a single $N \times K$ matrix remain to be investigated.

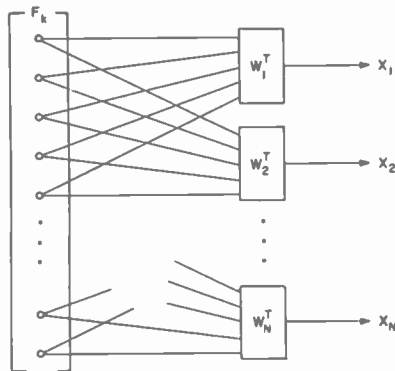


Fig. 9—Circuit implementation of detection scheme.

In addition to selecting the proper P_{jd} and P_{jk} terms (corresponding to the vector rows and columns), in order to characterize the signals it is also necessary to determine the divergence between the various signals as a function of the P_{jd} and P_{jk} terms selected since the above analysis does not guarantee good discrimination. This is accomplished by forming the likelihood ratio U of the various patterns (two at a time) and determining their divergence from

$$J \equiv \langle U|A_i \rangle - \langle U|A_j \rangle,$$

where A_i and A_j represents pattern i and j , respectively, and $U|A_i$ is the log of the likelihood ratio given that pattern i is present.

Conclusion

The main advantage of optical processors is the ability to pre-process data in parallel at high rates. The main drawback encountered has been the lack of suitable input and output devices. Recent improvements in photosensor arrays, read-write storage materials, parallel processing logic, and high resolution display devices now permit the

construction of hybrid optical processors that provide optical to electrical and man-to-machine interfaces. Two hybrid processors have been described. The first of these is a recognition system using frequency-domain sampling, while the second system is an interactive image-enhancement system. The former system appears well suited for image evaluation or pre-screening, while the latter can be used for rapidly modifying the MTF of an optical system by changing filter functions in the Fourier transform plane.

Acknowledgments

The authors wish to acknowledge the many fruitful discussions with personnel of the RCA Laboratories concerning the various read/write storage mediums.

References:

- ¹ Vander Lugt, A., "A Review of Optical Data Processing Techniques," *Optica Acta*, Vol. 15, No. 1, p. 1, 1968.
- ² Tippett, J. T., et al. (eds.) *Optical and Electro-Optical Information Processing*, MIT Press, Cambridge, Massachusetts, 1965, p. 715.
- ³ Feldstead, E. B., "A Simple Real-Time Incoherent Optical Correlator," *IEEE Transactions AFS*, Vol. AES-3, No. 6, p. 907, Nov. 1967.
- ⁴ Cutrona, L. J., "Optical Computing Techniques," *IEEE Spectrum*, p. 101, Oct. 1964.
- ⁵ Andrews, H. C. and Pratt, W. K., "TV Bandwidth Reduction by Encoding Spatial Frequencies," *J. SMPTE*, Vol. 77, No. 12, p. 1279, Dec. 1968.
- ⁶ Cochran, W. T., et al., "What is the Fast Fourier Transform?," *Proc. IEEE*, Vol. 55, No. 10, pp. 1664-1674.
- ⁷ Stockham, T. G. Jr., "High-Speed Convolution and Correlation," 1966 Spring Joint Computer Conference AFIPS Proc., Vol. 28, pp. 229-233, Washington, D.C., Spartan, 1966.
- ⁸ Pratt, W. K., et al., "Hadamard Transform Image Coding," *Proc. IEEE*, Vol. 57, No. 1, p. 58, Jan. 1969.
- ⁹ Sheats, L. F. and Vickers, H., "Implementation of a Pipeline FFT," *NEREM Record*, p. 156, 1970.
- ¹⁰ Lendaris, G. G. and Stanley, G. L., "Diffraction Pattern Sampling for Automatic Pattern Recognition," *Proc. IEEE*, Vol. 58, No. 2, p. 198, Feb. 1970.
- ¹¹ Darling, E. M. Jr. and Joseph, R. D., "Pattern Recognition from Satellite Altitudes," *IEEE Transactions on Systems Science and Cybernetics*, Vol. SSC-4, No. 1, p. 38, March 1968.
- ¹² Nilsson, N. J., *Learning Machines*, McGraw Hill Book Company, New York 1965.
- ¹³ Nagy, G., "State of the Art in Pattern Recognition," *Proc. of the IEEE*, Vol. 56, No. 5, p. 836, May 1968.
- ¹⁴ Jackson, G., "The Properties of Photochromic Materials," *Optica Acta*, Vol. 16, No. 1, p. 1, 1969.
- ¹⁵ Kiss, Z. J., "Photochromics," *Physics Today*, p. 42, Jan. 1970.
- ¹⁶ Amodel, J. J., "Non-Linear Coloration Effects in Transition—Metal-Doped SrTiO₃ Crystals," *The Physical Review*, Vol. 188, No. 3, p. 1336, Dec. 1969.
- ¹⁷ Ross, D. L., Photochromic Indigoids. III: "A Photochromic Element Based on the cis-trans Photoisomerization of a Thioindigo Dye," *Applied Optics*, Vol. 10, p. 571, March 1971.
- ¹⁸ Urbach, J. C. and Meler, R. W., "Thermoplastic Xerographic Holography," *Applied Optics*, Vol. 5, No. 4, p. 666, April 1966.
- ¹⁹ Oliver, D. S., "An Optical Image Storage and Processing Device Using Electro-Optic ZnS," Presented at the IEEE International Electron Devices meeting, Washington, D.C., Oct. 1970.

- ²⁰ Land, C. E., "Electro-Optic Ceramics for Information Storage and Display," *NEREM Record*, p. 12, 1969.
- ²¹ Dobriner, R. (ed.), "New Progress in Ferroelectric Ceramics," *Electronic Design*, No. 12, p. 21, June 7, 1970.
- ²² Taylor, G. W., Miller, A. and Keneman, S. A., "Bismuth Titanate-Photoconductor Optical Storage Medium," Report AFAL-TR-70-61, April 1970.
- ²³ Brown, B. R. and Lohman, A. W., "Complex Spatial Filtering with Binary Masks," *Applied Optics*, Vol. 5, No. 6, p. 967, June 1966.
- ²⁴ Mezrich, R. S., "Curie-Point Writing of Magnetic Holograms on MnBi," *Applied Physics Letters*, Vol. 14, No. 4, p. 132, Feb. 1969.
- ²⁵ Mezrich, R. S., "Information Storage by Magnetic Holography," *NEREM Record*, p. 158, 1970.
- ²⁶ Poppelbaum, W. J., et al., "On-Line Fourier Transform of Video Images," *Proc. IEEE*, p. 1744, Oct. 1968.
- ²⁷ Casasent, D., "An On-Line Optical Data Processing System," *Proc. of the Electro Optic Systems Conference*, p. 56, 1969.
- ²⁸ Amodei, J. J., et al., "Improved Electro-Optic Materials for Holographic Storage Applications," *Journal of Quantum Electronics*, Vol. QE-7, No. 6, p. 321, June 1971.
- ²⁹ Ovshinsky, S. R. and Klose, P. H., "Reversible High-Speed High-Resolution Imaging in Amorphous Semiconductors," *SID International Symposium Digest*, Vol. 2, p. 58, May 1971.
- ³⁰ Bartolini, R., et al., "Embossed Hologram Motion Pictures for Television Playback," *Applied Optics*, Vol. 9, No. 10, p. 2283, Oct. 1970.
- ³¹ Schade, O. H., Sr., "Electron Optics and Signal Readout of High Definition Return Beam Vidicon," *RCA Review*, Vol. 31, No. 1, p. 60, March 1970.
- ³² Caulfield, H. J. and Maloney, W. T., "Improved Discrimination in Optical Character Recognition," *Applied Optics*, Vol. 8, No. 11, p. 2355, Nov. 1969.
- ³³ Thompson, B. J., et al., "The Use of Holographic Subtraction in the Optical Processing of Reconnaissance Data," *AGARD Proc.*, No. 50, Norway, 1969.
- ³⁴ Lee, S. H., et al., "Optical Image Synthesis (Complex-Amplitude Addition and Subtraction) in Real Time by a Diffraction-Grating Interferometric Method," presented at the Spring Meeting of the Optical Society of America, April 1970.
- ³⁵ Weimer, P. K. et al., "Solid-State Digital Scanning of Mosaic Sensors (Phase IV)," Report AFAL-TR-70-34, April 1970.
- ³⁶ Ramsey, S. D. Jr., "Coherent Optical Processing of Temporal Functions," Standard Electronics Laboratories Report No. 2306-1, prepared under Contract AF33(615)-3589, Nov. 1968.

Low-Noise Punch-Through P-N-v-P, P-N-P, and P-N-Metal Microwave Diodes*

S. G. Liu and J. J. Risko

RCA Laboratories, Princeton, N. J.

Abstract—Three different diode structures of a new type have been constructed; they are low-noise punch-through transit-time devices that use injection of minority carriers. The diodes operate in the frequency range from C to Ku band with powers output of up to several milliwatts. The low-noise feature of all three structures has been demonstrated with small-signal noise figures of 15 dB being measured. Experimental results show that p-n-v-p structures work at higher frequencies and consistently produce higher power output than do p-n-p diodes.

Introduction

Transit-time negative resistance semiconductor diodes for high-frequency applications have been proposed for some time by several authors.¹⁻³ Those now widely in use are the p-n junction⁴ or Read⁵ type diodes where carriers traversing through the depletion region are produced by avalanche multiplication at the reverse-biased junction. The other proposed type uses punch-through p-n-p or p-n-v-p structures,^{4,5} where carriers are produced by minority carrier injection from the p-n junction as the depletion region reaches through the reverse biased n-p or n-v-p region. This injection type diode is inherently a low-noise device compared with the avalanche diode because no avalanche multiplication takes place in the diode. Recently, low-noise microwave oscillations have been reported from a metal-semiconductor-metal (MSM) structure⁷ where minority carrier injection from the metal-semiconductor contact was utilized.

This paper reports on three diode structures, the p-n-v-p, p-n-p, and the p-n-metal, which we fabricated recently, and on their performances

* Material covered in this paper were presented at the International Electron Device Meeting, Washington, D.C., October 1971.

as microwave oscillators and low-noise amplifiers. For convenience in later discussions, some analytical results on these types of diodes are reviewed.

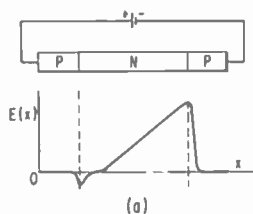


Fig. 1(a)—A reverse-biased p-n diode and its field distribution profile.

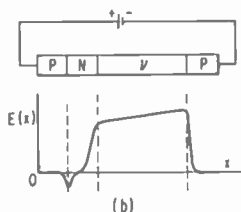


Fig. 1(b) A reverse-biased p-n-v-p diode and its field distribution profile.

Review of Theory

Both Cardinal⁴ and Ruegg⁵ have pointed out that a simple punch-through transit-time p-n-p structure (Fig. 1a) suffers from the low-field region near the forward biased injecting p-n junction. They propose a p-n-v-p structure (Fig. 1b), which raises the field near the forward-biased junction such that carriers drift at saturation velocity through most portions of the depletion region. Assuming the total conduction current is injected at the forward-biased junction according to the simple diode equation,

$$I_o = I_R(e^{qv/kT} - 1), \quad [1]$$

Cardinal⁴ shows that the negative resistance of the p-n-v-p diode exists for a transit angle between π and 2π , and is optimized when, first, the transit angle θ equals about 1.6π ,* which is to say

* This is consistent with Ruegg's approximate result of $(3/2)\pi$.

$$f = 0.8 \frac{v}{W}, \quad [2]$$

and secondly, the angular frequency

$$\omega = 2 \frac{I_0 q}{C_1 k T}, \quad [3]$$

where I_0 is the current through the diode, C_1 the forward-biased capacitance, q the electron charge, k the Boltzmann's constant, T the absolute temperature, v the saturation velocity, and W the width of the drift region. The small-signal analysis is similar to that of Gilden and Hines⁸ for avalanche transit-time diodes and the expression $I_0 q / (C_1 k T)$ is in a sense similar to the avalanche frequency defined by them. The injection zone is now represented by a conductance (rather than an inductance as in the avalanche case) in parallel with a junction capacitance. It is seen from Eq. [3] that the oscillation depends not only on the bias current, but also on temperature and forward-biased junction geometry. Therefore, the diode that oscillates in one bias direction may not oscillate in the reverse direction under the same conditions. A similar small-signal impedance analysis for a Schottky barrier injection contact diode, including image force and related surface state effects, has been recently made by K. P. Weller.⁹

Device Fabrication

The devices were fabricated by starting with silicon epitaxial wafers of a high-resistivity n-type epitaxial layer grown on a p⁺ substrate. The range of resistivity of the epi-layer for the wafers used were between 5 and 6.5 ohm-cm. Higher resistivity was used for the p-n-v-p structure to give a smaller field gradient in the v region. However, no optimization in the design was considered in these initial experimental devices. Instead, the main purpose is to demonstrate the feasibility of such new devices. The substrate was boron doped and had a resistivity of 0.1 to 0.2 ohm-cm. The range of epi-layer thickness prior to diffusion for the wafers used was between 10 and 12 μm; therefore, a punch through in the device is assured. After the diffusion process the net depletion width of the device is much less than the epi-layer thickness, allowing for both the in-diffusion from the diffusant and out-diffusion from the substrate. The p-substrate is boron doped and has

a diffusion coefficient approximately equal that of phosphorus, the diffusant. Therefore, about the same amount of outdiffusion results between the substrate and the high-resistivity epi-layer. This has the merit of reducing imperfections and increasing device reproducibility.¹⁰

For the p-n-p structure, a boron deposition and diffusion is applied to the epitaxial wafer; for the p-n- ν -p structure, a phosphorus diffusion is performed prior to the boron diffusion. Doped oxide films with prescribed carrier concentrations were utilized as diffusants. A schematic of doping profile of the p-n-p and p-n- ν -p diodes is shown in Fig. 2.

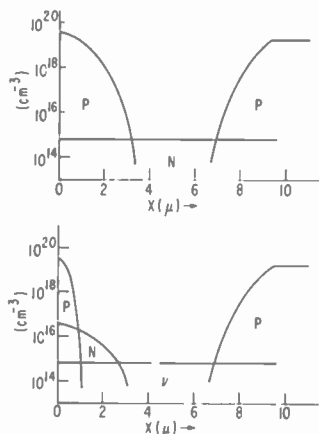


Fig. 2—A sketch of doping profiles of the p-n-p and p-n- ν -p diodes. Both diodes are fabricated by diffusion into silicon epitaxial wafers.

For the fabrication of p-n-metal structure, a platinum silicide Schottky barrier was formed on the n-on-p⁺ epitaxial wafer by sputtering and annealing processes. A wafer was pre-outdiffused for the purpose of reducing the active n-layer thickness and forming a buffer region between the high-resistivity epi-layer and the substrate. The resultant depletion region is about $5\mu\text{m}$ thick. Frustum-shaped diodes¹¹ were then made from the wafer following the metalization and photoresist techniques. Diodes used in the experiments range from 0.008 to 0.025 cm in diameter. Most experiments were performed with 0.020-cm-diameter diodes.

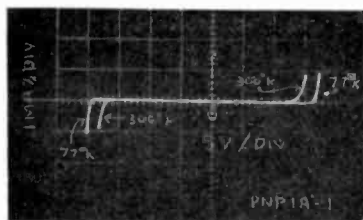
Device Characteristics

The depletion width of the diodes when reverse biased to punch-through can be approximately determined from a C - V measurement

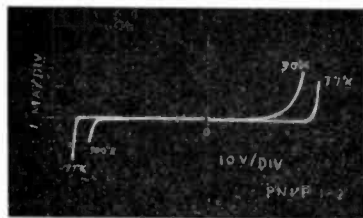
and the diode junction area. The total measured capacitance C for the p-n-p or p-n-v-p structure is given by

$$\frac{1}{C} = \frac{1}{C_1} + \frac{1}{C_2}, \quad [4]$$

where C_1 and C_2 represent the forward and reverse biased junction capacitances, respectively. Because C_1 is in general much larger than



(a)



(b)

Fig. 3—Traces of I-V characteristic curves at 300°K and 77°K respectively of (a) a p-n-p diode, and (b) a p-n-v-p diode. Vertical scale: 1 mA/div. Horizontal scale: (a) 5 V/div, (b) 10 V/div.

C_2 , the measured capacitance C is thus a good approximation for C_2 . Measured depletion widths at punch through are 5.6 and 5.8 μm for the p-n-p and p-n-v-p structures, respectively.

The I-V characteristics of a p-n-p diode and a p-n-v-p diode both at room temperature and liquid-nitrogen temperature are shown in Fig. 3. The traces to the left of the origin are when the substrate side of the diode is reverse (negatively) biased. Two features should be noted. First, because the current is produced by injection rather than avalanche multiplication, the diodes conduct current at a higher voltage when the temperature is reduced (in the case of avalanche multiplication the breakdown voltage decreases at reduced temperature). Secondly, when the diode first draws current the voltage of the p-n-v-p

structure is about 36 volts, while that of p-n-p diode is about 17 volts. This fact is expected from the doping profiles of these two types of diodes as shown in Fig. 2, because the field has been raised at the n-v region in the p-n-v-p structure. Both voltages are consistent with the depletion widths and doping values.

Experiments

The circuit used in the experiment is shown in Fig. 4 where a metal disk forms a localized cavity¹² inside the waveguide. A movable short

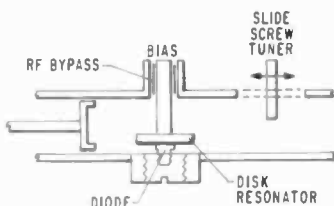


Fig. 4—A waveguide diode oscillator circuit with a disk-resonator structure.

circuit and a slide-screw tuner are provided for impedance matching purposes. The frequency of oscillation is determined mainly by the diameter of the metal disk. Both an X-band and a C-band waveguide circuit* have been used to cover the frequency range above 5 GHz. Diodes were mounted in threaded pill packages before insertion into the circuit.

Microwave oscillations and amplifications were obtained, and small-signal amplifier noise figure of around 15 dB have been measured for all three types of diodes. The oscillations are characterized by a low threshold current density, typically 12 A/cm². Operating voltages of the p-n-p and p-n-metal diodes as low as 16 volts have been obtained. The diodes tend to exhibit an early fall off in rf power output. Power outputs of the present devices at room temperature are typically half a milliwatt for the p-n-p and p-n-metal structures, and a few milliwatt for the p-n-v-p structure. Microwave oscillations have also been obtained using coaxial and microstrip circuits.

Figs. 5, 6, and 7 show typical plots of power output versus bias current of the three diode structures operating at room temperature. The corresponding variation in voltages and oscillation frequencies is

* C-band circuit provided by P. A. Levine.

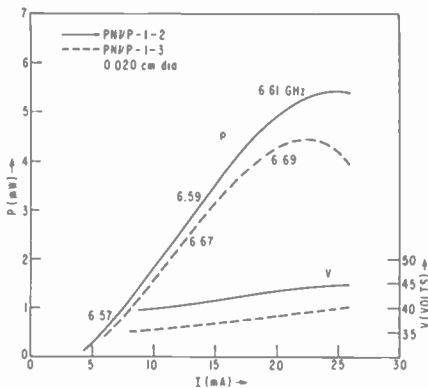


Fig. 5—Power output and bias voltage as a function of bias current of typical p-n-p diodes. The increase in oscillation frequency with current is also shown.

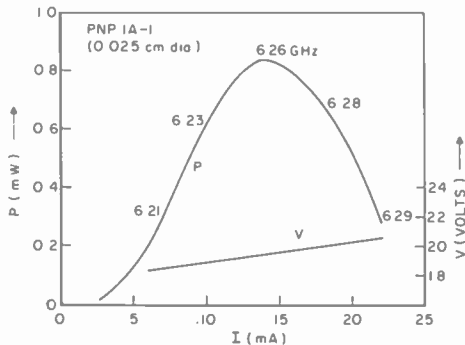


Fig. 6—Power output and bias voltage as a function of bias current of a typical p-n-p diode. Notice increase in frequency with bias current.

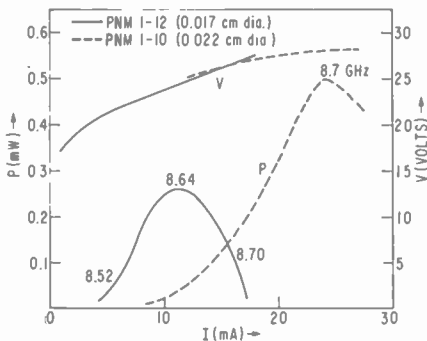


Fig. 7—Power output and bias voltage as a function of bias current of typical p-n-metal diodes. Oscillation frequency increases with increasing current.

also included in the same plot. The increase in frequency with current is expected from Eq. [3]. The p-n-v-p diodes have produced over 5 mW at 6.6 GHz as shown in Fig. 5, and 3 mW at 7.2 GHz in a slightly modified circuit. It is interesting to note that the p-n-v-p structure does operate at a higher frequency and performs better than the p-n-p structure.

At a reduced temperature, oscillations were obtained from small size p-n-metal diodes at Ku-band. The experiment was done in an X-band tunable crystal detector mount. Fig. 8 shows two such diodes operating at two different temperature levels. Power output of 3 mW at 13.2 GHz has been obtained from one diode. The operating voltage has increased from its room-temperature value of around 16 volts.

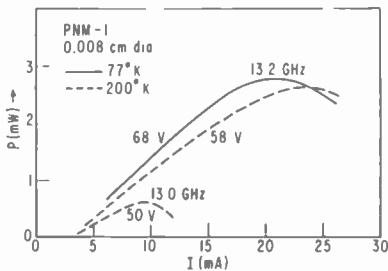


Fig. 8—Small-size p-n-metal diodes oscillate at Ku-band frequency at reduced temperatures.

All three types of diodes have also been incorporated into linear reflection-type amplifiers. Noise figures of 15 dB have been measured at 8.48 GHz with the p-n-metal diode, 15 dB at 6.68 GHz with the p-n-v-p diode, and 16 dB at 5.88 GHz with the p-n-p diode. The gain is in the range of 20 to 25 dB with a corresponding bandwidth under 10 MHz. The measurement was made with the conventional automatic noise figure indicator and noise source tube. Details and more data of the amplifier and noise measurements will be reported in a later paper.

Conclusions

We have fabricated three different types of silicon-punch-through transit-time diodes operating in the frequency range from C to Ku band. The low-noise features of all three types of diodes have been demonstrated with small-signal noise figures of about 15 dB being measured. A simple diffusion process is involved in the fabrication of the p-n and p-n-v-p diodes, although a complete epitaxy or ion-implanta-

tion technique should also be feasible. Experimental results show that p-n-v-p structures work at higher frequencies and consistently produce much higher power output than do p-n-p diodes made from the same type of wafer.

An approximate method of measuring the depletion width of the punch-through p-n-p or p-n-v-p diodes has been described. Based on the measured values of depletion width, the diodes operate at a transit angle substantially less than the optimum value predicted by small-signal analysis. This probably indicates that the injected carriers from the p-n junction for the present diodes do not travel at a saturation velocity throughout the depletion region of the device. Work is being continued for optimization of the diffusion profile of the device.*

Acknowledgments

The authors wish to thank B. S. Perlman for helpful discussions regarding noise measurement, P. Bura for initial measurement on noise figure, H. J. Prager for useful comments on the manuscript. Finally, we wish to thank K. K. N. Chang for many helpful discussions and encouragements.

References:

- ¹ W. Shockley, "Negative Resistance Arising from Transit Time in Semiconductor Diodes," *Bell Sys. Tech. Jour.*, Vol. 33, p. 799, July 1954.
- ² W. T. Read, "A Proposed High Frequency, Negative-Resistance Diode," *Bell Sys. Tech. Jour.*, p. 401, March 1958.
- ³ H. Yoshimura, "Space-Charge Limited and Emitter Current Limited Injections in Space Charge Region of Semiconductors," *IEEE Trans. Elec. Dev.*, Vol. ED-11, p. 414, Sept. 1964.
- ⁴ R. E. Cardinal, private communication.
- ⁵ H. W. Ruegg, "A Proposed Punch-Through, Microwave Negative-Resistance Diode," *IEEE Trans. on Elec. Devices*, Vol. ED-15, p. 577, Aug. 1968.
- ⁶ R. L. Johnston, B. C. DeLoach, and B. G. Cohen, "A Silicon Diode Microwave Oscillator," *Bell Sys. Tech. Jour.*, Vol. 44, p. 369, 1965.
- ⁷ D. J. Coleman, Jr. and S. M. Sze, "A Low-Noise Metal-Semiconductor-Metal (MSM) Microwave Oscillator," *Bell Sys. Tech. Jour.*, p. 1695, May-June 1971.
- ⁸ M. Gilden and M. E. Hines, "Electronic Tuning Effects in the Read Microwave Avalanche Diode," *Trans. on Elec. Devices*, Vol. ED-13, p. 169, Jan. 1966.
- ⁹ K. P. Weller, "Small-Signal Theory of a Transit-Time-Negative Resistance Device Utilizing Injection from a Schottky Barrier," *RCA Review*, Vol. 32, p. 372, Sept. 1971.
- ¹⁰ S. G. Liu and J. J. Risko, "Microwave Oscillation and Amplification with Complementary Silicon Avalanche Diodes," presented at the Int. Elec. Device Meeting, Washington, D. C., Oct. 1971.
- ¹¹ S. G. Liu and J. J. Risko, "Fabrication and Performance of Kilowatt Avalanche Diodes," *RCA Review*, Vol. 31, p. 3, March 1970.
- ¹² T. P. Lee, R. D. Standley, and T. Misawa, "A 50 GHz Silicon IMPATT Diode Oscillator and Amplifier," presented at the International Solid-State Circuit Conference, Philadelphia, Pennsylvania, Feb. 1968.

* Note added in proof: Power output of 40 mW at 6 GHz with 2% efficiency has been obtained from p-n-v-p diodes fabricated recently.

Switching Times of a Moderate-Power GaAs Field-Effect Transistor

L. S. Napoli, W. F. Reichert, R. E. DeBrecht, and A. B. Dreeben

RCA Laboratories, Princeton, N. J.

Abstract—Switching experiments have been conducted on a GaAs, 4-GHz field-effect transistor by driving the transistor with its own output signal delayed by 0.9 ns. The results indicate delay times of 0.11 ns through the transistor, and rise and fall times of the order of 0.22 ns for a drain potential of 10 volts and a current of 30 mA.

Introduction

Moderate-power high-speed switching devices are increasing in importance as components for high data-rate communication systems. Solid-state IMPATT oscillators have delivered hundreds of milliwatts at 60 GHz and are capable of carrying gigabit-rate data streams provided the carrier can be modulated in fractions of a nanosecond.

Schlosser, Beccone and Riggs¹ have digitally phase shifted a 200-mW 55-GHz carrier by modulating a p-i-n diode with +5 and -50 mA (forward-and reverse- switching currents, respectively). The switching time was 0.5 ns using a 50-ohm pulse source but deteriorated to 0.7 ns with a transistorized driver.

It is the purpose of this correspondence to describe switching experiments on a high-frequency Schottky-barrier-gate GaAs field-effect transistor (FET). The transistor, which exhibits delay times of 0.11 ns and rise times of the order of 0.22 ns, is a logical choice as a driver for a p-i-n diode switch in a gigabit data-rate communications system.

Switching Experiments and Results

The transistor is fabricated on semi-insulating GaAs with vapor-deposited n and n⁺ layers 1 or 2 μm thick, as shown in Fig. 1. It is made by a self-aligned gate technique similar to that described by Driver.² The notable device characteristics are 0.01 mho trans-

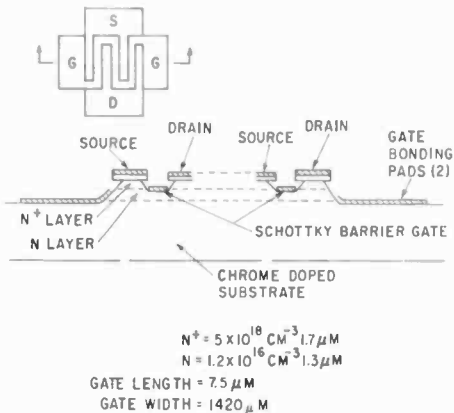


Fig. 1—A profile view of the FET showing various aspects of its construction.

conductance, $7.5 \mu\text{m}$ source-to-drain spacing, and 3.5 to 4.0 GHz f_{max} . Fig. 2 shows the FET characteristics.

Switching-speed measurements are made by using the FET to drive itself, because a pulse source with a fast rise time ($\sim 0.1 \text{ ns}$) and a large voltage swing ($\sim 5 \text{ volts}$) is not available. This is accomplished by connecting the output of the FET to the input via a suitable delay line as is shown in Fig. 3. Since the transistor acts as an inverter, a change

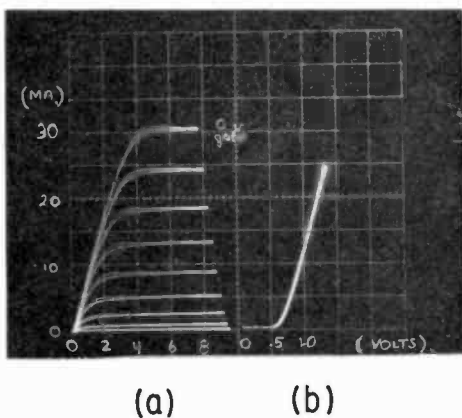


Fig. 2—FET characteristics showing (a) drain current vs. drain voltage for negative gate biases ($0.2\text{v}/\text{step}$) and (b) gate-diode forward current vs. gate-to-source voltage.

in potential at the output of the transistor (e.g., high to low) travels around the ring, is applied to the input, and results in an opposite change in potential at the output (low-to-high). The circuit oscillates in a square-wave-like manner at a frequency corresponding to approximately twice the time delay of the microstrip line. In actual operation the total wave includes the contributions of reflections at both the gate and drain of the transistor.

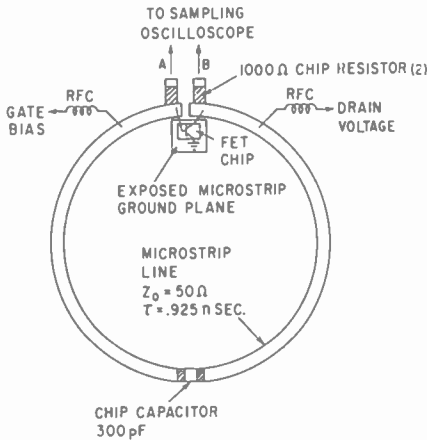


Fig. 3—Oscillator circuit showing the FET and microstrip delay-line feedback ring.

The exact frequency of oscillation is determined by a delay time through the transistor, and a delay time around the transmission line. Therefore, the time delay, τ , through the transistor can be calculated from frequency measurements by,

$$\tau = \frac{1}{2} \left(\frac{1}{f_1} - \frac{1}{f_0} \right),$$

where f_0 is the fundamental resonance frequency of the open-circuited ring (transistor removed) and f_1 is the fundamental frequency of the oscillator. The factor of $1/2$ accounts for the fact that two trips around the ring are required for one period of oscillation. The time delays of the reflected waves at the input and output are of the same order as the delay through the transistor, and should not change the frequency of oscillation significantly. The results of frequency measurements

using a 50-ohm transmission line are shown in Fig. 4 where the delay time, τ , is plotted against drain voltage. For the self-biased case, the gate is grounded through an rf choke in series with a 560-ohm resistor. A constant current flows through the choke to supply the gate Schottky-barrier diode with current during its forward-biased state. The

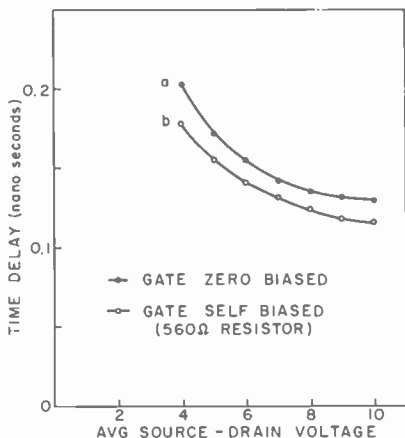


Fig. 4—Time delay through the transistor plotted vs. drain voltage for (a) the gate grounded and (b) the gate negatively biased.

measured gate bias voltages are -0.7 , -1.8 , -2.3 , and -2.5 volts for drain voltages of 4, 6, 8, and 10, respectively. The data for the rf choke attached directly to ground corresponds to the zero-bias curve. The delay times for the self-biased case are slightly lower than the zero-biased case because of the smaller average gate capacitance.

The fact that the product of transistor transconductance, g_m , and transmission-line impedance, Z_o , is less than unity precludes the termination of the transmission line at the gate to eliminate reflections. However, shunting the input of the transistor with 150-ohms gives a delay time of 0.13 ns for 10 volts on the drain, which is the same delay as that for the zero-gate-bias case (Fig. 4).

Putting the transistor in a 111-ohm ring results in a delay time of 0.25 ns for 10 volts on the drain and a zero bias on the gate. Shunting the gate with resistances from 150 to 106 ohms does not change the delay time, indicating that the reflections have little effect on the measured delay.

The voltage waveforms for the 50-ohm system shown in Fig. 5 are taken at the gate and drain contacts of the FET (1000-ohm chip

resistors are connected from the FET terminals to the 50-ohm sampling oscilloscope providing suitable voltage division and minimal loading of the circuit). The rise and fall times, corrected to the 90-ps oscilloscope response time, are 0.22 and 0.39 ns at the drain and 0.33 ns at the gate. These times are longer than the delay time because the FET is providing its own driving pulse and because the reflected waves are only approximately time coincident with the circulating wave.

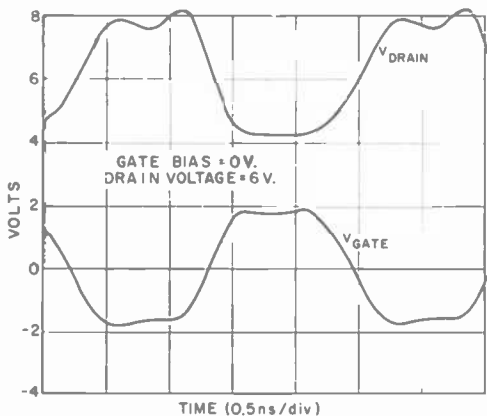


Fig. 5—Oscillator voltage waveforms at the drain and gate of the FET.

In summary, a moderate power GaAs FET has been tested as a switching device in a reentrant resonant ring circuit and for a 50-ohm line, delay time of 0.11 ns, and rise and fall time of the order of 0.22 ns.

Acknowledgments

The authors are indebted to B. Hershenov and A. Farber for their relevant comments on the experiment, to R. Chamberlain and J. J. Hughes for their aid in preparing the device for test, and W. H. Anderson and A. R. Triano, Jr., for providing valuable technical assistance in growing the GaAs.

References:

- ¹ W. O. Schlosser, J. P. Beccone, R. S. Riggs, "A PIN Diode for Mm-Wave Digital Modulation," *Digest G-MTT Symposium*, May 1970, Newport Beach, Calif.
- ² M. C. Driver, "A Self-Aligned-Gate Field-Effect Transistor," *Digest International Electron Device Meeting*, Oct. 28-30, 1970, Washington, D. C.

Transit-Time-Spread-Limited Time Resolution of Image Tubes in Streak Operation

Illes P. Csorba

RCA Electronic Components, Lancaster, Pennsylvania

Abstract—Transit-time spread caused by the emission-energy spread of electrons is analyzed for a uniform electric field, central field, and field-free region. In addition, the time resolution of a two-concentric-sphere type image inverter is calculated.

Introduction

Transit-time spread produced by the emission-energy spread of photoelectrons is one of the fundamental limitations of time resolution of high-speed image-tube cameras. Because of transit-time spread, a point image of a photo event of very short duration is imaged by the camera as a line in streak mode operation. The length of the line is proportional to the transit-time spread. Obviously the shorter the length of the line at a given streak velocity, the better the time resolution of the camera. In various types of image tubes, an electron may travel in a uniform electric field, in a central field, or in a field-free region during the imaging process. In this paper the transit-time spread in each region will be analyzed.

Uniform Electric Field

In the case of a uniform electric field the transit-time difference between two electrons, one having a zero emission velocity and another having a v_a axial emission velocity, may be obtained from the equation of electron motion in a uniform electric field;¹

$$v_s^2 t^2 + 4Lv_a t - 4L^2 = 0, \quad [1]$$

where t is the transit time, L is the screen-to-cathode separation, and

v_s is the electron velocity corresponding to an accelerating voltage V_s . For $v_s \gg v_a$ the transit-time difference ΔT from Eq. [1] is given by

$$\Delta T = 2L \frac{v_a}{v_s^2} = T_r \sqrt{\frac{V_a}{V_s}} = \sqrt{\frac{2m}{e}} \frac{\sqrt{V_a}}{E}, \quad [2]$$

where T_r is the transit time of zero-emission-velocity electrons, V_a is the accelerating voltage required for an electron at rest to acquire its emission energy, E is the electric-field strength, and e and m are the charge and mass of an electron, respectively.

The numerical value of transit-time difference from Eq. [2] is given by

$$\Delta T = 3.37 \times 10^{-8} \frac{L}{V_s} \sqrt{V_a} = 3.37 \times 10^{-8} \frac{\sqrt{V_a}}{E}, \quad [3]$$

where L is in centimeters, V_s and V_a are in volts, and E is in volts per centimeter.

Field-Free Region

Assume that two electrons, one having zero emission energy and another having eV_a axial emission energy, are accelerated across a very small distance to a potential V_s . Then let the electrons travel in a field-free region through a distance L . Denote the transit time of the zero-emission-energy electron by T_r . The transit-time difference of two electrons then becomes

$$\Delta T = \frac{L}{\sqrt{\frac{2e}{m} V_s}} - \frac{L}{\sqrt{\frac{2e}{m} (V_s + V_a)}} = \frac{L}{\sqrt{\frac{2e}{m} V_s}} \left(1 - \sqrt{\frac{V_s}{V_s + V_a}} \right) \quad [4]$$

For $V_s \gg V_a$ Eq. [4] reduces to

$$\Delta T = \frac{L}{\sqrt{\frac{2e}{m} V_s}} \frac{V_a}{2V_s} = \frac{T_r}{2} \frac{V_a}{V_s} = 0.84 \times 10^{-8} \frac{L}{\sqrt{V_s}} \frac{V_a}{V_s}, \quad [5]$$

where L is in centimeters and V_a and V_s are in volts.

Central-Field Region

In a two-concentric-sphere type image-inverting diode,² the electrons travel in a central field up to the anode aperture, then from the anode aperture to the screen in a field-free region. Consider an electron leaving the cathode sphere with an emission velocity v_i and direction θ as indicated in Fig. 1. In the central-field region the electron path is

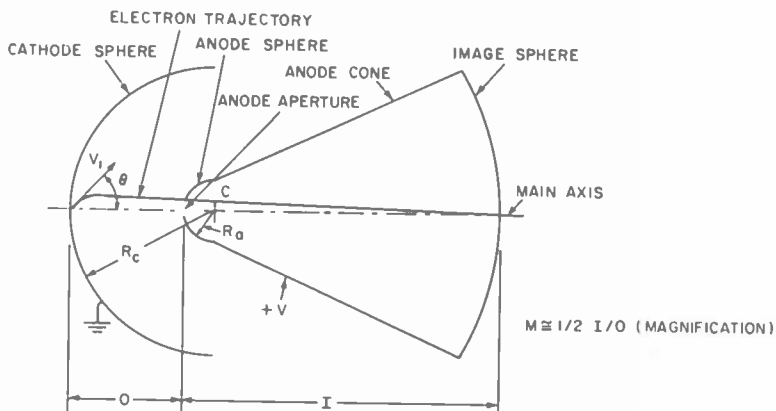


Fig. 1—Schematic diagram of a two-concentric-sphere-type image-inverting electrostatic diode. The central field and the anode aperture lens form an inverted image of the cathode on a sphere concentric with the cathode.

determined by Kepler's law of equal areas:

$$r^2 \frac{d\phi}{dt} = c, \quad [6]$$

where r and ϕ are the radius and angle, respectively, of the spherical coordinates of the centrally symmetric system and c is a constant. The velocity v of the electron may be described by the following equation:

$$v^2 = \left(\frac{dr}{dt} \right)^2 + \left(r \frac{d\phi}{dt} \right)^2. \quad [7]$$

The energy equation is

$$\frac{1}{2} m v^2 = eV(r) + eV_i, \quad [8]$$

where eV_i is the emission energy of the electron and $V(r)$ is the potential distribution given by the following equation³:

$$V(r) = V_s \frac{R_a}{R_c - R_a} \frac{R_c - r}{r}. \quad [9]$$

In Eq. [9], V_s is the anode potential and R_a and R_c are the radius of the anode and cathode spheres respectively. From the boundary conditions the following also holds:

$$R_c \frac{d\phi_o}{dt} = v_i \sin \theta. \quad [10]$$

By combining Eqs. [6] to [10], the following differential equation is obtained:

$$dt = \sqrt{\frac{m}{2e}} \frac{r dr}{\sqrt{\left(V_i - V_s \frac{R_a}{R_c - R_a}\right) r^2 + V_s \frac{R_a R_c}{R_c - R_a} r - R_c^2 V_i \sin^2 \theta}} \quad [11]$$

The transit time of an electron now may be obtained by integration of Eq. [11].

$$\int_0^T dT = - \sqrt{\frac{m}{2e}} \int_{R_c}^{R_a} \frac{r dr}{\sqrt{\left(V_i - V_s \frac{R_a}{R_c - R_a}\right) r^2 + V_s \frac{R_a R_c}{R_c - R_a} r - R_c^2 V_i \sin^2 \theta}}$$

$$T = - \sqrt{\frac{m}{2e}} \left\{ \frac{\sqrt{V_i(R_a^2 - R_c^2 \sin^2 \theta) + V_s R_a^2} - \sqrt{V_i R_c^2 (1 - \sin^2 \theta)}}{V_i R_c - (V_s + V_i) R_a} (R_c - R_a) \right. \\ \left. - \frac{V_s R_a R_c \sqrt{R_c - R_a}}{2[V_s R_a - V_i(R_c - R_a)] \sqrt{V_s R_a - V_i(R_c - R_a)}} \right. \\ \left. \left[\arcsin \left(\frac{V_s R_a (R_c - 2R_a) + 2V_i R_a (R_c - R_a)}{\sqrt{R_a^2 R_c^2 V_s^2 - 4R_c^2 V_i (R_c - R_a) [V_s R_a - V_i (R_c - R_a)] \sin^2 \theta}} \right) \right. \right. \\ \left. \left. + \arcsin \left(\frac{V_s R_a R_c - 2V_i (R_c - R_a) R_c}{\sqrt{R_a^2 R_c^2 V_s^2 - 4R_c^2 V_i (R_c - R_a) [V_s R_a - V_i (R_c - R_a)] \sin^2 \theta}} \right) \right] \right\} \quad [12]$$

For $V_s \gg V_i$ and $R_c > 2R_a$, Eq. [12] reduces to the following equation:

$$T = \sqrt{\frac{m}{2e}} \left\{ \frac{R_c - R_a}{\sqrt{V_s}} + \frac{R_c}{2} \sqrt{\frac{R_c - R_a}{V_s R_a}} \left[\pi - \arcsin \left(\frac{2\sqrt{R_a(R_c - R_a)}}{R_c} \right) \right. \right. \\ \left. \left. + \frac{2(R_c - 2R_a)}{R_c} \sqrt{\frac{R_c - R_a}{R_a}} \sqrt{\frac{V_i}{V_s}} \cos \theta \right] - \frac{R_c}{R_a} (R_c - R_a) \frac{\sqrt{V_i}}{V_s} \cos \theta \right\} \quad [12a]$$

Expanding the arc sin function into Taylor's Series gives:

$$T = \sqrt{\frac{m}{2e}} \left\{ \frac{R_c - R_a}{\sqrt{V_s}} + \pi \frac{R_c}{2} \sqrt{\frac{R_c - R_a}{V_s R_a}} - \frac{R_c}{2} \sqrt{\frac{R_c - R_a}{V_s R_a}} \arcsin \left(\frac{2\sqrt{R_a(R_c - R_a)}}{R_c} \right) \right. \\ \left. - \frac{2R_c}{R_a} (R_c - R_a) \frac{\sqrt{V_i}}{V_s} \cos \theta \right\} \quad [12b]$$

The transit-time difference between a zero-emission-energy electron and an eV_i emission-energy electron from Eq. [12b] is given by

$$\Delta T = - \sqrt{\frac{2m}{e}} \frac{R_c}{R_a} (R_c - R_a) \frac{\sqrt{V_i}}{V_s} \cos \theta. \quad [13]$$

The relationship between the anode voltage V_a and cathode field strength E_c is given by³

$$V_a = E_c \frac{R_c}{R_a} (R_c - R_a) \quad [14]$$

Combining Eqs. [13] and [14] the transit-time difference in seconds expressed with the cathode field strength becomes

$$\Delta T = -\sqrt{\frac{2m}{e}} \frac{\sqrt{V_i}}{E_c} \cos \theta = -\sqrt{\frac{2m}{e}} \frac{\sqrt{V_a}}{E_c} = -3.37 \times 10^{-8} \frac{\sqrt{V_i}}{E_c} \cos \theta \quad [15]$$

where V_i is in volts and E_c is in volts per centimeter. Eq. [15] is identical to Eq. [3].

Time Resolution Calculations

Assume that the photocathode of an image-inverting diode is illuminated with a point image, the duration of the illumination is negligibly small, and the photoelectron image is deflected with a constant speed on the phosphor screen. Assume also an aberration-free imaging process. For a monoenergetic Lambertian electron emission, the incremental current di_θ emitted between angles θ and $\theta + d\theta$ is given by

$$di_\theta = 2I \sin \theta \cos \theta d\theta, \quad [16]$$

where I is the emission current of the point source.

The incremental current di_θ strikes the phosphor screen over a short line dl given by

$$dl = wd(\Delta T), \quad [17]$$

where w is the electron image deflection speed. The value of $d(\Delta T)$ may be obtained by differentiation of Eq. [15].

$$d(\Delta T) = 2 \sqrt{\frac{m}{2e}} \frac{\sqrt{V_i}}{E_c} \sin \theta d\theta. \quad [18]$$

By combining Eqs. [16], [17], and [18], the image current density j is given by

$$j = \frac{di_\theta}{dl} = \sqrt{\frac{2e}{m}} \frac{E_c J}{w\sqrt{V_t}} \cos \theta. \quad [19]$$

By use of Eq. [15], j can be plotted as a function of ΔT .

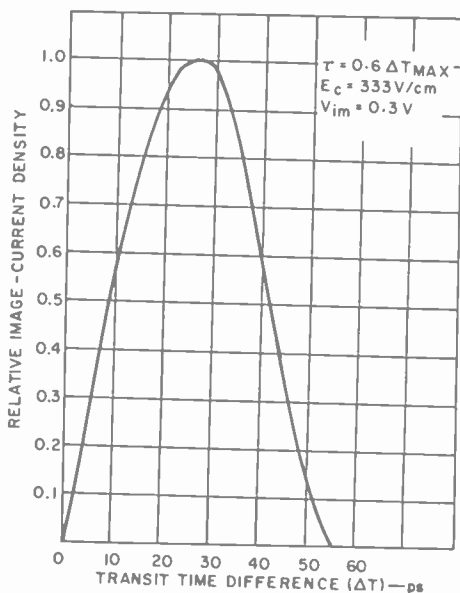


Fig. 2—Image current density as a function of transit-time difference. The emission-energy distribution of Eq. [20] is assumed.

For a polyenergetic emitter, the image current density may be found by summing the image current density of different monoenergetic groups. Fig. 2 shows the image current density distribution calculated for the operating conditions of the RCA Dev. Type C73435 high-speed light-shutter image tube. In the calculation the following emission-energy distribution was assumed:

$$dN = \frac{\pi^2}{2(\pi - 2)} \frac{V_t}{V_{im}} \cos \left(\frac{\pi}{2} \frac{V_t}{V_{im}} \right) d \left(\frac{V_t}{V_{im}} \right); \quad 0 < \frac{V_t}{V_{im}} < 1. \quad [20]$$

where dN is the fraction of electrons emitted in a voltage interval $d(V_e/V_{im})$. The distribution given by Eq. [20] is a normalized energy distribution similar to that measured for typical photocathodes. For an S_1 photocathode illuminated with a 1.06 μm wavelength, the emission energy spread $eV_{im} \cong 0.3$ eV. Therefore, $V_{im} = 0.3$ V was used in the calculation. The time resolution from Fig. 2 is 33 picoseconds, which is the time difference between the 50% image current density points. In the above calculations the transit-time spread in the drift space of the image tube was not included because it is negligibly small as may be concluded from Eq. [5]. (The length of drift space is 14 centimeters.)

If the time resolution calculations were carried out for a different value of emission-energy spread V_{im} or a different value of cathode field strength E_c , only the values of ΔT on the abscissa of Fig. 2 would change. The transit time difference ΔT is proportional to the square root of emission energy and inversely proportional to the cathode field strength. Therefore, the time resolution in seconds may be expressed as

$$\tau = k \frac{\sqrt{V_{im}}}{E_c} = 2 \times 10^{-8} \frac{\sqrt{V_{im}}}{E_c}, \quad [21]$$

where V_{im} is in volts and E_c is in volts per centimeter. The value of $k = 2 \times 10^{-8}$ was obtained by substitution in Eq. [21] of $\tau = 33 \times 10^{-12}$ S., $V_{im} = 0.3$ V, and $E_c = 333$ V/cm. Because of the identity of Eqs. [3] and [15], Eq. [21] is also valid for the electro-magnetic image tubes (uniform electric and magnetic fields).

Conclusion

Results of this study have shown that the transit-time spread limited-time resolution of image tubes is proportional to the emission velocity spread of electrons and inversely proportional to the cathode field strength. It is also shown that the time resolution of the RCA Dev. Tube Type C73435 gated image tube is about 33 picoseconds under normal operating conditions. Smaller time-resolution figures may be obtained by increasing the cathode field strength.⁴ Other limiting factors like the MTF of the image tube, space charge, and resistivity of photocathode⁵ were not considered. Therefore, the time resolution figure obtained here is the limiting time resolution for a given cathode field strength.

Acknowledgment

The author thanks E. G. Ramberg of the RCA Laboratories for his critical reading of this paper and for his many suggestions.

Appendix—Image-Current Distribution as a Function of Transit-Time Difference

Assume a Lambertian emitter with the emission-energy distribution of Eq. [20]. The fraction of electrons emitted between angles θ and $\theta + d\theta$ then may be given by the following equation.

$$dN_{\theta} = \frac{\pi^2}{\pi - 2} \frac{V_i}{V_{im}} \cos\left(\frac{\pi}{2} \frac{V_i}{V_{im}}\right) d\left(\frac{V_i}{V_{im}}\right) \cos\theta \sin\theta d\theta. \quad [22]$$

With substitution of

$$x = \sqrt{\frac{V_a}{V_{im}}} \text{ and } y = \sqrt{\frac{V_r}{V_{im}}} \quad [23]$$

in Eq. [20] the following is obtained

$$dN_{\theta} = \frac{2\pi^2}{\pi - 2} \cos\left[\frac{\pi}{2}(x^2 + y^2)\right] xy \, dx \, dy, \quad [24]$$

where eV_r is the transverse emission energy. The axial emission-energy distribution is:

$$\begin{aligned} dN_a &= \frac{2\pi^2}{\pi - 2} x \, dx \int_0^{\sqrt{1-x^2}} \cos\left[\frac{\pi}{2}(x^2 + y^2)\right] y \, dy \\ &= \frac{2\pi}{\pi - 2} x \left[1 - \sin\left(\frac{\pi}{2}x^2\right)\right] dx. \end{aligned} \quad [25]$$

Combining Eqs. [15], [23], and [25] gives

$$dN_a = \frac{\pi}{\pi - 2} \frac{E_c^2 e}{m V_{im}} \Delta T \left[1 - \sin\left(\frac{\pi}{4} \frac{E_c^2 \Delta T^2 e}{m V_{im}}\right)\right] d(\Delta T). \quad [26]$$

Eq. [26] gives identical results for the image-current distribution with the results shown in Fig. 2, which were obtained by numerical integration of Eq. 19 over the assumed emission-energy distribution.

References:

- ¹ I. P. Csorba, "Resolution Limitations of Electromagnetically Focused Image-Intensifier Tubes," *RCA Review*, Vol. 30, p. 36, March 1969.
- ² I. P. Csorba, "Chromatic-Aberration-Limited Image-Transfer Characteristics of Image-Tube Lenses of Simple Geometry," *RCA Review*, Vol. 31, p. 534, September 1970.
- ³ E. Weber, *Electromagnetic Fields*, p. 151. John Wiley & Sons, Inc., New York, 1950.
- ⁴ M. Ya. Schelev et al, "Image-Converter Streak Camera with Picosecond Resolution," *Applied Physics Letters*, Vol. 18, No. 8, p. 354, 1970.
- ⁵ N. Ahmed et al, In *Advances in Electronics and Electron Physics*, Vol. 28B, p. 999, 1969.

RCA Technical Papers Third Quarter, 1971

July

- "Binary-Intensity Holograms," A. R. Sass, **Jour. Opt. Soc. Amer.**
- "Low-Noise Operation of CW GaAs Avalanche Diode Oscillators," P. A. Levine, A. B. Dreeben, and A. R. Triano, **Proc. IEEE** (Letters)
- "New Performance Criteria for Quadruplex Recorder Servo Systems," K. Sadashige, **Jour. SMPTE**
- "Nonreciprocal Millimeter-Wave Devices Using a Solid-State Plasma at Room Temperature," K. Suzuki and R. Hirota, **IEEE Trans. GED**
- "Product Design of a High-Power J -Band MIC Module for Phased Arrays," F. E. Vaccaro, E. E. Bliss, D. Zieger, and R. P. Lorentzen, **IEEE Trans. GMITT**
- "A Simple Technique for the Accurate Determination of the Microwave Dielectric Constant for Microwave Integrated Circuit Substrates," L. S. Napoli and J. J. Hughes, **IEEE Trans. GMITT** (Correspondence)
- "Spectrum Conservation in the Land Mobile Radio Services," H. Staras and L. Schiff, **IEEE Spectrum**
- "Statistical Distribution of Irradiance in the Creation of a Hologram," D. Vilkomerson, **Jour. Opt. Soc. Amer.**
- "Status of Lumped Elements in Microwave Integrated Circuits—Present and Future," M. Caulton, B. Hershenov, S. P. Knight, and R. E. DeBrecht, **IEEE Trans. GMITT**
- "Dissociation of Eu^{+3} Charge-Transfer State in $\text{Y}_2\text{O}_3\text{S}$ and $\text{La}_2\text{O}_3\text{S}$ into Eu^{+2} and a Free Hole," C. W. Struck and W. H. Fonger, **Phys. Rev. B** (July 1)
- "Amplifier Slew-Rate Curves Simplify Design Decisions," H. A. Wittlinger, **Electronics** (Designer's Casebook) (July 5)
- "Identification of Auger Electrons in GaAs," J. I. Pankove, L. Tomasetta, and B. F. Williams, **Phys. Rev. Letters** (July 5)
- "Electrohydrodynamic and Dielectric Instabilities of Cholesteric Liquid Crystals," W. Helfrich, **Jour. Chem. Phys.** (July 15)

August

- "Advances in FM Receiver Design," J. Avins, **IEEE Trans. GBTR**
- "Amplitude Fluctuations of a Read Diode Oscillator," H. Johnson and B. B. Robinson, **Proc. IEEE** (Letters)
- "Analysis of Maintenance Man Loading Via Simulation," K. Weir and B. Tiger, **IEEE Trans. GR**
- "Applications of Integrated Circuit Technology to Microwave Frequencies," H. Sobol, **Proc. IEEE**
- "Codes for Error Correction In High-Speed Memory Systems—Part 1: Correction of Cell Defects in Integrated Memories," C. V. Srinivasan, **IEEE Trans. GC**
- "Computer Simulation of a Microwave Power Transistor," R. G. Harrison, **IEEE Jour. Solid-State Circuits**
- "Electronic Components and Consumerism," W. C. Hittinger, **IEEE Trans. GBTR**
- "Guidelines for the Design of High-Efficiency Mode Avalanche Diode Oscillators," A. S. Clorfeine, **IEEE Trans. GED**
- "Harmonic Extraction from High-Efficiency Avalanche Diodes," S. G. Liu, **Proc. IEEE**
- "Integrated-Circuit Stereo Decoder Does Everything," L. A. Kaplan, H. M. Kleinman, and A. L. Limberg, **IEEE Trans. GBTR**
- "Microwave Properties and Applications of Negative Conductance Transferred Electron Devices," B. S. Perlman, C. L. Upadhyayula, and W. W. Siekanowicz, **Proc. IEEE**
- "RCA Large-Screen Narrow-Neck 110° Color Television System," C. W. Thierfelder, **IEEE Trans. GBTR**
- "System Techniques for Using Optically Nonuniform Materials," G. W. Taylor and S. A. Keneman, **Proc. IEEE** (Letters)
- Correction to "Threshold Logic," D. Hampel and R. O. Winder, **IEEE Spectrum** (May) 1971; D. Hampel, **IEEE Spectrum** (Forum)
- "Transferred Electron (Gunn) Amplifiers and Oscillators for Microwave Applications," F. Stezzer, **Proc. IEEE**
- "Feedback Zeros DC Level of Diode Gating Circuit," R. J. Turner, **Electronics** (Designer's Casebook) (August 30)
- "Optical Measurements of Magnetite Single Crystals," I. Balberg and J. I. Pankove, **Phys. Rev. Letters** (August 30)

- "The Accuracy of Vehicle Location by Trilateration in a Dense Urban Environment," H. Staras and S. Honickman, **WESCON Tech. Papers**, Session 27, Western Electronic Show and Convention, Los Angeles, Calif., Vol. 15, 1971
- "The Acoustoelectric Effects and the Energy Losses by Hot Electrons Part V—Physical Concepts in Energy-Loss Processes," A. Rose, **RCA Review**
- "AN/ARC-144 UHF Multimode Transceiver," N. R. Avella and Coauthor, **Signal "Automatic Test System for Jet Engine Accessories,"** R. T. Cowley, **WESCON Tech. Papers**, Session 21, Western Electronic Show & Convention, Los Angeles, Calif., Vol. 15, 1971
- "Beam-Lead Processing of Complementary MOS Integrated Circuits," L. A. Murray and B. W. Richards, **WESCON Tech. Papers**, Session 20, Western Electronic Show & Convention, Los Angeles, Calif., Vol. 15, 1971
- "A Bipolar Transistor Model for Device and Circuit Design," R. B. Schilling, **RCA Review**
- "Clutter Suppression by Use of Weighted Pulse Trains," T. Murakami and R. S. Johnson, **RCA Review**
- "Design Considerations for a Future Electroluminescent TV Panel," A. G. Fischer, **IEEE Trans. GED (Correspondence)**
- "GaN Electroluminescent Diodes," J. I. Pankove, E. A. Miller, and J. E. Berkeyheiser, **RCA Review**
- "High Contrast Thermal-Erase Cathodochromic Sodalite Storage-Display Tubes," P. M. Heyman, I. Gorog, and B. Faughnan, **IEEE Trans. GED**
- "Hybrid Integrated Wideband Linear Power Amplifiers for S- and C-Band!," A. Presser, H. C. Huang, R. W. Paglione, and H. C. Johnson, **WESCON Tech. Papers**, Session 23, Western Electronic Show & Convention, Los Angeles, Calif., Vol. 15, 1971
- "Impurity Photoconductivity and Impact Ionization of Shallow States in Semiconductors," R. S. Crandall, **Jour. Appl. Phys.**
- "Infrared Spectroscopic Method for Compositional Determination of Vapor Deposited Borosilicate Glass Films and Results of Its Application," W. Kern, **RCA Review**
- "L-Band High Power Silicon p-i-n Diode Switch," V. Stachejko, **Proc. IEEE (Letters)**
- "Low Birefringent Orthoterrites for Optical Devices," R. B. Clover, Jr., C. Wentworth, and Coauthor, **IEEE Trans. PGMAG**
- "Low-Cost Pulsing of Avalanche Diodes," A. S. Clorfeine, R. D. Hughes, and S. Weisbrod, **RCA Review**
- "Low-Power Digital Frequency Synthesis Application Demonstrates Unique COS/MOS Performance Characteristics," R. E. Funk, **WESCON Tech. Papers**, Session 29, Western Electronic Show & Convention, Los Angeles, Calif., Vol. 15, 1971
- "A Microwave Hybrid with Impedance Transforming Properties," H. Sobol, **IEEE Trans. GMITT (Correspondence)**
- "Mode Guiding in Symmetrical (AlGa)As-GaAs Heterojunction Lasers with Very Narrow Active Regions," H. Kressel, J. K. Butler, F. Z. Hawrylo, H. F. Lockwood, and M. Ettenberg, **RCA Review**
- "Network Utilization of Super-8 Newsfilm," S. Nemeyer, **Jour. SMPTE**
- "Numerical Differentiation Formulas for Stiff Systems of Ordinary Differential Equations," R. W. Klopfenstein, **RCA Review**
- "On Hunting in Hysteresis Motors and New Damping Techniques," S. P. Clurman, **IEEE Trans. PGMAG**
- "Oscillations of Solid-State Plasmas," G. Dorman and Coauthor, **Phys. Rev. A**
- "Re: Cleaning Videotape," B. F. Melchionni, **Jour. SMPTE (Letters to the Editor)**
- "Schottky-Barrier Anomalies and Interface States," J. D. Levine, **Jour. Appl. Phys.**
- "Small-Signal Theory of a Transit-Time-Negative-Resistance Device Utilizing Injection from a Schottky Barrier," K. P. Weller, **RCA Review**
- "Static Negative Differential Resistance in Bulk Semiconductors," F. Sterzer, **RCA Review**
- "Unshielded Capacitor Probe Technique for Determining Disk Memory Ceramic Slider Flying Characteristics," G. R. Briggs and P. G. Heskart, **IEEE Trans. PGMAG**
- "Statistical Properties of Disordered Semiconductors," D. Redfield, **Phys. Rev. Letters** (September 13)

Patents Issued to RCA Inventors Third Quarter, 1971

July

- D. S. Bond** Radio Facsimile Postal System (3,594,495)
A. Boornard Gyromagnetic Notch Filter (3,594,666)
N. W. Burwell and F. R. Dimeo Rotatable Shaft (3,595,505)
J. A. Dean and R. C. Huener Complementary Field-Effect Transistor Buffert Circuit (3,591,855)
P. J. Donald Projection of Color-Coded B and W Transparencies (3,591,274)
A. G. Fischer Optical Semiconductor Device with Glass Dome (3,596,136)
H. R. Frey Photographic Printing of Cathode-Ray Tube Screen Structure (3,592,112)
T. P. Fulton Method of Constructing a Magnetic Core Memory Plane (3,594,897)
J. R. Hall and P. B. Korda Agitation Switch (3,594,520)
Z. J. Kiss Photochromic Display Device (3,592,528)
S. L. Knanishu Circuit and Method for Measuring the Amplification Factor of an In-Circuit or Out-of-Circuit Transistor (3,595,640)
P. Labarre Differential Phase Distortion Compensator for Color Television Equipment (3,593,041)
S. Larach Image Device Having 1000 Angstrom Bandwidth Phosphor Emissive in Blue Region (3,593,054)
N. L. Lindburg Display Device Including Resilient Mounting Means (3,594,602)
S. Liu, J. J. Risko, and K. K. N. Chang High Power Avalanche Diode Microwave Oscillators Having Output Frequency Above Diode Transit Time Frequency (3,593,193)
J. S. Martin, Jr. Method for Preparing Zinc and Zinc-Cadmium Sulfide Phosphors (3,595,804)
H. Perkel and W. H. Comerford Control System for Spinning Bodies (3,591,108)
J. N. Pratt Noise-Cancelling Circuits (3,595,993)
D. A. Wlsner Apparatus for Comparing Two Dimensions (3,593,133)
D. L. Yerzley Sawtooth Frequency Modulation System Including a Waveshaping Frequency Multiplier Chain (3,596,208)

August

- J. B. Bean, Jr.** Television Electronic Control Circuit for Channel Selections (3,602,822)
J. H. Beinart and D. Hampel Storage Circuit (3,599,184)
A. Bernstein AC Overcurrent Protection Circuit (3,602,773)
N. W. Brackelmanns and J. Ollendorf Power Transistor (3,600,646)
J. Breen Method of Making Laminated Semiconductor Devices (3,600,246)
G. W. Carter Electronic Switching of Tuned Circuits (3,602,823)
J. A. Castellano Electro-Optic Light Modulator (3,597,044)
J. A. Cooksey Apparatus for Controlling the Operating Potential of a Vidicon (3,600,511)
R. A. Dischert Color Television Signal-Generating Apparatus (3,601,529)
D. L. Greenaway Apparatus for Making Annual Holograms (3,602,570)
F. G. Hammersand High Power Electron Discharge Device Having Anode with Improved Heat Dissipation Capability (3,601,647)
W. J. Hannan Holographic Storage and Retrieval of Information (3,601,465)
L. A. Harwood Phase Shift Circuits (3,597,639)
G. H. Heilmeier and L. A. Zanoni Electro-Optic Device Having Grooves in the Support Plates to Confine a Liquid Crystal by Means of Surface Tension (3,600,061)

W. A. Helbig, Sr. Circulating Memory-Refreshed Display System (3,598,911)
D. S. Jacobson Radial High Frequency Power Transistor Employing Peripheral Emitter Contact Ring and High Current Base Contact Layer (3,602,780)
L. B. Juroff Noise Immune Pure Carrier Detector Circuit (3,602,821)
M. A. Leedom Electrostatic Printing System Employing a Replaceable Cartridge to Provide a Supply of a Recording Element and Processing Means (3,600,083)
S. Liu and J. J. Risko High Power Avalanche Diode (3,600,649)
J. J. Moscony Method for Preparing Oxide-Coated Cathodes (3,598,646)
J. M. S. Neilson Protection Circuit Including a Thyristor and a Three Terminal Device (3,600,635)
W. L. Oates Apparatus Including a Wire Tipped Probe for Testing Semiconductor Wafers (3,599,093)
A. Orenberg Frequency Synthesizer Having a Plurality of Cascaded Phase Locked Loops (3,600,699)
S. M. Petty and C. R. Pendred Process for Rapid Recording of Polygonal Images (3,600,513)
W. Phillips Photochromic Image Device (3,598,750)
J. W. Rabek Transducer Supporting Arrangement for Disk Memory (3,599,192)
L. A. Rempert Object-Positioning System and Method (3,598,978)
J. Rivera High Current Semiconductor Device Employing a Zinc-Coated Aluminum Substrate (3,597,658)
H. W. Silverman Kinescope Simulator Used in Checking an Automatic Testing System (3,599,092)
G. O. Walter Film Merging Unit (3,600,089)
J. A. Weisbecker Memory Addressing Failure Detection (3,599,146)
J. A. Weisbecker Memory System (3,601,812)
W. D. Williams, D. A. Moe, and C. R. Turner Inverter Including Complementary Transistors (3,602,839)
R. O. Winder Decade Counter Employing Logic Circuits (3,600,561)

September

J. M. Assour Radiation-Sensing Device Comprising an Array of Photodiodes and Switching Devices in a Body of Semiconductor Material (3,604,987)
R. A. Freggens and W. E. Harbaugh Electrical Connector Assembly Having Cooling Capability (3,605,074)
J. B. George Instant-On Circuitry for Solid State Television Receivers (3,603,732)
L. A. Harwood Automatic Chroma Control Circuits (3,604,842)
L. A. Harwood and E. J. Wittmann Amplifier Circuits (3,604,843)
G. H. Heilmeier and L. A. Zanoni Panel Structure for Matrix Addressed Displays (3,603,894)
W. J. Howarth Electro-Optical Image Forming System (3,609,222)
N. W. Hursh and J. J. McArdle Power Supply Utilizing a Diode and Capacitor Voltage Multiplier for Tracking Focusing and Ultor Voltages (3,609,446)
S. W. Kessler, Jr. and J. L. Hess Flexible Heat Pipe (3,604,504)
J. T. Kindley Keyboard for a Computer or Similar Article (D221951)
D. W. Janz and R. E. Seeger Three-Axis Drive System (3,605,977)
B. J. Lechner Color Display for Computer Terminal (3,603,962)
R. D. Lohman, G. A. Alphonse, and W. F. Kosonocky Binary Light Beam Deflector Using Acoustic Waves (3,609,009)
L. R. Motisher and E. Engel Clock Pulse Generator (3,609,408)
J. Ollendorf and F. P. Jones Power Transistor Having Ballasted Emitter Fingers Interdigitated with Base Fingers (3,609,460)
J. J. O'Toole Color Television Video Signal Processing Apparatus (3,609,224)
R. J. Ryan Multilayer Circuit Board Techniques (3,606,677)
I. E. Smith Method for Making an Electron-Tube Grid Assembly (3,604,080)
I. H. Sublette Pattern Recognizer (3,609,687)
G. W. Taylor and P. Goldstein Fluid Variable Light Deflector (3,606,523)
G. W. Taylor Light Deflection System (3,609,004)
R. C. Vandenheuvel Constant Time Stroke Generator (3,609,444)

AUTHORS



Gardner Burton received a B.S. in EE from Drexel Institute of Technology in 1957 under the cooperative engineering program. He received an M.S. in EE from the University of Pennsylvania in 1964. Mr. Burton joined the RCA Advanced Technology Laboratories in 1957 and was engaged in the development of transistor circuitry for digital logic operations, i-f and video signal processing in noisy environments, and FM modulation and demodulation systems. He studied methods for synchronizing binary data transmission systems in noisy environments, and modulation methods for transmitting pictorial information at high data rates. He also in-

vestigated methods for reading printed documents automatically. Mr. Burton was responsible for the design of the RCA Ideographic Composing Machine used for the composition of Chinese text on photographic film. He developed an automatic exposure control system for night aerial cameras using image-amplifier tubes. He was responsible for the development of wideband optical modulation techniques and their associated electronics, and for the electronic and optical modulation design of a high-resolution laser-beam image recorder. He has extensive experience in the application of aperture-response techniques to the analysis and design of electro-optic systems. In 1967 he was promoted to Leader of the Electro-Optic Techniques group of the Advanced Technology Laboratories. During the early part of 1969, he transferred to the Burlington satellite laboratory as Leader of the Visual Techniques group, where he directs efforts concerned with the development of optical processing and holographic techniques.

Mr. Burton is a member of the IEEE and SMPTE.



Richard Croce received his BEE degree from Manhattan College in 1962. He continued his studies at New York University while serving as a Senior Electronics Lab Instructor at Manhattan College and received his MEE degree in 1963. Since joining RCA, Mr. Croce has been involved with the design and development of an ICW radar range tracker and a three-tone radar tracker associated with the landing and docking radars, respectively, in the Lunar Module (LM) on the APOLLO Program. Mr. Croce has also investigated the Q-switch properties of singly and doubly doped neodymium YAG laser rods which resulted in the delivery of the COIN

ranging and guidance laser system. He participated in the development of a light-weight GaAs diode laser rangefinder and has investigated the energy transfer time from the chromium to the neodymium ions in double doped YAG lasers. Recently, he has made contributions to programs involving a holographic multi-color moving-map display, methods for holographically storing and retrieving a miniaturized data base, and pattern recognition systems using parallel processing logic techniques. He is presently involved in programs to apply coherent processing techniques to the problem of two dimension pattern recognition and image-enhancement systems.

Mr. Croce is a member of SID.



I. P. Csorba graduated from the Electrical Engineering Fundamentals at the Electrical Engineering Faculty of the Technical University of Budapest in 1952. In the same year he was admitted to the Communication Engineering Faculty, specializing in communication and electronics. In October, 1954, he received the Diplôme Ingénieur Degree in Electrical and Communication Engineering. From 1955 to 1956 he worked as a research engineer at the War Technical Institute, Budapest. In December of 1956 he joined the research group of Rauland Corporation, Chicago, where he worked on electrostatic-type image converter tubes, television picture tubes, scan-converter tubes. From 1959 to 1961 he was with Motorola, Inc., Chicago, working primarily on electrostatic-type scan magnification. In November of 1961, he joined RCA as a member of the Photo and Image Tube Engineering Activity. Mr. Csorba has been active in the design and development of magnetic and electrostatic-type image tubes and recently has been engaged in product development work on high-speed light-shutter image tubes.



Robert E. DeBrecht received his Bachelor's degree in Engineering Physics in 1966 and his Master's degree in Electrical Engineering in 1968, both from the University of California at Berkeley. Mr. DeBrecht joined RCA Laboratories in 1968, working on the design and fabrication of integrated circuits. In 1969 he became part of the Microwave Integrated Circuits Group working on the measurement of microwave integrated-circuit lumped elements. Recently, he has been working on GaAs Schottky-Barrier field-effect transistors.



Arthur Dreeben completed his graduate work in Inorganic and Solid State Chemistry and Physics at the Polytechnic Institute of Brooklyn in 1950. He held a Teaching Fellowship, and did research on Infrared Stimulable phosphors. From 1950 to 1953, he was employed as a research chemist at the General Electric Research and Knolls Atomic Power Laboratories on the development of analytical and radiochemical procedures. In 1953, he joined the research department of the Westinghouse Lamp Division as a Research Engineer. Here, he did research in the field of luminescence, including high-temperature phosphors, lamp phosphors, and transparent luminescent films. He joined RCA Laboratories in 1958 as a Member of the Technical Staff and has worked on photoconductors, electroluminescence, problems in crystal growth, dislocations, and impurity precipitation in semiconductors. At present he is working on the growth and properties of epitaxial layers of III-V compounds for various microwave devices.

He is listed in "American Men of Science" and is a member of the American Chemical Society, the Electrochemical Society, Sigma Xi, and Phi Lambda Upsilon.



Shing-gong Liu received his B.S. degree in electrical engineering from Taiwan University, Taipei, Taiwan, in 1954, the M.S. degree in electrical engineering from North Carolina State College, Raleigh, North Carolina, in 1958, and the Ph.D. degree in electrical engineering from Stanford University, Stanford, California, in 1963. From 1958 to 1959 he worked with the IBM Laboratories, Poughkeepsie, New York. He was a research assistant at the Hansen Microwave Laboratories, Stanford University, where he worked in the field of microwave ferrites. He joined RCA Laboratories, Princeton, New Jersey, in 1963, and has since worked

principally in the areas of semiconductor microwave devices.

Dr. Liu is a member of Phi Kappa Phi, Sigma Xi, and the American Physical Society.



Louis S. Napoli received his B.S. in 1959 and the M.S. in 1961 in Electrical Engineering, both from Rutgers University. He has pursued further studies in electrophysics at the Polytechnic Institute of Brooklyn. He joined the technical staff of RCA Laboratories in June, 1959, and has engaged in research in phase-locked oscillators as a microwave logic device. He has specialized in research relating to microwave phenomena in gaseous plasmas, solid-state microwave devices, and is now engaged in research on solid-state microwave integrated circuits. His work in collaboration with Dr. George Swartz on amplification at 24 Gc by the interaction

of an electron beam with a cesium plasma was cited by Industrial Research Magazine as one of the 100 most important achievements in 1963.

Mr. Napoli is a member of Sigma Xi, the Institute of Electrical and Electronics Engineers, Tau Beta Pi, and Eta Kappa Nu.



Leon S. Nergaard attended the University of Minnesota and received the B.S. degree in electrical engineering in 1927. He received the M.S. degree in electrical engineering from Union College, Schenectady, New York, in 1930 and the Ph.D. degree in physics from the University of Minnesota in 1935. From 1927 to 1930 Dr. Nergaard was associated with the research laboratory and vacuum-tube engineering department of the General Electric Company. He held a teaching assistantship in the Department of Physics at the University of Minnesota from 1930 to 1933. Dr. Nergaard joined the RCA Manufacturing Company at Harrison, New

Jersey, in 1933 and transferred to RCA Laboratories as a research physicist in 1942. At Harrison, he worked on microwave measurements, on receiving, transmitting, microwave and pulse-radar tubes. After the transfer to Princeton he continued work on pulse-radar tubes until the end of the war. Since then he has worked on transmitting tubes and television transmitters, then switched to solid-state physics, particularly the semiconducting properties of oxide cathodes. He assumed responsibility for the microwave work at RCA Laboratories in 1957. In 1959 he was appointed associate laboratory director, Electronics Research Laboratory. He assumed the responsibility of Director of the Microwave Research Laboratory in 1961. Dr. Nergaard retired in 1971, and now serves as a consultant to RCA.

Dr. Nergaard is a Fellow of both the American Physical Society and the Institute of Electrical and Electronic Engineers, a member of the American Association for the Advancement of Science. He has been active in numerous committees of the IEEE, URSI, and is a member of the Theta Kappa Nu, Gamma Alpha and Sigma Xi.



Walter F. Reichert graduated from De Witt Clinton High School in 1952 and served in the U.S. Army from 1954 to 1956. He attended RCA Institutes in New York, receiving his certificate in the General Electronics Technology Course. He has received his Second Class Radio Operators License. He has attended Rutgers University, and at present is working toward an ASEE at Middlesex County College.

Mr. Reichert joined RCA Laboratories, Princeton, New Jersey, in September 1961 as a Research Technician. Since this time he has participated in experiments dealing with cesium recombination, double-stream amplifiers, crystal acoustics, and surface wave propagation in CdS. His recent work has been on GaAs Schottky Barrier Diodes; at present he is working on fabrication of GaAs field-effect transistors.



John J. Risko graduated from RCA Institutes T-3 program in 1962 and is now an evening student at Newark College of Engineering. He joined RCA laboratories in 1962 and has worked in the research and development area of gallium antimonide tunnel diodes, gallium arsenide varactor diodes and more recently silicon avalanche diodes. He is currently engaged in work involving the high-efficiency mode avalanche diode.

Mr. Risko is an associate member of IEEE.



Otto H. Schade, Sr. was born and educated in Germany; he came to the United States in 1926. He joined RCA Electronic Components and Devices, Harrison, New Jersey, in 1931. Since 1938, he has specialized in television circuits, camera tubes, and picture tubes. From 1944 to 1957 he worked on a unified general method of image analysis and specification, including practical methods for measuring the "aperature" effect (square-wave and sine-wave response function) and fluctuation levels (noise) of optical, photographic, and electronic image-system components and the eye. He has had the responsibility for the thermal and

electrical design of nuvistor tubes. More recently, he has developed an accurate method for calculating the resolving power of television and photographic imaging systems to assist in the evaluation of high-definition television systems, and a new electron optic providing minimum aberrations and uniform focus in television camera tubes with larger (50 × 50 mm) image surfaces. Dr. Schade has received numerous honors, including the Modern Pioneers Award of the National Association of Manufacturers (1940), the Morris Liebmann Memorial Prize of the Institute of Radio Engineers (1950) and a Fellowship (1951) from the Institute of Radio Engineers. In 1951 he was made a Fellow, and also was the first recipient of the David Sarnoff Gold Medal Award, of the Society of Motion Picture and Television Engineers. In June 1953, he was invested with the honorary degree of Doctor of Engineering by Rensselaer Polytechnic Institute. In 1960, he received the Progress Medal Award of the Society of Motion Picture and Television Engineers for his outstanding technical contribution in the engineering phases of the motion picture and television industries

Index 1971 Volume 32

Contents

- 3 Microwave Amplification Using Transferred-Electron Devices in Prototype Filter Equalization Networks
Barry S. Perlman
- 24 A New Type of Gallium Arsenide Field-Effect Phototransistor
G. A. Swartz, A. Gonzalez, and A. Dreeben
- 42 MOS Models and Circuit Simulation
John E. Meyer
- 64 Radiochemical Study of Semiconductor Surface Contamination
III. Deposition of Trace Impurities on Germanium and Gallium Arsenide
Werner Kern
- 88 A Comparative Analytical Study of the Performance of Argon Laser Amplifiers and Oscillators
I. Gorog
- 115 Computer Calculation of Electron Trajectories in Television Camera Tubes
Otto H. Schade, Sr.
- 144 Analysis and Optimization of a Field-Emitter Array
Jules D. Levine
- 150 Contrast Characteristics of X-Ray Images
Illes P. Csorba
- 164 Accurate Measurements of Isolation in Three-Port Circulators
Robert L. Ernst
- 172 RCA Technical Papers
- 174 Patents
- 177 Authors

June 1971 Volume 32 Number 2

- 185 Analysis of Transport Processes During Holographic Recording in Insulators
Juan J. Amodi
- 199 System Aspects of Electrophotographic Materials and Processing for Liquid Reversal Toning
E. C. Gialmo and H. Wielicki
- 221 High-Level Current Gain in Bipolar Power Transistors
J. Olmstead, W. Einthoven, S. Ponczak, and P. J. Kannam

- 247 Observation of the Influence of Base Widening Upon Beta and f_T
C. F. Wheatley
- 251 Systems and Technologies for Solid-State Image Sensors
Paul K. Weimer
- 263 Optical Techniques for Detecting Defects in Silicon-On-Insulator Devices
Richard A. Sunshine
- 279 Symmetrical Trough Waveguide Nonresonant Ferrite Isolators and Steerable Antenna
C. P. Wen
- 289 RF Sputtered Transparent Conductors II: The System $\text{In}_2\text{O}_3\text{-SnO}_2$
John L. Vossen
- 297 Contrast Thresholds of Image-Intensifier-Aided Eye at Low Field-Luminance Levels
Illes P. Csorba
- 306 A Technique for Selective Electroless Plating
N. Feldstein and T. S. Lancsek
- 311 The Ad-Conductor Cathode
Karl G. Hernqvist
- 319 Permanent-Holograms in Glass by RF Sputter Etching
J. J. Hanak and J. P. Russell
- 325 RCA Technical Papers
- 327 Patents
- 330 Authors

September 1971 Volume 32 Number 3

- 339 A Bipolar Transistor Model for Device and Circuit Design
R. B. Schilling
- 372 Small-Signal Theory of a Transit-Time-Negative-Resistance Device Utilizing Injection from a Schottky Barrier
K. P. Weller
- 383 GaN Electroluminescent Diodes
J. I. Pankove, E. A. Miller, and J. E. Berkeyheiser
- 393 Mode Guiding in Symmetrical (AlGa)As-GaAs Heterojunction Lasers with Very Narrow Active Regions
H. Kressel, J. K. Butler, F. Z. Hawrylo, H. F. Lockwood, and M. Ettenberg
- 402 Clutter Suppression by Use of Weighted Pulse Trains
T. Murakami and R. S. Johnson
- 429 Infrared Spectroscopic Method for Compositional Determination of Vapor Deposited Borosilicate Glass Films and Results of Its Application
W. Kern
- 447 Numerical Differentiation Formulas for Stiff Systems of Ordinary Differential Equations
R. W. Klopfenstein
- 463 The Acoustoelectric Effects and the Energy Losses by Hot Electrons
Part V—Physical Concepts in Energy-Loss Processes
A. Rose

- 489 Low-Cost Pulsing of Avalanche Diodes
A. S. Clorfeine, R. D. Hughes, and S. Weisbrod
- 497 Static Negative Differential Resistance in Bulk Semiconductors
F. Sterzer
- 503 Technical Papers Published
- 505 Patents
- 508 Authors

December 1971 Volume 32 Number 4

- 517 Memorial to David Sarnoff by Elmer W. Engstrom
- 519 Amplification—Modern Trends, Techniques and Problems II
Leon S. Nergaard
- 567 Resolving Power Functions and Integrals of High-Definition Television and Photographic Cameras—A New Concept In Image Evaluation
Otto H. Schade Sr.
- 610 Techniques for High-Data-Rate Two-Dimensional Optical Pattern Recognition
R. Croce and G. Burton
- 636 Low-Noise Punch-Through P-N-v-P, P-N-P, and P-N-Metal Microwave Diodes
S. G. Liu and J. J. Risko
- 645 Switching Times of a Moderate-Power GaAs Field-Effect Transistor
L. S. Napoli, W. F. Reichert, R. E. DeBrecht, and A. B. Dreeben
- 650 Transit-Time-Spread-Limited Time Resolution of Image Tubes in Streak Operation
Illes P. Csorba
- 660 RCA Technical Papers
- 662 Patents
- 664 Authors
- 668 Index to Volume 32, 1971

Index to Authors, Volume 32, 1971

- J. J. Amodel Analysis of Transport Processes During Holographic Recording in Insulators, June, p. 185
- J. E. Berkeyheiser (coauthor) GaN Electroluminescent Diodes, September, p. 383
- G. Burton (coauthor) Techniques for High-Data-Rate Two-Dimensional Optical Pattern Recognition, December, p. 610
- J. K. Butler (coauthor) Mode Guiding to Symmetrical (AlGa)As-GaAs Heterojunction Lasers with Very Narrow Active Regions, September, p. 393
- A. S. Clorfeine (coauthor) Low-Cost Pulsing of Avalanche Diodes, September, p. 489
- R. Croce (coauthor) Techniques for High-Data-Rate Two-Dimensional Optical Pattern Recognition, December, p. 610
- I. P. Csorba Contrast Characteristics of X-Ray Images, March, p. 150
—Contrast Thresholds of Image-Intensifier-Aided Eye at Low Field Luminescence Levels, June, 297
—Transit-Time-Spread-Limited Time Resolution of Image Tubes in Streak Operation, December, p. 650
- R. E. DeBrecht (coauthor) Switching Time of a Moderate-Power GaAs Field Effect Transistor, December, p. 645
- A. Dreeben (coauthor) A New Type of Gallium Arsenide Field-Effect Phototransistor, March, p. 24
—Switching Times of a Moderate-Power GaAs Field-Effect Transistor, December, p. 645
- W. Einthoven (coauthor) High-Level Current Gain in Bipolar Power Transistors, June p. 221
- E. W. Engstrom Memorial to David Sarnoff, December, p. 517
- R. L. Ernst Accurate Measurements of Isolation in Three-Port Circulators, March, p. 164
- M. Ettenberg (coauthor) Mode Guiding in Symmetrical (AlGa)As-GaAs Heterojunction Lasers with Very Narrow Active Regions, September, p. 393
- N. Feldstein (coauthor) A Technique for Selective Electroless Plating, June, p. 306
- E. C. Glaimo (coauthor) System Aspects of Electrophotographic Materials and Processing for Liquid Reversal Toning, June, p. 199
- A. Gonzales (coauthor) A New Type of Gallium Arsenide Field-Effect Phototransistor, March, p. 24
- I. Gorog A Comparative Analytical Study of the Performance of Argon Laser Amplifiers and Oscillators, March, p. 88
- J. J. Hanak (coauthor) Permanent Holograms in Glass by RF Sputter Etching, June, p. 319
- F. Z. Hawrylo (coauthor) Mode Guiding in Symmetrical (AlGa)As-GaAs Heterojunction Lasers with Very Narrow Active Regions, September, p. 393
- K. G. Hernqvist The Ad-Conductor Cathode, June, p. 311
- R. D. Hughes (coauthor) Low-Cost Pulsing of Avalanche Diodes, September, p. 489
- R. S. Johnson (coauthor) Clutter Suppression by Use of Weighted Pulse Trains, September, p. 402
- P. J. Kannam (coauthor) High-Level Current Gain in Bipolar Power Transistors, June, p. 221
- W. Kern Radiochemical Study of Semiconductor Surface Contamination III. Deposition of Trace Impurities on Germanium and Gallium Arsenide, March, p. 64
—Infrared Spectroscopic Method for Compositional Determination of Vapor Deposited Borosilicate Glass Films and Results of its Application, September, p. 429
- R. W. Klopfenstein Numerical Differentiation Formulas for Stiff Systems of Ordinary Differential Equations, September, p. 447
- H. Kressel (coauthor) Mode Guiding in Symmetrical (AlGa)As-GaAs Heterojunction Lasers with Very Narrow Active Regions, September, p. 393
- T. S. Lancsek (coauthor) A Technique for Selective Electroless Plating, June, p. 306

- J. D. Levine** Analysis of Optimization of a Field-Emitter Array, March, p. 144
- S. G. Liu** (coauthor) Low-Noise Punch-Through P-N-v-P, P-N-P, and P-N-Metal Microwave Diodes, December, p. 636
- H. F. Lockwood** (coauthor) Mode Guiding in Symmetrical (AlGa)As-GaAs Heterojunction Lasers with Very Narrow Active Regions, September, p. 393
- J. E. Meyer** MOS Models and Circuit Simulation, March, p. 42
- E. A. Miller** (coauthor) GaN Electroluminescent Diodes, September, p. 383
- T. Murakami** (coauthor) Clutter Suppression by Use of Weighted Pulse Trains, September, p. 402
- L. S. Napoli** (coauthor) Switching Times of a Moderate-Power GaAs Field-Effect Transistor, December, p. 645
- L. S. Nergaard** Amplification—Modern Trends, Techniques, and Problems II, December, p. 519
- J. Olmstead** (coauthor) High-Level Current Gain in Bipolar Power Transistor, June, p. 221
- J. I. Pankove** (coauthor) GaN Electroluminescent Diodes, September, p. 383
- B. S. Perlman** Microwave Amplification Using Transferred-Electron Devices in Prototype Filter Equalization Networks, March, p. 3
- S. Ponczak** (coauthor) High-Level Current Gain in Bipolar Power Transistors, June, p. 221
- W. F. Reichert** (coauthor) Switching Times of a Moderate-Power GaAs Field-Effect Transistor, December, p. 645
- J. J. Risko** (coauthor) Low-Noise Punch-Through P-N-v-P, P-N-P, and P-N-Metal Microwave Diodes, December, p. 636
- A. Rose** The Acoustoelectric Effects and the Energy Losses by Hot Electrons Part V—Physical Concepts in Energy-Loss Processes, September, p. 463
- J. P. Russell** (coauthor) Permanent Holograms in Glass by RF Sputter Etching, June, p. 319
- O. H. Schade, Sr.** Computer Calculation of Electron Trajectories in Television Camera Tubes, March, p. 115
—Resolving Power Functions and Integrals of High-Definition Television and Photographic Cameras—A New Concept in Image Evaluation, December, p. 567
- R. B. Schilling** A Bipolar Transistor Model for Device and Circuit Design, September, p. 339
- F. Sterzer** Static Negative Differential Resistance in Bulk Semiconductors, September, p. 497
- R. A. Sunshine** Optical Techniques for Detecting Defects in Silicon-On-Insulator Devices, June, p. 263
- G. A. Swartz** (coauthor) A New Type of Gallium Arsenide Field-Effect Phototransistor, March, p. 24
- J. L. Vossen** RF Sputtered Transparent Conductors II: The System $\text{In}_2\text{O}_3\text{-SnO}_2$, June, p. 289
- P. K. Weimer** Systems and Technologies for Solid-State Image Sensors, June, p. 251
- S. Welsbrod** (coauthor) Low-Cost Pulsing of Avalanche Diodes, December, p. 489
- K. P. Weller** Small-Signal Theory of a Transit-Time-Negative-Resistance Device Utilizing Injection from a Schottky Barrier, September, p. 372
- C. P. Wen** Symmetrical Trough Waveguide Nonresonant Ferrite Isolators and Steerable Antenna, June, p. 279
- C. F. Wheatley** Observation of the Influence of Base Widening Upon Beta and f_T , June, p. 247
- H. Wielicki** (coauthor) System Aspects of Electrophotographic Materials and Processing for Liquid Reversal Toning, June, p. 199